

HYBRID METHODS FOR SIMULATION
OF MUON IONIZATION COOLING CHANNELS

BY
JOSIAH D. KUNZ

Submitted in partial fulfillment of the
requirements for the degree of
Doctor of Philosophy in Physics
in the Graduate College of the
Illinois Institute of Technology

DMK comments

DMK comments

Mostly quite good
clearly written

Some more justification
of the math would help,
and some math details
could be omitted

Some stylistic issues.

Approved _____
Advisor

Chicago, Illinois
August 2016

ACKNOWLEDGMENT

Not if
you say
it

It goes without saying that I am grateful to God, who has guided me in my academic path and has allowed me to fulfil my dream of getting my Ph.D. in Physics. I would also like to thank my wife, Meredith Kunz, who has been by my side even before graduate school. I am very fortunate to have an advisor like Pavel Snopok, who puts in so much time and thought on my behalf. Pavel has worked with me on every turn. I could be no luckier than to have an advisor like him.

I would like to acknowledge the committee for their valuable time and selflessness: Dan Kaplan, Linda Spentzouris, Yagmur Torun, and Xiaofan Li. The Department of Energy is also acknowledged for funding me through Pavel.

On a less serious note, I would like to thank my late cat Scout, who slept on my lap through many of my COSY days. Although he did not make it to see the end result, he will not be forgotten. I would also like to thank my puppy Oliver for his patience with me while writing my thesis, and for keeping my mind fresh with breaks for playtime.

TABLE OF CONTENTS

	Page
ACKNOWLEDGEMENT	iii
LIST OF TABLES	vi
LIST OF FIGURES	ix
LIST OF SYMBOLS	x
ABSTRACT	xiv
CHAPTER	
1. INTRODUCTION	1
1.1. Muon-based Accelerators	1
1.2. COSY Infinity	3
1.3. Introduction to Matter-Dominated Lattices	8
1.4. Emittance	13
1.5. Looking Forward	17
2. STOCHASTIC PROCESSES IN OTHER CODES	20
2.1. Energy Straggling in ICOOL	20
2.2. Multiple Scattering in ICOOL	35
2.3. Energy Straggling in G4Beamline	43
2.4. Multiple Scattering in G4Beamline	47
3. STOCHASTIC PROCESSES IN COSY INFINITY	53
3.1. Energy Straggling in COSY	53
3.2. Multiple Scattering in COSY Infinity	56
3.3. Transverse Displacement in COSY Infinity	65
3.4. Temporal Displacement in COSY Infinity	69
4. SOFTWARE IMPLEMENTATION	72
4.1. User Input	72
4.2. COSYScript Level	74
4.3. FORTRAN Level	75
4.4. Summary	76
5. RESULTS	77
5.1. Benchmark Against Other Codes	77
5.2. Validation	90

5.3. The Muon Ionization Cooling Experiment	93
5.4. Summary	105
APPENDIX	105
A. DERIVATION OF TRANSVERSE EMITTANCE	106
B. DERIVATION OF IMPLEMENTED SCATTERING CROSS SECTION	111
C. A BRIEF REVIEW OF RELEVANT PARTICLE PHYSICS . .	123
D. EXPLICIT FORMS OF THE DIRAC GAMMA MATRICES AND PAULI MATRICES	127
E. PROOFS OF USEFUL DIRAC GAMMA MATRIX TRACE IDENTITIES	129
E.1. Proof of $(\gamma^5)^2 = I_4$	130
E.2. Proof of $\gamma^5 \gamma^\alpha = -\gamma^\alpha \gamma^5$	130
E.3. Proof of $\text{Tr}(\text{odd number of } \gamma \text{ matrices}) = 0$	131
E.4. Proof of $\text{Tr}(\gamma^\alpha \gamma^\beta) = 4\eta^{\alpha\beta}$	132
E.5. Proof of $\text{Tr}(\gamma^\alpha \gamma^\beta \gamma^\delta \gamma^\epsilon) = 4(\eta^{\alpha\beta}\eta^{\delta\epsilon} - \eta^{\alpha\delta}\eta^{\beta\epsilon} + \eta^{\alpha\epsilon}\eta^{\beta\delta})$	133
F. REPRODUCTION OF IMPLEMENTED CODE	134
F.1. Example COSY Deck using ABSPOLY	135
F.2. COSYScript	140
F.3. FORTRAN	151
BIBLIOGRAPHY	188

LIST OF TABLES

Table	Page
1.1 Energy loss table for muons in iron.	18
2.1 G4Beamline scattering distribution parameters.	49
5.1 MICE Step IV coil parameters.	95
5.2 MICE Step IV initial distribution Gaussian parameters.	95
5.3 Run times for MICE Step IV simulation.	99
5.4 Step size dependence for the absorber-coil section of MICE Step IV lattice for liquid hydrogen.	101
5.5 Step size dependence for MICE Step IV lattice.	104

LIST OF FIGURES

Figure	Page		
1.1 The current model of particle physics.	1	3.6 2D histogram of (x, p_x) phase space.	67
1.2 The reference orbit.	5	3.7 Cross section of Figure 3.6 at $p_x = 0.08 \text{ keV}/c$	68
1.3 Example of some map \mathcal{M} creating a bijection from s_0 to s_1 .	7	3.8 Phase space portrait of Figure 3.6.	69
1.4 Example of two maps $\mathcal{M}(s_0, s_1)$ and $\mathcal{M}(s_1, s_2)$. These two maps may be combined together to reduce to a single map, $\mathcal{M}(s_0, s_2)$.	7	3.9 Sample simulation results for the implementation of the transverse coordinate correction algorithm.	69
1.5 Classical muon-target interaction model.	8	3.10 Sample simulation results for the implementation of the temporal displacement algorithm discussed in this section.	71
1.6 Quantum muon-target interaction model.	9	4.1 A flowchart for the structure of the new COSY routines implemented in this work.	73
1.7 Proposed muon accelerator schematics.	11	4.2 Cartoon example of some of the ABSPOLY parameters.	74
1.8 Cartoon of a cooling channel.	12	5.1 Muons of momentum $100 \text{ MeV}/c$ through 1 mm liquid hydrogen. .	78
1.9 Vector diagram illustrating the principle of ionization cooling in Figure 1.8.	13	5.2 Muons of momentum $100 \text{ MeV}/c$ through 10 mm liquid hydrogen. .	79
1.10 $x\text{-}\theta$ phase space examples.	14	5.3 Muons of momentum $100 \text{ MeV}/c$ through 100 mm liquid hydrogen. .	80
1.11 Stopping power curve for antimuons on copper.	17	5.4 Muons of momentum $200 \text{ MeV}/c$ through 1 mm liquid hydrogen. .	81
2.1 Classical model of particle passage through matter.	23	5.5 Muons of momentum $200 \text{ MeV}/c$ through 10 mm liquid hydrogen. .	82
2.2 Plot of $\int w(u)(1 - e^{-pu}) du$.	32	5.6 Muons of momentum $200 \text{ MeV}/c$ through 100 mm liquid hydrogen. .	83
2.3 Example of the Landau function.	34	5.7 Muons of momentum $300 \text{ MeV}/c$ through 1 mm liquid hydrogen. .	84
2.4 Quantum scattering model.	37	5.8 Muons of momentum $300 \text{ MeV}/c$ through 10 mm liquid hydrogen. .	85
2.5 Two parts of Green's function with their poles at $s = \pm k$, altered to be closed by a semicircle at $ s = \pm\infty$.	40	5.9 Muons of momentum $300 \text{ MeV}/c$ through 100 mm liquid hydrogen. .	86
3.1 λ_{max} vs. $\langle \lambda \rangle$ over a variety of liquid hydrogen absorber lengths and initial beam momenta.	55	5.10 Muons of momentum $400 \text{ MeV}/c$ through 1 mm liquid hydrogen. .	87
3.2 Example of the COSY cumulative angular distribution function.	59	5.11 Muons of momentum $400 \text{ MeV}/c$ through 10 mm liquid hydrogen. .	88
3.3 Example of the first iteration of the COSY CDF algorithm.	61	5.12 Muons of momentum $400 \text{ MeV}/c$ through 100 mm liquid hydrogen. .	89
3.4 Example of a muon entering an absorber with some nonzero initial angle.	63	5.13 MuScat angular scattering results for 109 mm of liquid hydrogen compared against COSY (red), G4BL (green), and ICOOL (blue). .	91
3.5 Two examples of true paths.	66	5.14 MuScat angular scattering results for 159 mm of liquid hydrogen compared against COSY (red), G4BL (green), and ICOOL (blue). .	92
		5.15 MuScat angular scattering results for 3.73 mm of beryllium compared against COSY (red), G4BL (green), and ICOOL (blue). .	93
		5.16 MICE Step IV cell.	94

5.17	MICE Step IV x position results for 350 mm of liquid hydrogen.	97
5.18	MICE Step IV x angle results for 350 mm of liquid hydrogen.	97
5.19	MICE Step IV final energy results for 350 mm of liquid hydrogen.	98
5.20	MICE Step IV x position results for 65 mm of lithium hydride.	99
5.21	MICE Step IV x angle results for 65 mm of lithium hydride.	100
5.22	MICE Step IV final energy results for 65 mm of lithium hydride.	100
5.23	Absorber-coil simulation results for x with 10^5 muons and a 5 step propagation.	102
5.24	Absorber-coil simulation results for θ_x with 10^5 muons and a 5 step propagation.	102
5.25	Absorber-coil simulation results for the final energy with 10^5 muons and a 5 step propagation.	103
5.26	MICE simulation results for x with 10^5 muons at 5th order and 50 steps.	104
5.27	MICE simulation results for θ_x with 10^5 muons at 5th order and 50 steps.	105
A.1	Sample scatterplot of a bivariate Gaussian with its projected ellipse.	109
B.1	Feynman diagram for electron-muon scattering.	113
B.2	Mathematical interpretation the three branches of the Feynman diagram in Figure B.1.	114
B.3	COSY treatment of muon-electron scattering.	121

LIST OF SYMBOLS

Symbol	Definition
\mathcal{A}, \mathcal{B}	Matrix, general
a, b_r, d_r, p_g, q_g	GEANT4 angular parameters
b	Impact parameter
b_c	COSY offset of scattering tail
C, C_i	Normalization constant; shell correction parameter)
C_{Euler}	Euler's constant (≈ 0.577)
c	Speed of light in a vaccuum
$\langle dE/dx \rangle$	Energy loss per unit length, mean (Bethe Bloch)
E	Energy (general; context dependent)
e	Fundamental charge (such that $z_{ch} = eQ$)
e^-, e^+	Electron or antielectron
F	Distribution function antiderivative (general; context dependent)
f	Distribution function (general; context dependent)
f_i	Oscillator strengths
$g(E)$	Energy loss distribution function
$g(u)$	Angular distribution function
H	Distribution function antiderivative (general; context dependent)
h	Distribution function (general; context dependent); Planck's constant
h_i	Highland corrections ($i = 1, 2$)

\hbar	Planck's constant divided by 2π	T_{max}	Maximum transferrable kinetic energy
I	Ionization energy (mean)	t	Time (variable)
I_j	Unit matrix of rank j	t_z	True path length
K, K_i	Constant (context dependent)	U	Spinor
L	Length (of absorber or step size)	u	Angular cosine variable ($u = \cos \theta$); dummy variable
ℓ	Time-of-flight in units of length (COSY coordinate)	u_0	Characteristic cosine variable
M	Moments of a function	\vec{v}	Unit vector
\mathcal{M}	Scattering amplitude; transfer map	v	Velocity
m	Mass (general; context dependent)	w	Weight for a distribution function (context dependent)
m_e	Electron mass	X_0	Radiation length
m_μ	Muon mass	(x, y, z)	Beamline position coordinate system
N	Atomic density	Z	Atomic charge
N_A	Avagadro's Number	z_{ch}	Electric charge
N_{el}	Electron density	z_g	Geometric path length
P	Four-momentum	α	Dummy variable
P_k	Legendre polynomials	β	Relativistic velocity ($\beta = v/c$)
p	Momentum (total)	γ	Lorentz factor
(p_x, p_y, p_z)	Beamline momentum coordinate system	γ^α	Dirac gamma matrix
Q_i	Charge number of particle i	δ	Density correction parameter; Dirac function
r_e	Electron radius	ϵ	Energy loss fluctuation ($\epsilon = \Delta E$); emittance
s	Arc length coordinate	ζ	COSY amplitude of scattering tail
T	Transverse coordinate		

η	Minkowski metric
θ	Scattered angle
θ_0	Angular distribution Gaussian width
κ	Vavilov limit parameter
λ	Landau parameter
λ_k	Transport free mean paths, k^{th} value
λ_v	Vavilov parameter
μ	Mean; muon
$\nu_e, \bar{\nu}_e$	Electron neutrino or electron antineutrino
ν_μ	Muon neutrino
π	Circle constant
ρ	Density
Σ	Cross section
σ	Standard deviation
σ^j	Pauli matrices
ϕ	Laplace transformed function
ψ	Wavefunction, time-independent component
Ω	Solid angle
$*$	Complex conjugate
\dagger	Transpose conjugate
T	Transpose of a matrix

ABSTRACT

COSY Infinity is an arbitrary-order beam dynamics simulation and analysis code. It can determine high-order transfer maps of combinations of particle optical elements of arbitrary field configurations. For precision modeling, design, and optimization of next-generation muon beam facilities, its features make it a very attractive code. New features are being developed for inclusion in COSY to follow the distribution of charged particles through matter. To study in detail some of the properties of muons passing through material, the transfer map approach alone is not sufficient. The interplay of beam optics and atomic processes must be studied by a hybrid transfer map-Monte Carlo approach in which transfer map methods describe the average behavior of the particles in the accelerator channel including energy loss, and Monte Carlo methods are used to provide small corrections to the predictions of the transfer map accounting for the stochastic nature of scattering and straggling of particles. The advantage of the new approach is that it is very efficient in that the vast majority of the dynamics is represented by fast application of the high-order transfer map of an entire element and accumulated stochastic effects as well as possible particle decay. The gains in speed shown in this work are expected to simplify the optimization of muon cooling channels which are usually very computationally demanding due to the need to repeatedly run large numbers of particles through large numbers of configurations. This work describes the development of the required algorithms and their application to the simulation of muon ionization cooling channels. The code is benchmarked against other codes, validated with experimental results, and predicts results for current muon ionization cooling efforts.

CHAPTER 1

INTRODUCTION

1.1 Muon-based Accelerators

Muons (μ) were first discovered experimentally in 1947 by Powell *et al.* [1]. They were looking for the Yukawa meson. It is now known that muons fit into a particle group called leptons, and fit into the standard model (along with other fundamental particles) as shown in Figure 1.

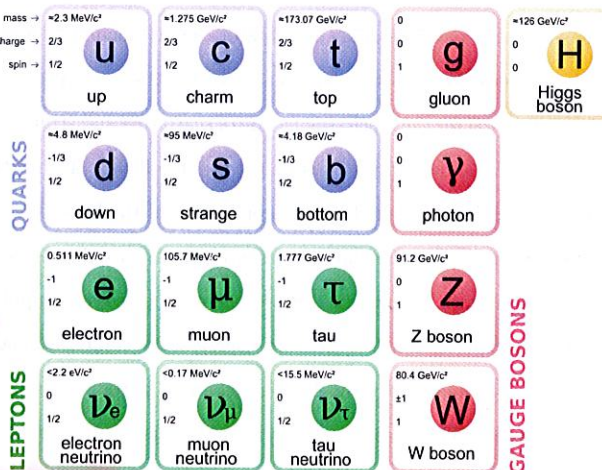


Figure 1.1: The current model of particle physics. Image courtesy of [2].

Similar to the electron (e), the muon carries a fundamental charge of ± 1 , a total spin of $1/2$, and observes the electromagnetic and weak forces. Moreover, the muon also has a corresponding neutrino: the muon neutrino (ν_μ). However, the muon (mass = $105.7 \text{ MeV}/c^2$) is about 200 times heavier than the electron (mass = $0.511 \text{ eV}/c^2$).

MeV/c^2). Indeed, sometimes it is useful to think of a muon simply as a heavy electron, but the mass implies several unique characteristics. One of these is the instability of muons, and results in muons decaying into an electron, an electron antineutrino, and a muon neutrino:

$$\mu \rightarrow e + \bar{\nu}_e + \nu_\mu.$$

This is quite interesting, as it means muons are a double-edged sword. On the one hand, their point-like nature means that ~~the muon~~ collisions are clean. That is to say, muon colliders have a great advantage over, e.g., proton colliders since protons are composed of three quarks. Each quark may have a different flavor or energy level and hence adds more variables to the analysis. Furthermore, each quark is bound and so gluon interactions must also be considered. These quarks and gluons may undergo hadronization when interacting with one another, creating a plethora of possible hadrons. Hadronization is not fully understood, and so these sprays of hadrons are typically lumped together as a single “jet”. While there are many working models for jet analysis, none are exact. Conversely, any data from muon interactions will have relatively little noise and will not produce jets.

Clean collisions can also be achieved with linear electron ~~colliders~~. Yet unlike the electron, the muon does not emit a large amount of synchrotron radiation as it is accelerated. This is because the power irradiated on a particle due to synchrotron radiation is inversely proportional to the mass of the particle to the fourth power [3]:

$$P \propto 1/m^4.$$

Therefore, the relative power loss due to synchrotron radiation for electrons and muons is $P_e/P_\mu \propto m_\mu^4/m_e^4 \approx 10^{30}$. Since muons lose power via synchrotron radiation at roughly one-billionth the rate of electrons, it is ~~possible to have a~~ circular muon accelerator. Furthermore, due to the small mass of a muon compared to a proton

~~should use human rather than computer notation~~

~~also possible for electrons \rightarrow much more quantitative discussion~~

($\sim 105 \text{ MeV}/c^2$ vs. $\sim 938 \text{ MeV}/c^2$), muons are easier to accelerate. This means that a muon facility can be much smaller than its proton counterpart.

~~wrong reason~~

this work is

However, there is one problem with a muon accelerator. A rest frame lifetime of $2 \mu\text{s}$ requires the muons to be accelerated quickly before they decay. This is a challenge for circular colliders which require a high-intensity beam.

~~1st~~

Overall, it appears that there are several advantages and one key disadvantage:

the $2 \mu\text{s}$ mean rest frame lifetime of the muon. However, this is only a disadvantage for muon colliders. Another application, which turns the moderately short lifetime

into an advantage, is a neutrino factory. This is a facility that is dedicated to the output of a neutrino beam. Muons have two primary advantages over fission reactor neutrino sources. The first is that muons decay into exactly two flavors of neutrino: electron and muon. Therefore, the initial composition of the neutrino beam would be well-defined. This is important since neutrinos can change their flavors over time. Secondly, since neutrinos have no electric charge, they cannot be manipulated via electromagnetic focusing methods. However, the beam of muons can be focused into a high-intensity beam, and the intensity of the neutrino beam will reflect this.

~~of II don't be
of II more quantitative~~

1.2 COSY Infinity

COSY Infinity is a beamline simulation tool used in the design, analysis, and optimization of particle accelerators [4]. COSY uses the transfer map approach, which evaluates the overall effect of a system on a beam of particles using differential algebra. This involves expanding an ordinary differential equation into multivariate Taylor polynomials up to arbitrary order [5]. Each particle in this work is represented by its coordinates as a phase space vector. The form of phase space vectors used in

~~wrong comparison
produces angle
(assumed small)~~

$$\mathbf{Z} = \begin{pmatrix} x \\ y \\ l = k(t - t_0) \\ a = p_x/p_0 \\ b = p_y/p_0 \\ \delta = (E - E_0)/E_0 \end{pmatrix}, \quad (1.1)$$

where the coordinates are transverse positions (x, y), time-of-flight in units of length (l), transverse angles w.r.t. the reference particle (a, b), and kinetic energy deviations w.r.t. the reference particle (δ). The 0 subscript in the definitions denotes the reference particle properties.

In beam physics, phase space vectors \mathbf{Z} are subject to physics processes. This ~~subjugation~~ can usually be represented by a differential equation. For example, a particle in an electric field is subject to the force law [3]

$$\mathbf{F} = Q(\mathbf{E} + \mathbf{v} \times \mathbf{B}),$$

or in terms of the momentum,

$$\frac{d}{dt}\mathbf{p} = Q(\mathbf{E} + \frac{1}{m}\mathbf{p} \times \mathbf{B}).$$

Fortunately, ~~any phase space vector \mathbf{Z} is~~ an arbitrary order ordinary differential equation (ODE) ~~can be rewritten as a first order ODE~~ [5]. For an order n ODE, a first-order ODE is constructed by introducing $n - 1$ new variables. This is to say that

$$\frac{d^n}{dt^n}\mathbf{Z} = f\left(\frac{d^0}{dt^0}\mathbf{Z}, \dots, \frac{d^{n-1}}{dt^{n-1}}\mathbf{Z}\right)$$

~~use X1084, Wright~~

can be rewritten as

$$\frac{d}{dt} \begin{pmatrix} Z \\ Z_1 \\ \vdots \\ Z_{n-1} \end{pmatrix} = \begin{pmatrix} Z_1 \\ Z_2 \\ \vdots \\ f(Z, \dots, Z_{n-1}) \end{pmatrix}.$$

Here, f represents the physics processes. For the Maxwell's equations example, the equation is already first order in a and b , with the momentum component of f as

$$f(p) = Q(E + \frac{1}{m} p \times B) = Q(E + \frac{1}{m} [ap_0\hat{x} + bp_0\hat{y} + p_z\hat{z}] \times B).$$

Furthermore, COSY does not use time as the independent variable, but rather arc length s (see Figure 1.2).

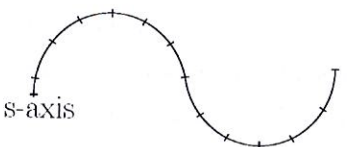


Figure 1.2: The reference orbit. Figure courtesy of [6].

If there exists a unique evolution of Z then it is possible to construct the so-called transfer map \mathcal{M} . Mathematically, this relationship is $Z(s) = \mathcal{M}(s_0, s) * Z(s_0)$, with $*$ representing the application of the transfer map to the phase space vector Z at s_0 .

It is possible to construct a transfer map for most cases in beamline physics. This is because most beamline elements follow differential equations which yield unique solutions dependent on initial conditions (such as Maxwell's equations). If there does not exist a unique evolution of Z then it is not possible to construct the

transfer map. Systems which produce a unique evolution of Z are called "deterministic".

An example of the relationship between the initial phase space vector, the transfer map, and the final phase space vector can be seen in Figure 1.3. The initial phase space occupied by the beam of particles is at the coordinate s_0 . Physically, there exists some deterministic beamline element between s_0 and s_1 . This element can be represented by the map \mathcal{M} , which creates a bijection for the phase space vectors $Z(s_0)$ and $Z(s_1)$ between the initial coordinate s_0 and the final coordinate s_1 .

Entire lattices may also be represented by a single transfer map. This is done by dividing the lattice into its base components or elements. A transfer map for each corresponding element may then be produced. For two example elements between coordinates s_0 and s_2 (see Figure 1.4), the composition of two maps yields another map: $\mathcal{M}(s_1, s_2) * \mathcal{M}(s_0, s_1) = \mathcal{M}(s_0, s_2)$. Therefore, it is possible to simplify the middle part s_1 . In this way, the transfer maps from small components build up into a single transfer map for the whole system. Computationally this is advantageous because once calculated, it is much faster to apply a single transfer map to a distribution of particles than to simulate that same distribution through many meters of individual lattice elements.

Along with the tracking of particles through a lattice, COSY also has a plethora of analysis and optimization tools, including (but not limited to) lattice aberration and correction tools, support for Twiss parameters, support for tunes and nonlinear tune shifts, built-in optimizers for lattice design, and spin tracking.

Valid elements are any beamline elements that are deterministic. Elements used in this study are magnetic multipoles (dipoles, quadrupoles, etc.), solenoidal coils, radiofrequency (RF) cavities, and drifts. Currently supported elements in COSY

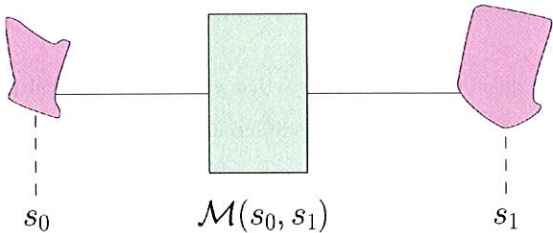


Figure 1.3: Example of some map \mathcal{M} creating a bijection from s_0 to s_1 .

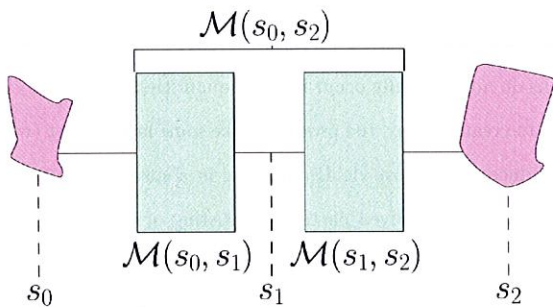


Figure 1.4: Example of two maps $\mathcal{M}(s_0, s_1)$ and $\mathcal{M}(s_1, s_2)$. These two maps may be combined together to reduce to a single map, $\mathcal{M}(s_0, s_2)$.

include but are not limited to: various magnetic and electric multipoles (with or without fringe effects), homogeneous and inhomogeneous bending elements, Wien

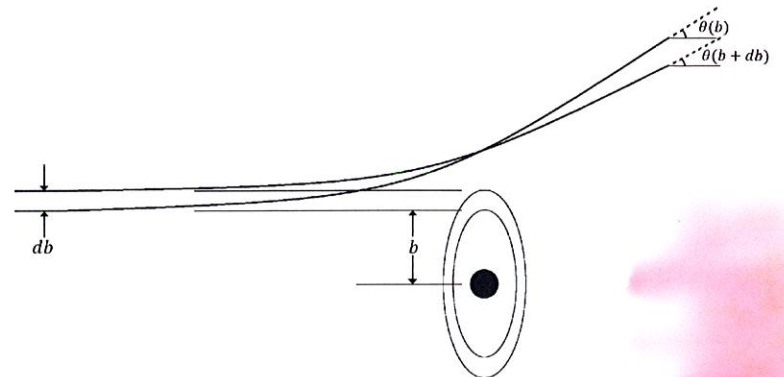


Figure 1.5: Classical muon–target interaction model courtesy of [9].

filters, wigglers and undulators, cavities, cylindrical electromagnetic lenses, general particle optical elements, and deterministic polynomial absorbers of arbitrary order.

1.3 Introduction to Matter-Dominated Lattices

1.3.1 Introduction to Stochastic Effects. This section introduces stochastic effects, or effects that are intrinsically random. These effects are in contrast to deterministic effects, which are not random and hence can be predicted exactly.

This work concerns the interactions between a muon beam and some stationary target called the ‘absorber’—typically a cylinder or wedge of a material with low nuclear charge (Z) such as liquid hydrogen or lithium hydride. The simplest model of a beam interacting with some stationary target can be found in several textbooks [7,8], with the model from [9] illustrated in Figure 1.5.

In this figure, b is referred to as the impact parameter and is measured with respect to the particle’s initial trajectory. For a beam of noninteracting particles

*don't mix
UK + US
quote conventions*

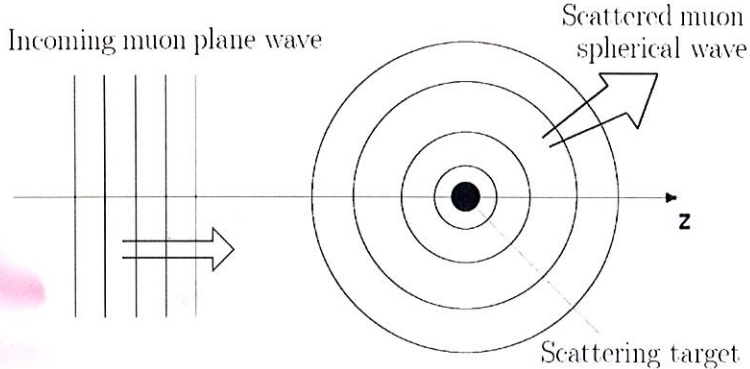


Figure 1.6: Quantum muon–target interaction model. The incoming particle wavefunction is represented as a plane wave and is scattered locally as a spherical wave. Image courtesy of [8].

and a perfectly stationary target, classical mechanics suggest that this is a purely deterministic problem (see, e.g., ‘hard-sphere scattering’ in [8]); the particle with a smaller impact parameter b deflects more than its neighbor with a slightly larger impact parameter $b + db$. Since this model is entirely based on initial conditions, it would be relatively easy to implement these effects into the map methods of COSY Infinity. However, reality does not follow the model of Figure 1.5. A more accurate model is illustrated by Figure 1.6. Here the target is still approximated as fixed, but the incident particle is now approximated as a travelling plane wave and the scattered particle is approximated as a spherical wave (at least locally). It is shown later that this model predicts

1. a spectrum of energy loss $\omega(\epsilon)$ which yields the probability of losing an amount of energy ϵ (see Section 2.1), and

2. a scattering amplitude which gives the shape of the probability distribution of scattering in a given direction θ (see Section 2.2).

Hence quantum theory suggests that even if two identical particles have identical initial conditions their final conditions are not the same.

1.3.2 Muon Ionization Cooling. In Section 1.1, the primary disadvantage to the considered muon-based accelerator was the mean muon rest frame lifetime ($2 \mu\text{s}$). This is expected to be far too short of a timespan to be useful in a traditional accelerator scheme since the muons must be collected, focused, and accelerated. For the moment, observe the two proposed schematics in Figure 1.7 [10]. The section labeled ‘Proton Driver’ produces protons, which will eventually yield muons. This is essential since muons do not naturally occur in great quantities at a convenient extraction point. In order to create muons, the protons strike some large target (which must be optimized to produce the highest yield), resulting in a spray of protons, muons, electrons, and pions (even shorter-lived particles consisting of a quark-antiquark pair). To further optimize this process, it is advantageous to let the pions decay into muons via $\pi^+ \rightarrow \mu^+ + \nu_\mu$. The resulting ensemble of muons is then split up into bunches. The next section in Figure 1.7 is the focus of this thesis. For now, it is simply addressed as the cooling channel and delved into later. Cooling the beam simply means reducing the beam’s phase space. Reducing the momentum of the beam results in a reduced physical size. The purpose of cooling is to increase the density of the resulting beam. This lets the beam fit into smaller magnets, which are less expensive than larger magnets. However, this increase in density also increases the luminosity of the beam in the long run. For a collider, this means more collisions; for a neutrino factory, this means more neutrino counts in the detectors (since neutrinos are neutral, there is no way to focus a neutrino beam once created). After the beam of muons is focused it is accelerated to an appropriate energy. For a neutrino factory, this is 5 GeV, and

But they travel $c \approx c$!

*I volume
how?
Not my
also
RF*

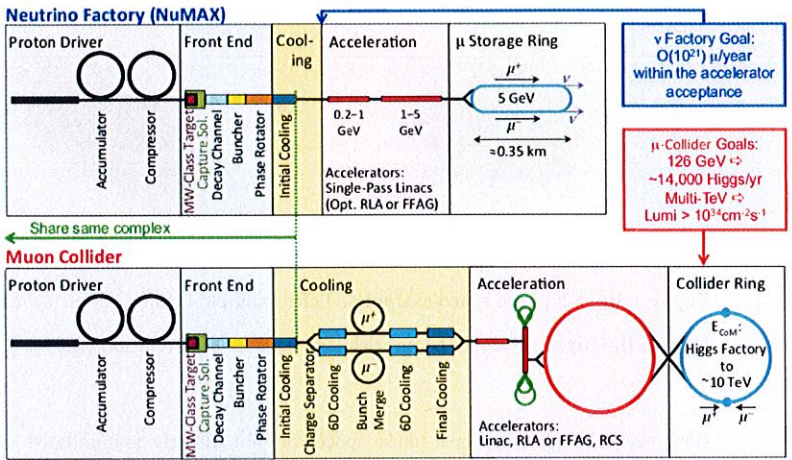


Figure 1.7: Proposed muon accelerator schematics. The neutrino factory (top) is designed to produce high-intensity beams of neutrinos. The muon collider (bottom) is designed to produce high energy high-intensity beams of muons for, e.g., Higgs production. The muon collider demands more cooling and acceleration due to the higher intensity and energy threshold requirements of high energy physics. Image courtesy of [10].

the muon and antimuon beams are allowed to decay in a storage ring. For a muon collider, the center-of-momentum energy is ~ 126 GeV for a Higgs factory or up to 10 TeV for high energy studies.

The cooling channel is the crux of the entire operation for either purpose. Ionization cooling is the only cooling technique fast enough to work within the average muon lifetime. Ionization cooling requires the beam to deposit its energy in matter, thus ionizing the matter.

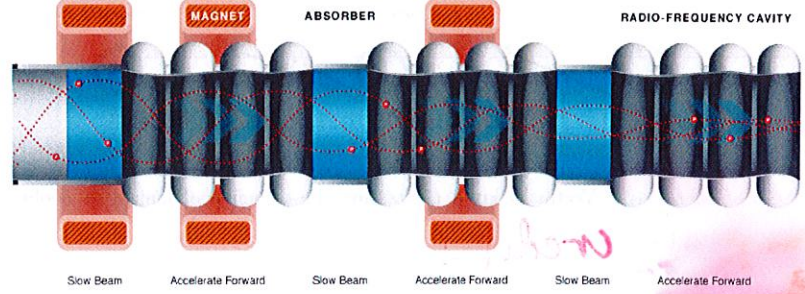


Figure 1.8: Cartoon of a cooling channel, courtesy of [10].

While the idea of ionization cooling has been around since at least 1956 [11,12], it did not appear to be a viable option until roughly 1970 [13]. It was believed that multiple scattering effects would mask any cooling benefits. Scattering is a quantum effect in which two objects are deflected when they are in close proximity at high energies, and hence is intrinsically random. This means that while the energy deposition reduced the beam's phase space, the beam would also grow in the transverse direction due to this multiple scattering.

Now, this seems to be quite the opposite of what is intended; ionization cooling potentially produces a slow, fat beam, and an effective muon beam should be narrow and fast so that the Lorentz boost keeps the muons from decaying. Fortunately, these problems can be solved simultaneously. The overall cooling scheme is presented in Figure 1.8 and the vector describing the change in momentum is depicted in Figure 1.9.

The key is to use a cell which contains both the ionizing material and a radio frequency cavity. To understand why this solves the problem of potentially producing a beam with a large transverse phase space, it is necessary to observe Figure 1.9. In

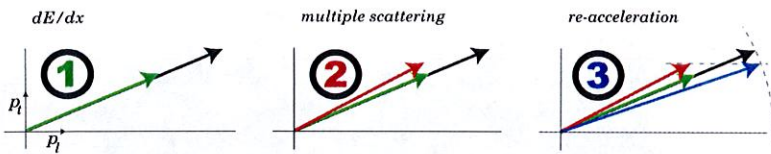


Figure 1.9: Vector diagram illustrating the principle of ionization cooling in Figure 1.8. *credit 7*

Figure 1.9, the longitudinal momentum (p_l) is plotted against the transverse momentum (p_t).

1. Beam deposits energy in material, reducing the momentum in all directions.
2. Multiple scattering effects are observed. The transverse phase space increases (or heats up). By a clever choice of absorbing material (as discussed in the next section), the growth of the transverse phase space is kept to a minimum at this stage.
3. The beam is re-accelerated by the radiofrequency cavity, increasing the longitudinal momentum only. The result is a reduction in transverse momentum (i.e. blue vector compared to black vector). This solves the problem of having a large transverse phase space. Moreover, re-acceleration solves the problem of decay: after the beam loses energy, it gains that much energy again, and so the Lorentz boost stays constant on average.

1.4 Emittance

Emittance (ϵ) is a measure of the volume of phase space occupied by the beam.

It is sometimes beneficial to normalize the emittance by the relativistic factors, γ and β . This is useful because when a beam accelerates the transverse angles decrease. This results in a reduction of ϵ_x (where x represents the general transverse direc-

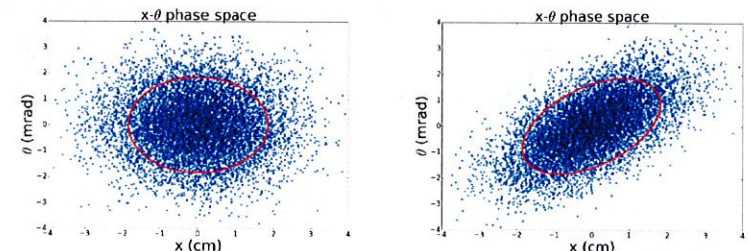


Figure 1.10: $x\theta$ phase space examples. Left: example beam with no $x\theta$ correlation ($\langle x\theta \rangle = 0$). Right: example beam with significant $x\theta$ correlation ($\langle x\theta \rangle = 0.8$).

tion) even though transverse phase space was not directly manipulated. However, ϵ_x^N stays constant when a beam accelerates, and hence gives an invariant measure characterizing the beam. For the relevant transverse emittance,

$$\epsilon_x^N = \beta\gamma\epsilon_x = \beta\gamma\sqrt{\langle x^2 \rangle \langle \theta^2 \rangle - \langle x\theta \rangle^2}. \quad (1.2)$$

Here, azimuthal symmetry is assumed, and so x represents the general transverse position, and $\theta = \sin^{-1} p_x/p$ is the projection of the divergence angle of the particle trajectory onto the x - z plane, where z is the longitudinal Cartesian coordinate.

The full derivation of the emittance in Eq. (1.2) can be found in Appendix A. Qualitatively, if there exists no cross-dependence in x and θ , then the distribution should be a non-tilted ellipse. Then the emittance is proportional to the geometric mean, $\sqrt{\langle x^2 \rangle \langle \theta^2 \rangle}$. However, if there is some cross-dependence then the result is a tilted ellipse. For a sample comparison of tilted vs. non-tilted ellipses, see Figure 1.10. Here, the emittance is outlined in red.

The goal is to observe the evolution of the emittance through an absorber. Taking the expression for the rate of change of normalized transverse emittance over

better to cite original source (Neuffer)

a length z from [14],

$$\frac{d\epsilon_x^N}{dz} = \frac{\beta_\perp}{2} \frac{E_s^2}{\beta^3 Emc^2} \frac{1}{X_0} - \frac{1}{\beta} \left| \left\langle \frac{dE}{dz} \right\rangle \right| \frac{\epsilon_x^N}{E},$$

where $\beta = v/c$ is the relativistic velocity, β_\perp is the transverse betatron function, E_s is some characteristic energy (usually 14 MeV), E is the (mean) energy of the beam, m is the mass of the beam species, X_0 is the radiation length of the absorber material, and $\langle dE/dz \rangle$ is the mean energy loss of the beam through the absorber. The first term represents 'heating' and the second term represents 'cooling' in the transverse plane.

Starting with the first term,

$$\frac{d\epsilon_x^N}{dz} (\text{heat}) = \frac{\beta_\perp}{2} \frac{E_s^2}{\beta^3 Emc^2} \frac{1}{X_0}. \quad (1.3)$$

Now it is clearer why this is referred to as the heating term. Since the derivative of emittance is positive, this part represents emittance growth. Moreover, to reduce this growth it is necessary to have highly energetic particles through a material with a large radiation length (typically $X_0 \propto 1/Z$ (nuclear charge)).

Now for the second term:

$$\frac{d\epsilon_x^N}{dz} (\text{cool}) = -\frac{1}{\beta} \left| \left\langle \frac{dE}{dz} \right\rangle \right| \frac{\epsilon_x^N}{E}. \quad (1.4)$$

Similarly to the heating term, it is now understandable why this is referred to as the cooling term. The rate of change of the normalized transverse emittance is negative, and so the transverse phase space shrinks. However, at this point Eq. (1.4) does not explain precisely how the rate changes, and so is purely conceptual. The shape of the cooling term is determined by the average energy loss, $|\langle dE/dz \rangle|$. However, usually it is not $|\langle dE/dz \rangle|$ that is measured, but rather the stopping power $S(E) = -\frac{1}{\rho} \langle dE/dz \rangle$, typically in units of MeV·cm²/g. A good example of a stopping power curve can be seen in

No verb

No such form

should punctuate consistently

No
A distinction without difference!
g is non-controversial!

Figure 1.11 [15]. For this example, there are several effects noted in Figure 1.11. One may be tempted to think that based on 1.11 the most cooling should occur in the Anderson-Ziegler regime at $\beta\gamma \sim 0.01$. This may seem correct since there is a $1/E$ dependence in Eq. (1.4), and so the high energy part of the curve is not advantageous. Indeed, for $\rho = 8.92 \text{ g/cm}^3$ it is easy to see that at $\beta\gamma = 0.01$

$$\frac{d\epsilon_x^N}{dz} (\text{cool}) \approx -900 \text{ cm}^{-1} \cdot \epsilon_x^N.$$

Not obvious - see argument on next slide

However, the correct strategy is just the opposite—one should endeavor to build a cooling cell with the minimum ionization point in mind (in the Bethe regime, where $\beta\gamma \sim 2$). At the peak ($\beta\gamma \sim 0.01$), the muon beam slows down quite a bit through a single cooling cell and one is at risk of losing the beam to decay. Moreover, Figure 1.11 only depicts the stopping power, not the actual energy loss that individual particles experience. The individual energy loss is a stochastic effect, and the distribution of energy losses broadens with decreasing beam energy. This means that for lower energies, there are more particles that stop completely. Finally, Eq. (1.3) suggests that higher energies are better since they reduce the heating term. For these reasons, it is apparent that a muon cooling cell should be made of low-Z materials such as liquid hydrogen or lithium hydride and operate anywhere between 100 MeV/c and 400 MeV/c. There are more issues

When particles impinge upon a fixed target, they lose some of their energy. For massive particles like muons, there are a number of major effects that contribute. However, it is important to note that in the muon cooling regime only ionization contributes significantly to the energy loss. To see this, take for an example the relatively heavy element of iron. In Table 1.1, the energy loss contributions of these

¹While iron would not likely be used as an absorber material, it serves as an exaggerated example due to its Z value of 26.

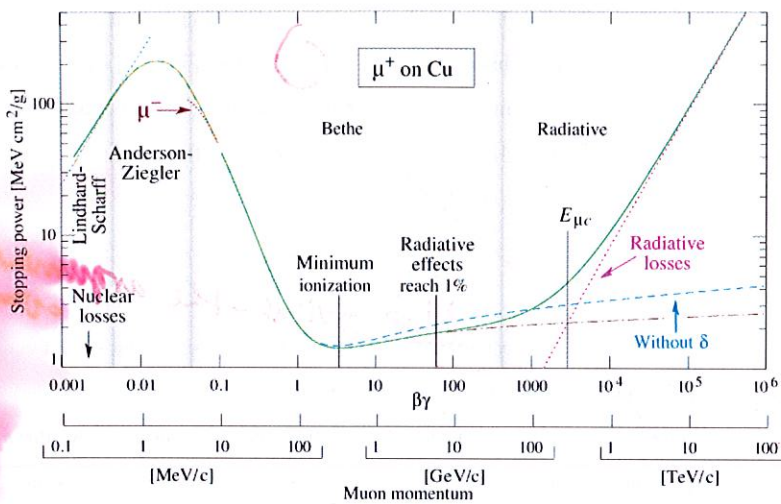


Figure 1.11: Stopping power curve for antimuons on copper, courtesy of [15].

four effects can be seen. However, the non-ionization effects only start to contribute at an initial beam kinetic energy of 1.40 GeV—far outside of the muon cooling regime.

This is a good example because all of the cooling materials currently being considered have less muon stopping power than iron. This means that iron represents the maximum contribution of non-ionization energy loss per initial beam energy; that is, the non-ionization effects begin to emerge at much higher energies for lighter materials such as liquid hydrogen. Note that Figure 1.11 may also be useful when discussing this subject, as the minimum ionization regime is explicitly characterized.

1.5 Looking Forward

In short, this work uses basic principles to successfully implement muon ionization cooling simulation tools into COSY Infinity. The algorithms which have been implemented are derived from first or second principles as can be seen from other codes

means what?

non seq

Muons in Iron (Fe)

T MeV	p MeV/c	Ionization	Brems	Pair prod	Photonucl	Total	CSDA range g/cm²
10	47.04	5.494				5.494	1.025
14	56.16	4.321				4.321	1.854
20	68.02	3.399				3.399	3.437
30	85.09	2.654				2.654	6.812
40	100.3	2.274				2.274	10.91
80	152.7	1.717				1.717	31.78
100	176.4	1.616				1.616	43.82
140	221.8	1.516				1.516	69.50
200	286.8	1.463				1.463	109.9
274	364.2	1.451				1.451	Min. ionization
300	391.7	1.452				1.453	178.7
400	494.5	1.467				1.467	247.2
800	899.5	1.548				1.548	512.4
1000	1101	1.581	0.001			1.582	640.2
1400	1502	1.635	0.001		0.001	1.637	888.5

Table 1.1: Energy loss table for muons in iron, T MeV. Courtesy of [16]. The first two columns show T , the kinetic energy of the beam, and p , the corresponding momentum of the beam. The next four columns show the various contributions to energy loss, with column 7 giving the total energy loss. Finally, column 8 shows the range of muons through the material calculated by the continuous slowing down approximation.

WRONG
PROPOSITION

in Chapter 2 and novelly in Chapter 3. Furthermore, these algorithms are augmented by fitting the results to experimental data and benchmarking against external sources. The results of benchmarking and validation are discussed in Chapter 5. Here it is shown that the new routines in COSY produce robust, accurate, and fast simulations.

Great! Have you published?
Sounds like you should!

~~wherein~~

CHAPTER 2

STOCHASTIC PROCESSES IN OTHER CODES

In this chapter, the two major stochastic processes—energy straggling and multiple scattering—are detailed. Because there are so many models for these two key processes, two case studies are shown as a frame for their derivations. Both of these ~~codes~~ use particle-by-particle propagation and do not use the transfer map method discussed in Section 1.2.

The first case study is ICOOL [17] and covers the classic models. Much of the classic theory is also used in the new COSY routines. Consequently, the sections concerning ICOOL serve as a foundation for the derivations in Chapter 3. ICOOL was created at Brookhaven National Laboratory for the benefit of the members of the Neutrino Factory and Muon Collider Collaboration, who specifically study ionization cooling problems.

The second case study is G4Beamline [18], which is based on GEANT4 [19]. GEANT4 implements a more novel approach. Many of the routines use empirically-tuned parameters. Consequently, G4Beamline is accurate for a variety of particles over a wide range of energies. It should be noted that muons, for which there is little experimental data available, are usually grouped with protons as heavy charged particles. Therefore, for lack of experimental data, muons use the same routines as protons.

2.1 Energy Straggling in ICOOL

ICOOL [17] employs four straggling models, three of which were used in these muon simulations studies. Discussed below, these are

1. Gaussian (Bohr),
2. Landau distribution, and
3. Vavilov distribution (with appropriate limits).

The fourth model was not considered for this study.

2.1.1 Gaussian (Bohr) Straggling Model. ~~The first model uses a Gaussian function to model the energy loss distribution. Recall that Gaussian distributions are defined by two parameters: the standard deviation σ and the mean μ .~~

According to [19], the first of these is given by:

$$\sigma^2 = 2\pi e^2 N_A T_c \frac{Z\rho L}{A} \frac{1 - \beta^2/2}{\beta}, \quad (2.1)$$

where e is the fundamental electric charge, N_A is Avogadro's number, T_c is the cut kinetic energy of δ -electrons, Z is the nuclear charge, ρ is the density of the material, L is the length of the material, A is the nuclear mass, and $\beta = v/c$ is the relativistic speed.

The mean comes from the Bethe-Bloch equation [20], which is derived here and yields Eq. (2.5). The derivation is the so-called classical derivation, which takes first principles and mechanically derives an expression. The classically-derived intermediate equation is then subject to modern corrections, which account for the approximations made or phenomena neglected during the classical derivation.

Classical Derivation

The process begins with a particle of charge e moving through a material. It is assumed that the mass of the incoming particle is much greater than the mass of the electron since scattering is neglected in this derivation. Moreover, the electron must either be at rest and fixed into place (which is nonphysical) or the collision time

of the particle and electron must be very small compared to the electron orbital time. The longitudinal (z) axis is aligned with the particle velocity such that $v_x = v_y = 0$. The momentum transfer Δp from the incoming particle to the orbiting electron is sought via

$$\Delta p = \int_{-\infty}^{\infty} F dt.$$

~~net~~

The first observation is that the ~~change~~ in the longitudinal force on the particle is zero. This is true since the particle feels an average force "forward" just as much as it feels a force "backward" due to symmetry. Explicitly, this is equivalent to saying that $F_z(z) = -F_z(-z)$. For this reason, any change in momentum is solely due to the transverse force. Again following Figure 2.1,

$$\Delta p = \int_{-\infty}^{\infty} F_x dt = \int_{-\infty}^{\infty} F_x \frac{dz}{v} = \int_{-\infty}^{\infty} F \cos \theta \frac{dz}{v},$$

Observe from Figure 2.1 that $\cos \theta = b/r$. Then

$$\begin{aligned} \Delta p &= \int_{-\infty}^{\infty} \frac{e^2 b}{r^2 r} \frac{dz}{v} = \int_{-\infty}^{\infty} \frac{e^2}{z^2 + b^2} \frac{b}{\sqrt{z^2 + b^2}} \frac{dz}{v} \\ &= \frac{e^2 b}{v} \int_{-\infty}^{\infty} \frac{1}{(z^2 + b^2)^{3/2}} dz. \end{aligned}$$

By substitution of the following

$$\begin{aligned} z &= b \tan \theta, & dz &= b \sec^2 \theta d\theta, \\ z = -\infty &\rightarrow \theta = -\frac{\pi}{2}, & z = \infty &\rightarrow \theta = \frac{\pi}{2}. \end{aligned}$$

the integral becomes

$$\begin{aligned} \Delta p &= \frac{e^2 b}{v} \int_{-\pi/2}^{\pi/2} \frac{b \sec^2 \theta d\theta}{(b^2(\tan^2 \theta + 1))^{3/2}} = \frac{e^2 b}{v} \int_{-\pi/2}^{\pi/2} \frac{d\theta}{b^2 |\sec \theta|} \\ &\cancel{=} \frac{2e^2}{vb}. \end{aligned}$$

~~This~~ The non-relativistic approach yields the energy loss for the interaction between a muon and a single bound electron:

$$\epsilon = \frac{\Delta p^2}{2m} = \frac{2e^4}{v^2 b^2 m_e}. \quad (2.2)$$

~~Explain why not m_m ?~~
NO

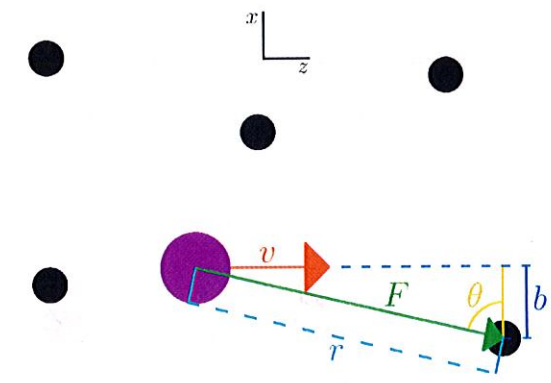


Figure 2.1: Classical model of particle passage through matter.

~~Here, it is useful to note that if the interaction of the muon with the nucleus was desired, ϵ for a single interaction would be proportional to Z^2/m_{nuc} and would be added on to Eq. (2.2).~~ However, since $1/m_e \gg 1/m_{nuc}$ the second term is disregarded.

Observe from Figure 2.1 that only a single electron has been considered for Eq. (2.2). For multiple electrons, the average electron density is $N_{el} = N_A \cdot Z\rho/A$, where N_A is Avogadro's number, Z is the nuclear charge, ρ is the density of the material, and A is the nuclear mass. From this expression the average energy loss may be obtained. The cylindrical symmetry of the system is exploited by integrating the single electron interaction in cylindrical coordinates, with θ as the cylindrical angle, b (the impact parameter) as radius, and z as length. The bounds are $\theta \in [0, 2\pi]$, $z \in [0, L]$ (where L is the total length of material traversed), and $b \in [b_{min}, b_{max}]$ (which is discussed

shortly). Then

$$\langle \epsilon \rangle = \int_{b_{min}}^{b_{max}} \int_0^L \int_0^{2\pi} \frac{2e^4}{v^2 b^2 m_e} N_{el} d\theta dz db$$

$$= \frac{4\pi N_A e^4 Z\rho L}{v^2 m_e A} \int_{b_{min}}^{b_{max}} \frac{db}{b}. \quad (2.3)$$

reassumed?

It is known that b_{min} comes from the maximum amount of energy (T_{max}) which a muon may impart upon an electron. This quantity is derived later and can be seen in Eq. (2.8), but is only symbolic here. Similarly, the minimum transferrable energy is taken as the mean ionization energy, I , which is usually an empirical value. Any energy below this value does not transfer, since this is the minimum amount of energy to free the electron from its orbit. Then

$$\epsilon_{max} = \frac{2e^4}{v^2 b_{min}^2 m_e} = T_{max},$$

$$b_{min} = \frac{e^2}{v} \sqrt{\frac{2}{m_e T_{max}}},$$

$$\epsilon_{min} = \frac{2e^4}{v^2 b_{max}^2 m_e} = T_{min} = I,$$

$$b_{max} = \frac{e^2}{v} \sqrt{\frac{2}{m_e I}}.$$

derived? justified? obtained?

Even worse...

Thus

Once the bounds have been acquired, the integral in Eq. (2.3) is solvable.

$$\langle \epsilon \rangle = \frac{4\pi N_A e^4 Z\rho L}{v^2 m_e A} \int_{b_{min}}^{b_{max}} \frac{db}{b},$$

$$\langle \epsilon \rangle = \frac{4\pi N_A e^4 Z\rho L}{v^2 m_e A} \ln \frac{b_{max}}{b_{min}},$$

$$\langle \epsilon \rangle = \frac{2\pi N_A e^4 Z\rho L}{v^2 m_e A} \ln \frac{T_{max}}{I}. \quad (2.4)$$

Modern Corrections

There are a number of corrections to the Bethe-Bloch equation. The first is a correction under the logarithm due to the relativistic flattening of the incoming

Why? or give citation

particle's electric field. This factor is $\frac{2m_e\beta^2\gamma^2}{I}$. Another correction is known as the density correction δ and arises due to polarization of the material. This is important for high energies since it can limit the range of the flattened electric field in the material. The last correction is the shell correction C and accounts for the fact that the electron is not at rest (or the interaction time is not much faster than the electron orbit). This is important for low energies. These corrections may or may not have a large impact on these medium energy studies since the logarithmic and density corrections arise at high energies and the shell correction occurs at low energies. Finally, in its more familiar form, the constants in Eq. (2.4) are condensed into a single constant $K = \frac{2\pi e^4 N_A}{m_e} \approx 15.4 \text{ (MeV} \cdot \text{cm}^3\text{)/(m} \cdot \text{g)}$. Since the model assumes natural units (i.e., $c = 1$), v^2 is usually replaced with β^2 . Moreover, to avoid confusion $\langle \epsilon \rangle$ is given a negative sign in order to emphasize energy loss.

The ultimate result is the Bethe-Bloch equation for the average energy lost by a particle traversing some medium with correction factors:

$$\langle \epsilon \rangle = -\frac{K Z \rho L}{\beta^2 A} \left(\ln \frac{2m_e\beta^2\gamma^2 T_{max}}{I^2} - 2\beta^2 - \delta - 2\frac{C}{Z} \right). \quad (2.5)$$

According to the Particle Data Group [15], this equation is generally accurate for intermediate Z materials (within up to a few % when compared to experimental data) in the energy regime of $0.1 \lesssim \beta\gamma \lesssim 1000$. The lower limit of this equation is reached when the incoming particle velocity is comparable to the atomic electron velocities and the upper limit is attained due to radiative effects, and both limits exhibit some Z dependence. Figure 1.11 depicts this region with muons on copper. Clearly, the region typically used for muon ionization cooling ($100 \text{ MeV}/c < p_\mu < 1000 \text{ MeV}/c$) falls in the middle of the Bethe region.

Derivation of T_{max}

core sources

*charge unit
cm³ = 100 m⁻²*

Although T_{max} is used symbolically in many equations, here it is derived explicitly from a relativistic point of view. This derivation yields Eq. (2.8) and works in natural units such that $c = 1$. Conservation of energy for a muon incident upon an electron at rest requires that

$$\begin{aligned} E_\mu + m_e &= E_{\mu,f} + E_e, & \text{or} \\ \sqrt{p_\mu^2 + m_\mu^2} + m_e &= \sqrt{p_{\mu,f}^2 + m_\mu^2} + T_e + m_e, & \text{or} \\ p_{\mu,f}^2 &= p_\mu^2 + T_e^2 - 2T_e \sqrt{p_\mu^2 + m_\mu^2}, & \cancel{\text{or}} \end{aligned} \quad (2.6)$$

with

$$\begin{aligned} E_e &= T_e + m_e = \sqrt{p_e^2 + m_e^2}, & \text{or} \\ p_e^2 &= (T_e + m_e)^2 - m_e^2, & \text{or} \end{aligned} \quad (2.7)$$

where T_e is the final kinetic energy of the electron, p_μ is the initial muon momentum, m_μ is the mass of the muon, and $p_{\mu,f}$ is the final muon momentum.

Conservation of momentum requires that

$$\begin{aligned} \vec{p}_\mu &= \vec{p}_{\mu,f} + \vec{p}_e, & \text{or} \\ p_{\mu,f}^2 &= p_\mu^2 + p_e^2 - 2p_\mu p_e \cos \alpha, \end{aligned}$$

where α is the angle between the initial muon momentum and the final electron momentum. Using Eq. (2.7) for p_e on the right-hand side this becomes

$$p_{\mu,f}^2 = p_\mu^2 + (T_e + m_e)^2 - m_e^2 - 2p_\mu \cos \theta \sqrt{(T_e + m_e)^2 - m_e^2}.$$

Now substitution of Eq. (2.6) for $p_{\mu,f}^2$ on the left-hand side yields

$$p_\mu^2 + T_e^2 - 2T_e \sqrt{p_\mu^2 + m_\mu^2} = p_\mu^2 + (T_e + m_e)^2 - m_e^2 - 2p_\mu \cos \theta \sqrt{(T_e + m_e)^2 - m_e^2}.$$

For maximum energy (i.e. to attain $T_e = T_{max}$), $\cos \theta = 1$, which is representative of a head-on collision. Then

$$\begin{aligned} T_{max}^2 - 2T_{max}\sqrt{p_\mu^2 + m_\mu^2} &= T_{max}^2 + 2T_{max}m_e - 2p_\mu\sqrt{T_{max}^2 + 2T_{max}m_e} \\ -2T_{max}(\sqrt{p_\mu^2 + m_\mu^2} + m_e) &= -2p_\mu\sqrt{T_{max}^2 + 2T_{max}m_e} \\ \sqrt{p_\mu^2 + m_\mu^2} + m_e &= p_\mu\sqrt{1 + \frac{2m_e}{T_{max}}}. \end{aligned}$$

Substituting the initial muon energy $E_\mu = \sqrt{p_\mu^2 + m_\mu^2} = \gamma m_\mu$ and the initial muon momentum $p_\mu^2 = E_\mu^2 - m_\mu^2 = m_\mu^2(\gamma^2 - 1) = m_\mu^2\gamma^2\beta^2$ results in

$$\begin{aligned} \gamma m_\mu + m_e &= m_\mu \gamma \beta \sqrt{1 + \frac{2m_e}{T_{max}}} \\ (\gamma m_\mu + m_e)^2 &= m_\mu^2 \gamma^2 \beta^2 \left(1 + \frac{2m_e}{T_{max}}\right). \end{aligned}$$

Finally, solving for the maximum transferrable energy from an incident muon to an electron at rest is

$$T_{max} = \frac{2m_e\beta^2\gamma^2}{1 + 2\gamma \frac{m_e}{m_\mu} + \left(\frac{m_e}{m_\mu}\right)^2}. \quad (2.8)$$

2.1.2 Landau Straggling Model

~~What have I obtained?~~ Inconsistent formatting

The second ICOOL straggling model selects an energy loss from a Landau distribution [21]. This derivation is particularly important since it is the same model that was implemented into COSY in this work. Landau begins the derivation by stipulating that this theory assumes fast particles ("so that the usual ionisation theory may be applied", here taken as particles whose energy is in the Bethe regime in Figure 1.11). Moreover, the thickness of the absorber should be small enough, so that the energy loss is small compared to the initial energy. Landau defines the weight function $w(E, u)$ as the probability per unit length of an energy loss u given the instantaneous total energy E . For the aforementioned constraints, the weight function may be written simply as $w(u)$ (since E is now a constant instead of a

variable). Another way of describing this constraint is that the total energy of the particle is roughly constant while traversing the medium.

Let $f(L, \epsilon)$ be the desired distribution function for the energy loss. This means that the particle loses an amount of energy between ϵ and $\epsilon + d\epsilon$ while traversing an absorber of length L . Then on one hand

$$\text{change in } f \text{ per unit length} = \frac{\partial f(L, \epsilon)}{\partial L}.$$

On the other hand, the change in f may also be expressed as the difference of two functions: one at a length L with possible energy losses between ϵ and $\epsilon + d\epsilon$ and another at length L and with possible energy losses between $\epsilon - u$ and $\epsilon + d\epsilon - u$, with u accounting for the infinitesimal change in length. Then

$$\text{change in } f \text{ per unit length} = \left[\int_0^\infty w(u)f(L, \epsilon - u)du \right] - f(L, \epsilon).$$

Often referred to as the integral transport equation, the two previous definitions of the change in f per unit length may be combined as

$$\frac{\partial f(L, \epsilon)}{\partial L} = \left[\int_0^\infty w(u)f(L, \epsilon - u)du \right] - f(L, \epsilon). \quad (2.9)$$

Since L and ϵ are independent and implicit variables, this allows for a Laplace transformation. Take the transformed function with respect to ϵ as

$$\phi(p, L) = \int_0^\infty e^{-pe} f(\epsilon) d\epsilon.$$

(Note that p is simply a dummy variable and not the momentum.) Then the inverse transformation gives

$$f(L, \epsilon) = \frac{1}{2\pi i} \int_{K-i\infty}^{K+i\infty} \phi(p, L) e^{pe} dp. \quad (2.10)$$

~~What's K?~~ ~~How known?~~
Observe here that $K > 0$ and so the integral is just to the right of the imaginary axis. This is the desired distribution function, and so is useful later. However, without the form of ϕ it is not useful. The goal then is to find a closed form of ϕ .

Multiplying both sides of Eq. (2.9) by e^{-pe} and integrating with respect to $d\epsilon$ yields

$$\int_0^\infty \frac{\partial f}{\partial L} e^{-pe} d\epsilon = \int_0^\infty \left[\int_0^\infty w(u) f(L, \epsilon - u) du \right] e^{-pe} d\epsilon - \int_0^\infty f(L, \epsilon) e^{-pe} d\epsilon.$$

On the left side, the operations of partial derivative and integration are commutable, and are therefore switched. On the right side, the first term has commutable integrations and so the order is switched. For the second term, note that $w(u)$ is normalized, so adding the integral of $w(u)$ over all u changes nothing. Dropping the implicit L for now,

$$\begin{aligned} \frac{\partial}{\partial L} \int_0^\infty e^{-pe} f(\epsilon) d\epsilon &= \int_0^\infty \left[\int_0^\infty e^{-pe} f(\epsilon - u) du \right] w(u) du - \\ &\quad \int_0^\infty \left[\int_0^\infty e^{-pe} f(\epsilon) du \right] w(u) du. \end{aligned}$$

Parts of the left side and the second term on the right side may be substituted for ϕ directly, while the first term on the right side should be shifted by $-u$, resulting in

$$\frac{\partial}{\partial L} \phi(p, L) = \int_0^\infty \left[\int_{-u}^\infty e^{-p(\epsilon+u)} f(\epsilon) d\epsilon \right] w(u) du - \int_0^\infty \phi(p, L) w(u) du.$$

Now recall that $f(\epsilon)$ is the desired function for energy loss. Therefore, $f(\epsilon < 0) = 0$ (i.e., the particle cannot gain energy while traversing a medium), and so

$$\begin{aligned} \frac{\partial}{\partial L} \phi(p, L) &= \int_0^\infty e^{-pu} \left[\int_0^\infty e^{-pe} f(\epsilon) d\epsilon \right] w(u) du - \phi(p, L) \int_0^\infty w(u) du \\ &= \phi(p, L) \int_0^\infty w(u) (e^{-pu} - 1) du. \end{aligned}$$

This differential equation is a first-order, undriven normal linear ODE (ordinary differential equation) [22]. Let prime ('') denote a partial derivative with respect to L . Then the strategy to solve this ODE is to define a function $h(L)$ as

$$h(L) = - \int_0^\infty w(u) (e^{-pu} - 1) du$$

and its antiderivative as

$$H(L) = \int h(L) dL = L \int_0^\infty w(u) (1 - e^{-pu}) du.$$

Then

$$\phi' + \phi \cdot h(L) = 0. \quad (2.11)$$

Since $(e^{H(L)})' = e^{H(L)} \cdot H'(L) = e^{H(L)} \cdot h(L)$, it is useful to multiply both sides of the ODE in Eq. (2.11) by $e^{H(L)}$, resulting in

$$\begin{aligned} \phi' \cdot e^{H(L)} + \phi \cdot h(L) \cdot e^{H(L)} &= 0, \\ (\phi \cdot e^{H(L)})' &= 0. \end{aligned}$$

Integrating both sides yields

$$\begin{aligned} \phi \cdot e^{H(L)} &= K_1, \\ \phi &= K_1 e^{-H(L)}, \\ \phi(p, L) &= K_1 \exp \left[-L \int_0^\infty w(u) (1 - e^{-pu}) du \right]. \end{aligned}$$

This differential equation is now solvable provided that there are initial conditions. The first observation is that for $L = 0$, the only possible energy loss is zero. Mathematically, this means that $f(0, \epsilon) = \delta(\epsilon)$; that is, the probability of energy loss is 100% for an energy loss of zero and 0% for all other energy losses. Then the boundary condition on ϕ is

$$\begin{aligned} \phi(p, 0) &= \int_0^\infty \delta(\epsilon) e^{-pe} d\epsilon \\ \phi(p, 0) &= e^{p \cdot 0} \\ \phi(p, 0) &= 1 = K_1 \exp[0]. \end{aligned}$$

Then

$$\phi(p, L) = \exp \left[-L \int_0^\infty w(u) (1 - e^{-pu}) du \right].$$

is

$$f(L, \epsilon) = \frac{1}{2\pi i} \int_{K-i\infty}^{K+i\infty} \exp \left[p\epsilon - L \int_0^\infty w(u)(1 - e^{-pu}) du \right] dp. \quad (2.12)$$

In principle, this is the general solution to the energy loss profile for a particle traversing some medium. In practice, the only thing which is inhibiting implementation is an algorithm to generate a number from this distribution (which is discussed in Chapter 3) and the function $w(u)$. Once $w(u)$ is obtained, the integral may be found using numeric integration, provided that it is not computationally expensive.

Livingston and Bethe [23] derived the form of $w(u)$ in 1937, and it is

$$w(u) = \frac{\xi}{L} \frac{1}{u^2},$$

where

$$\xi = \frac{2\pi r_e^2 m_e N_A Z \rho L}{\beta^2 A} \quad (2.13)$$

and r_e is the classical electron radius, m_e is the electron mass, N_A is Avagadro's number, Z is the nuclear charge, ρ is the density of the material, L is the length of the material, A is the nuclear mass, and $\beta = v/c$ is the relativistic speed. Now the form of $w(u)(1 - e^{-pu})$ may be seen in Figure 2.2. It can be seen that the most

important values of p are those where $pu \ll 1$ and $1 \ll pu$ since values of $pu \approx 1$ tends to vanish.

Rather than zero, let u_{min} be the minimum possible energy loss. Now consider a certain energy u_1 such that $u_{min} \ll u_1$ and $pu_1 \ll 1$. Then the integral in the exponent of Eq. (2.12) has the form

$$L \int_0^\infty w(u)(1 - e^{-pu}) du = \xi \left(\int_0^{u_1} \frac{1 - e^{-pu}}{u^2} du + \int_{u_1}^\infty \frac{1 - e^{-pu}}{u^2} du \right).$$

Since the first integral is over the small values, it is possible to write $1 - e^{-pu} \approx 1 - (1 - pu) = pu$. Furthermore, the minimum energy loss is not 0 but rather u_{min} .

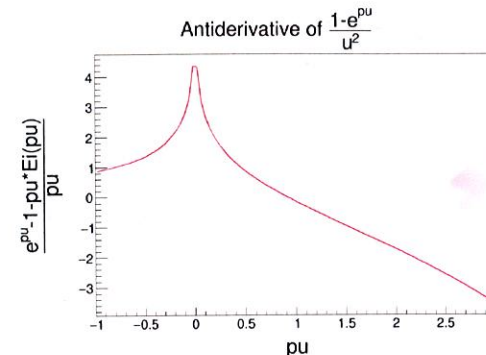


Figure 2.2: Plot of $\int w(u)(1 - e^{-pu}) du$ for various pu . On the vertical axis is the antiderivative of $w(u)(1 - e^{-pu})$, with $Ei(x)$ representing the exponential integral.

Then

$$\begin{aligned} \frac{L}{\xi} \int_0^\infty w(u)(1 - e^{-pu}) du &= \int_{u_{min}}^{u_1} \frac{p u}{u^2} du + \int_{u_1}^\infty \frac{1 - e^{-pu}}{u^2} du \\ &= p \int_{u_{min}}^{u_1} \frac{1}{u} du + \int_{u_1}^\infty \frac{1 - e^{-pu}}{u^2} du \\ &= p \ln \frac{u_1}{u_{min}} + \int_{u_1}^\infty \frac{1 - e^{-pu}}{u^2} du. \end{aligned}$$

For the second term, integration by parts and evaluation at the boundaries gives

$$\frac{L}{\xi} \int_0^\infty w(u)(1 - e^{-pu}) du = p \ln \frac{u_1}{u_{min}} + \frac{1 - e^{-pu_1}}{u_1} + p \int_{u_1}^\infty \frac{e^{-pu}}{u} du.$$

Recalling that u_1 was chosen such that $pu_1 \ll 1$, the exponential in the second term may be approximated as $e^{-pu_1} \approx 1 - pu_1$. Then

$$\frac{L}{\xi} \int_0^\infty w(u)(1 - e^{-pu}) du = p \ln \frac{u_1}{u_{min}} + p + p \int_{u_1}^\infty \frac{e^{-pu}}{u} du. \quad (2.14)$$

Too much on others' work? Too much math?
not enough physics?

The final integral may be evaluated first by letting $K_2 = pu$:

$$\begin{aligned} \frac{L}{\xi} \int_{u_1}^{\infty} \frac{e^{-pu}}{u} du &= \int_{pu_1}^{\infty} \frac{e^{-K_2}}{K_2} dK_2 \\ &= \int_{pu_1}^{\infty} \frac{e^{-K_2}}{K_2} dK_2 + \int_{pu_1}^1 \frac{dK_2}{K_2} - \int_{pu_1}^1 \frac{dK_2}{K_2} \\ &= \int_{pu_1}^1 \frac{e^{-K_2}}{K_2} dK_2 + \int_1^{\infty} \frac{e^{-K_2}}{K_2} dK_2 + \int_{pu_1}^1 \frac{dK_2}{K_2} - \int_{pu_1}^1 \frac{dK_2}{K_2} \\ &= \int_{pu_1}^1 \left(\frac{e^{-K_2}}{K_2} - \frac{1}{K_2} \right) dK_2 + \int_1^{\infty} \frac{e^{-K_2}}{K_2} dK_2 + \int_{pu_1}^1 \frac{dK_2}{K_2} \\ &= \int_{pu_1}^1 \frac{dK_2}{K_2} + \left[\int_{pu_1}^1 \frac{e^{-K_2} - 1}{K_2} dK_2 + \int_1^{\infty} \frac{e^{-K_2}}{K_2} dK_2 \right]. \end{aligned}$$

The first term is easily evaluated, and the second term in brackets is approximately² the negative of Euler's constant, $-C_{Euler}$. Putting this back into Eq. (2.14) yields

$$\begin{aligned} \frac{L}{\xi} \int_0^{\infty} w(u)(1 - e^{-pu}) du &= p \ln \frac{u_1}{u_{min}} + p(1 - C_{Euler} - \ln pu_1) \\ &= p(1 - C_{Euler} - \ln pu_{min}). \end{aligned}$$

Now Eq. (2.12) may be rewritten as

$$\begin{aligned} f(L, \epsilon) &= \frac{1}{2\pi i} \int_{K-i\infty}^{K+i\infty} \exp \left[p\epsilon - L \int_0^{\infty} w(u)(1 - e^{-pu}) du \right] dp \\ &= \frac{1}{2\pi i} \int_{K-i\infty}^{K+i\infty} \exp \left[p\epsilon - p\xi(1 - C_{Euler} - \ln pu_{min}) \right] dp. \end{aligned}$$

If a unitless variable of integration is desired, then $p \rightarrow p/\xi$, and

$$f(\xi, \epsilon) = \frac{1}{2\pi i \xi} \int_{K-i\infty}^{K+i\infty} \exp \left[p\frac{\epsilon}{\xi} - p(1 - C_{Euler} - \ln \frac{u_{min}}{\xi}) + p \ln p \right] dp,$$

or simply

$$f(\lambda) = \frac{1}{2\pi i \xi} \int_{K-i\infty}^{K+i\infty} \exp \left[p \ln p + \lambda p \right] dp, \quad (2.15)$$

where evidently

$$\lambda = \frac{\epsilon}{\xi} - 1 + C_{Euler} + \ln \frac{\xi}{u_{min}}.$$

²This expression would be exactly $-C_{Euler}$ if $pu_1 = 0$.

However, typically the Landau function is evaluated for the desired *fluctuation about the mean energy loss*, not the energy loss itself. Because of this, λ must be shifted by the mean, $\langle \epsilon \rangle$. Furthermore, a relativistic correction of $-\beta^2$ is added and $u_{min} \rightarrow T_{max}$ (from Eq. (2.8)), resulting in the final form of the Landau parameter:

$$\lambda \equiv \frac{\epsilon - \langle \epsilon \rangle}{\xi} - (1 - C_{Euler}) - \beta^2 - \ln(\xi/T_{max}). \quad (2.16)$$

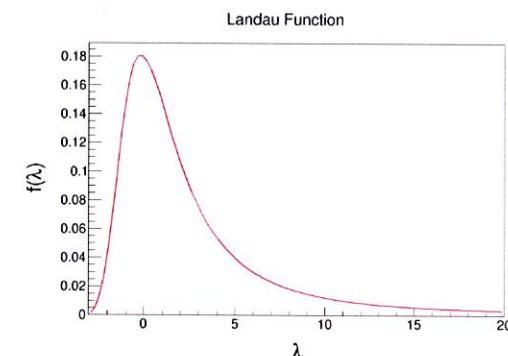


Figure 2.3: Example of the Landau function.

In summary, the ICOOL Landau model uses the mean energy loss from the Bethe-Bloch equation (Eq. (2.5)). The routine then adds noise based on the Landau function (see, e.g., Figure 2.3), which has a mode of zero. This value is then accepted as the total energy loss of the particle.

2.1.3 Vavilov Straggling Model

The Vavilov model [24] is similar to the Landau model, except that the thickness of the absorber is not required to be small enough such that the energy loss is small compared to the initial energy. The derivation is also similar, except that Vavilov introduced a limit on the maximum transferable energy due to a single collision

(recall that in Landau theory the upper limit was ∞). The result is

$$f(\lambda_v, \kappa, \beta^2) = \frac{1}{\xi} \phi_v(\lambda_v, \kappa, \beta^2), \quad (2.17)$$

where

$$\begin{aligned} \phi_v(\lambda_v, \kappa, \beta^2) &= \frac{1}{2\pi i} \int_{K+i\infty}^{K-i\infty} \phi(p, \kappa, \beta^2) e^{\lambda p}, \\ \phi(p, \kappa, \beta^2) &= \exp[\kappa(1 + \beta^2 \gamma)] \exp[\psi(p, \kappa, \beta^2)], \\ \psi(p) &= p \ln \kappa + (p + \beta^2 \kappa)[\ln(p/\kappa) + E_1(p/\kappa)] - \kappa e^{-p/\kappa}, \\ E_1(p) &= \int_{\infty}^z \frac{e^{-u}}{u} du \quad (\text{the exponential integral}), \\ \lambda_v &= \kappa \left(\frac{\epsilon - \langle \epsilon \rangle}{\xi} - (1 - C_{Euler}) - \beta^2 \right) = \kappa(\lambda + \ln \kappa), \text{ and} \\ \kappa &= \xi/T_{max}. \end{aligned}$$

While this function in theory is universal for the needs of this study, clearly such a distribution function requires numeric methods, and as such is more costly than the Landau method. Fortunately, the Vavilov distribution converges to either the Landau distribution (for $\kappa \rightarrow 0$) or a Gaussian distribution (for $\kappa \rightarrow \infty$) at its extrema. The cutoffs for these extrema in practice are

$$\phi_v = \begin{cases} \text{Landau via Eq. (2.15)} & \kappa \leq 0.01 \\ \text{Vavilov via Eq. (2.17)} & 0.01 < \kappa < 10 \\ \text{Gaussian via } Gaus(\langle \epsilon \rangle, \sigma) \text{ in Eqns. 2.5 and 2.1} & 10 \leq \kappa \end{cases}$$

2.2 Multiple Scattering in ICOOL

ICOOL version 3.30 [17] boasts a total of seven models of multiple scattering:

1. Gaussian (σ determined by Rossi-Greisen model),

2. Gaussian (σ determined by Highland model),

3. Gaussian (σ determined by Lynch-Dahl model),
4. Bethe version of Molière distribution with Rutherford limit,
5. Rutherford,
6. Fano with Rutherford limit, and
7. Tollestrup with Rutherford limit.

The scattering model used in this work is Fano with Rutherford limit, which is also the default scattering model in ICOOL. The following is a derivation of the Rutherford model accompanied by a brief discussion of the Fano model. Unless otherwise stated, the derivation of the Rutherford model closely follows [8].

The Rutherford model is used in part in four out of the seven models because it is so robust. The derivation can be done using the Coulomb potential, classical mechanics, the Born approximation, and quantum field theory, with the quantum mechanics Born approximation being the weapon of choice here. Recall that the quantum model used in this work is represented by Figure 2.4. Here there is an incoming plane wave (mathematically represented by e^{ikz}) and a spherical wave (represented by e^{ikr}/r). r and z are coordinates, i is the imaginary unit, and k is the wave number, classically related to the energy as $k = \sqrt{2mE}/\hbar$. Then basic quantum mechanics suggests that the solution to the Schrödinger equation has the form

$$\psi(r, \theta) \approx A \left(e^{ikz} + f(\theta) \frac{e^{ikr}}{r} \right), \quad (2.18)$$

where A is the total amplitude and $f(\theta)$ is the scattering amplitude. The probability of the particle scattering in a particular direction is given by the amplitude squared,

\rightarrow non-relativistic!

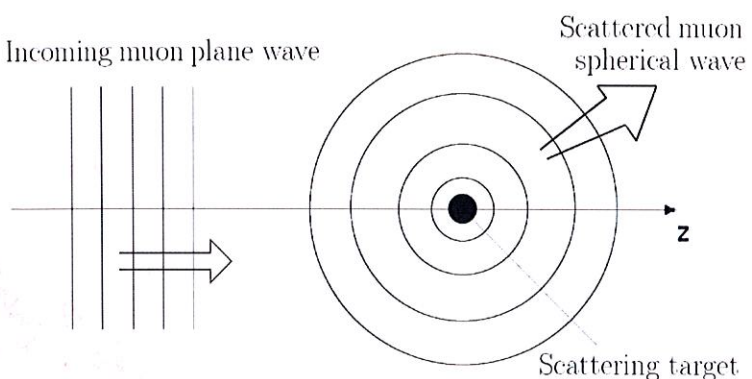


Figure 2.4: Quantum scattering model. (repeated from Fig 1.6)

$|f(\theta)|^2$, and is the object of this derivation. Now, ψ solves the differential (time-independent) Schrödinger equation, which usually has the form

$$-\frac{\hbar^2}{2m}\nabla^2\psi + V\psi = E\psi,$$

where V is the system potential and E is the energy of the wavefunction. This can be expressed alternatively by assigning $Q \equiv V\psi \cdot 2m/\hbar^2$ and recalling that $k = \sqrt{2mE}/\hbar$. Then

$$(\nabla^2 + k^2)\psi = Q. \quad (2.19)$$

The strategy is to solve Eq. (2.19) for ψ . A comparison of the solutions for ψ from Eqns. 2.18 and 2.19 yields the scattering amplitude $f(\theta)$. However, if Eq. (2.19) is solved for ψ then it suggests that ψ will be in integral form since Eq. (2.19) is a differential equation. Therefore, some special techniques are required. Note that it does not matter at this point that Q is a function of ψ , since the task is to compare the integrated solution of Eq. (2.19) with that of Eq. (2.18). Moving forward, observe

that Eq. (2.19) may again be rewritten as

$$(\nabla^2 + k^2)\psi(\vec{r}) = Q(\vec{r}) = \int \delta^3(\vec{r} - \vec{r}_0)Q(\vec{r}_0)d^3\vec{r}_0. \quad (2.20)$$

Now it is natural to guess that there exists some function $G(\vec{r})$ such that

$$\psi(\vec{r}) = \int G(\vec{r} - \vec{r}_0)Q(\vec{r}_0)d^3\vec{r}_0, \quad (2.21)$$

in which case

$$(\nabla^2 + k^2)\psi(\vec{r}) = (\nabla^2 + k^2) \int G(\vec{r} - \vec{r}_0)Q(\vec{r}_0)d^3\vec{r}_0,$$

or

$$(\nabla^2 + k^2)\psi(\vec{r}) = \int [(\nabla^2 + k^2)G(\vec{r} - \vec{r}_0)]Q(\vec{r}_0)d^3\vec{r}_0. \quad (2.22)$$

Combining Eqns. 2.20 and 2.22, it can be seen that

$$\int \delta^3(\vec{r} - \vec{r}_0)Q(\vec{r}_0)d^3\vec{r}_0 = \int [(\nabla^2 + k^2)G(\vec{r} - \vec{r}_0)]Q(\vec{r}_0)d^3\vec{r}_0.$$

Consequently, one comes to the conclusion that

$$(\nabla^2 + k^2)G(\vec{r}) = \delta^3(\vec{r}). \quad (2.23)$$

If Eq. (2.23) seems familiar, it is because this is the Helmholtz equation with a delta function source. $G(\vec{r})$ is Green's function for the Helmholtz equation, and in this case it is the response to the delta function source. Now, if one accepts that there exists a well-known particular solution for Eq. (2.23), then one could skip forward to the solution in Eq. (2.26); however, it is also derived subsequently.

The usual strategy in solving systems like Eq. (2.23) is to Fourier transform both the Green's function and the delta function. Then creating the dummy variable \vec{s} , the transform yields

$$G(\vec{r}) = \frac{1}{(2\pi)^{\frac{3}{2}}} \int e^{i\vec{s} \cdot \vec{r}} g(\vec{s}) d^3\vec{s},$$

and

$$\delta^3(\vec{r}) = \frac{1}{(2\pi)^3} \int e^{i\vec{s}\cdot\vec{r}} d^3\vec{s}.$$

Then from Eq. (2.23),

$$\frac{1}{(2\pi)^{\frac{3}{2}}} \int (k^2 e^{i\vec{s}\cdot\vec{r}} - s^2 e^{i\vec{s}\cdot\vec{r}}) g(\vec{s}) d^3\vec{s} = \frac{1}{(2\pi)^3} \int e^{i\vec{s}\cdot\vec{r}} d^3\vec{s},$$

it is clear that $g(\vec{s}) = 1/(2\pi)^{3/2}(k^2 - s^2)$. Now all that is left is to find $G(\vec{r})$ from its transformation:

$$G(\vec{r}) = \frac{1}{(2\pi)^3} \int e^{i\vec{s}\cdot\vec{r}} \frac{d^3\vec{s}}{k^2 - s^2}$$

$$G(\vec{r}) = \frac{1}{(2\pi)^3} \int_0^\infty \frac{s}{k^2 - s^2} \left(\int_0^\pi e^{isr \cos\theta} \sin\theta d\theta \right) ds \int_0^{2\pi} d\phi.$$

The integration over ϕ is trivial, and the integration over θ can be done via u substitution, with $u = \cos\theta$. The last integral is over s , and is

$$G(\vec{r}) = \frac{1}{2\pi^2 r} \int_0^\infty \frac{s \sin sr}{k^2 - s^2} ds = \frac{1}{4\pi^2 r} \int_{-\infty}^\infty \frac{s \sin sr}{k^2 - s^2} ds.$$

This integral is not simple to solve, but it does have two poles at $s = k$ and $s = -k$, which implies the technique of choice should be to use Cauchy's integral formula for simple poles³:

$$\oint \frac{f(z)}{z - z_0} dz = 2\pi i f(z_0), \quad (2.24)$$

where the integral is done over some path in the complex plane and z_0 is the pole of interest which lies in the ~~enclosed~~ path (note: the integral is zero if there exist no poles in the ~~enclosed~~ path). It follows then that $f(z)$ is not simply any function, but a necessarily complex function ~~which is closed~~. For this reason, the (strictly real) Green's function integral should be split up into two (strictly complex) functions, as depicted by Figure 2.5. This can be done by expanding the $\sin sr$ term and factoring $k^2 - s^2$:

$$G(\vec{r}) = \frac{i}{8\pi^2 r} \left[\int_{-\infty}^\infty \frac{se^{isr}}{(s-k)(s+k)} ds - \int_{-\infty}^\infty \frac{se^{-isr}}{(s-k)(s+k)} ds \right]. \quad (2.25)$$

³This touches an area of mathematics known as the calculus of residues, and is based on the Laurent series.

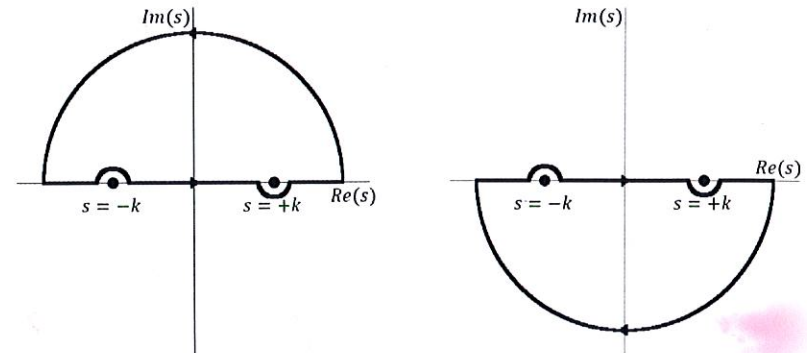


Figure 2.5: Two parts of Green's function with their poles at $s = \pm k$, altered to be closed by a semicircle at $|s| = \pm \infty$.

Observe that in Eq. (2.25) the path integrals at $|s| = \pm \infty$ have been left out. This is because they do not contribute to the integral since the first integrand corresponds to the left side of Figure 2.5 and goes like e^{isr} , hence going to zero at large positive imaginary numbers. Similarly, the second integrand goes like e^{-isr} and goes to zero at large negative imaginary numbers.

Combining Eqns. 2.24 and 2.25, it can be seen that

$$G(\vec{r}) = \frac{i}{8\pi^2 r} [(i\pi e^{ikr}) - (-i\pi e^{ikr})] = -\frac{e^{ikr}}{4\pi r}.$$

This is a particular solution to the inhomogeneous Helmholtz equation. To get a general solution, the solution to the homogeneous Helmholtz equation must be added:

$$G(\vec{r}) = G_0(\vec{r}) - \frac{e^{ikr}}{4\pi r}; \quad (2.26)$$

that is, $G_0(\vec{r})$ solves $(\nabla^2 + k^2)G_0(\vec{r}) = 0$.

cite reference?

Using Eq. (2.21) in conjunction with Eq. (2.26) gives rise to the *integrated* time-independent Schrödinger equation:

$$\psi(\vec{r}) = \psi_0(\vec{r}) - \frac{m}{2\pi\hbar^2} \int \frac{e^{ik|\vec{r}-\vec{r}_0|}}{|\vec{r}-\vec{r}_0|} V(\vec{r}_0) \psi(\vec{r}_0) d^3\vec{r}_0. \quad (2.27)$$

That is, nothing has been said about the potential and so this equation is quite general. Eq. (2.27) gives the recursive form for ψ . Let $g = -me^{ik|\vec{r}-\vec{r}_0|}/2\pi\hbar^2|\vec{r}-\vec{r}_0|$.

Then Eq. (2.27) says that

$$\psi = \psi_0 + \int gV\psi = \psi_0 + \int gV(\psi_0 + \int gV\psi) \quad ?$$

Applying this recursion several times gives the Born series:

$$\psi = \psi_0 + \int gV\psi_0 + \int \int gVgV\psi_0 + \int \int \int gVgVgV\psi_0 + \dots$$

The zeroth term is exact if there is no scattering whatsoever (i.e., $V = 0$) and the first term is accurate if the scattering potential is “weak” (that is, if V is small enough for the second term to be neglected). For the purposes of this derivation, first order is a sufficient approximation for ψ . Then

$$\psi = \psi_0 + \frac{m}{2\pi\hbar^2} \int \frac{e^{ik|\vec{r}-\vec{r}_0|}}{|\vec{r}-\vec{r}_0|} V(\vec{r}_0) \psi_0(\vec{r}_0) d^3\vec{r}_0.$$

Recall that the strategy was to compare this solution of the Helmholtz equation with the wavefunction from the quantum scattering model (Eq. (2.18)) in order to find the scattering amplitude, $f(\theta)$. Doing so yields

$$f(\theta) = -\frac{r}{e^{ikr}} \frac{m}{2\pi\hbar^2 A} \int \frac{e^{ik|\vec{r}-\vec{r}_0|}}{|\vec{r}-\vec{r}_0|} V(\vec{r}_0) \psi_0(\vec{r}_0) d^3\vec{r}_0.$$

The Coulomb potential goes as $1/r^2$, and as such $V(\vec{r}_0)$ is localized about $\vec{r}_0 = 0$. Since particles are observed far away from their scattering centers, it is advantageous to make use of the fact that $r \gg r_0$. However, caution must be taken,

? better to compare lengths?

since one must evaluate the exponential and non-exponential terms separately, for they are of separate orders. For the non-exponential terms, this is simple, since

$$\frac{r}{|\vec{r}-\vec{r}_0|} \approx 1.$$

The exponential terms look like

$$e^{ik(|\vec{r}-\vec{r}_0|-r)},$$

and so it is useful to expand the absolute value as

$$|\vec{r}-\vec{r}_0|^2 = r^2 + r_0^2 - 2\vec{r} \cdot \vec{r}_0 \approx r^2 \left(1 - 2\frac{\vec{r} \cdot \vec{r}_0}{r^2}\right),$$

or simply

$$|\vec{r}-\vec{r}_0| \approx r - \hat{r} \cdot \vec{r}_0.$$

This leaves

$$f(\theta) = \frac{m}{2\pi\hbar^2} \int e^{-ik\hat{r} \cdot \vec{r}_0} V(\vec{r}_0) e^{ik\hat{z} \cdot \vec{r}_0} d^3\vec{r}_0, \quad (2.28)$$

Now define $\vec{\kappa} \equiv k(\hat{z} - \hat{r})$ such that $\kappa = 2k \sin \theta/2$. The exponential term becomes

$$e^{i\vec{\kappa} \cdot \vec{r}_0} = e^{i\kappa r_0 \cos \theta_0}.$$

Furthermore, the form of the potential V is known. Since the scattering for the low- Z target happens at low temperatures, it is possible to use the Fermi-Thomas approximation for screening [25]. This modifies the Maxwell equation

$$\nabla^2 V(r) = -\frac{\rho}{\epsilon_0}$$

to

$$(\nabla^2 - b^2) V(r) = -\frac{Q}{\epsilon_0} \delta(r),$$

where ρ is the charge density, b is some screening constant, ϵ_0 is the permittivity of free space, and Q is the charge of the potential (in this case, the atomic number Z).

The solution is

$$V(r) = \frac{Q}{4\pi\epsilon_0} \frac{e^{-br}}{r}.$$



Then the quantum scattering equation (Eq. (2.28)) becomes

$$f(\theta) \propto \int e^{ikr_0 \cos(\theta_0)} e^{-bro} r_0 \sin(\theta_0) dr_0 d\theta_0 d\phi_0,$$

where the amplitude terms have been left out since $|f(\theta)|^2$ is normalized anyway. Here it is seen that there does exist some θ dependence in $f(\theta)$ (by virtue of κ). The integral over ϕ_0 is trivial, and the integral over θ_0 can be done via u substitution, with $u = \cos \theta_0$. This leaves

$$f(\theta) \propto \frac{1}{\kappa} \int_0^\infty e^{-bro} \sin(kr_0) dr_0,$$

which has the solution

$$f(\theta) \propto \frac{1}{b^2 + \kappa^2}.$$

For classical Rutherford scattering, $b \rightarrow 0$. Recalling that $\kappa = 2k \sin \theta / 2$ yields the final Rutherford scattering distribution:

$$\begin{aligned} |f(\theta)|^2 &\propto \frac{1}{\sin^4 \frac{\theta}{2}} = \frac{1}{(\sin^2 \frac{\theta}{2})^2} = \frac{1}{\left(\frac{1}{2} [1 - \cos^2(2 \cdot \frac{\theta}{2})]\right)^2}, \\ |f(\theta)|^2 &\propto \frac{1}{(1 - \cos^2 \theta)^2}. \end{aligned} \quad (2.29)$$

Only the tail of Eq. (2.29) should be used since it blows up at $\theta = 0$. This may seem like a contradiction since the Born series was truncated at the weak potential term (the first nontrivial term), and hence the incoming muons should not scatter much at all! In fact, the muons are not scattering much at all for each individual atom they encounter. Over the entire absorber, however, some muons have a net scattering angle which is small (and therefore should not be approximated by the Rutherford tail) whereas others have a large net scattering angle (and are well represented by Eq. (2.29)). Many weak potentials can still induce a relatively large scattering angle.

2.3 Energy Straggling in G4Beamline

G4Beamline uses the in-house straggling model described by GEANT4 in [19]. GEANT4 has determined that a “thick absorber” occurs when the following conditions

are met:

$$|\Delta E| > \kappa T_c \quad \text{and} \quad T_{max} \leq 2T_c, \quad (2.30)$$

where ΔE is the energy loss, κ is the Vavilov limit parameter, T is the kinetic energy cut of δ -electrons, and T_{max} is the maximum transferrable kinetic energy between the incoming particle and target electron. These symbols can also be found in the Definition of Terms at the beginning of this document.

For thick absorbers, the energy loss is sampled according to a simple Gaussian distribution with average equal to the Bethe-Bloch energy loss (Eq. (2.5)) and a standard deviation according to Bohr's variance (Eq. (2.1)).

If these conditions are not met, a “thin absorber” algorithm is called. Here, atoms are assumed to have only two energy levels with binding energies E_1 and E_2 . The interacting muon can then lose energy via excitation, yielding an energy loss of E_1 or E_2 , or lose energy via δ ray production, yielding an energy loss according to $g(E) \propto 1/E^2$, or (more likely) some combination or weighted average of the two. $g(E)$ may then be normalized:

$$\int_{E_0}^{T_{up}} g(E) dE = 1 \rightarrow g(E) = \frac{E_0 T_{up}}{T_{up} - E_0} \frac{1}{E^2}, \quad (2.31)$$

where E_0 is the ionization energy of the atom in question and T_{up} is some kinetic energy cutoff (either the production threshold for delta rays or the maximum transferrable energy, whichever is smaller).

The probability for obtaining any one of these energy losses is given by the macroscopic cross section, Σ_i , where $i = 1, 2, 3$. For excitation ($i = 1, 2$), the cross section has a form similar to the deterministic Bethe-Bloch equation (Eq. (2.5)):

$$\Sigma_i = C \frac{f_i}{E_i} \frac{\ln(2m_e c^2 (\beta\gamma)^2 / E_i)}{\ln(2m_e c^2 (\beta\gamma)^2 / I)} (1 - r). \quad (2.32)$$

Not (not
a person)

Here, C and $r = 0.55$ are model parameters with r describing the relative contribution of excitation to ionization, f_i are the relative oscillator strengths of the energy levels of E_i , I is the average ionization energy, and the other symbols have their usual meaning. For continuous energy loss, the cross section is given by

$$\Sigma_3 = C \frac{T_{up} - E_0}{T_{up} E_0 \ln(T_{up}/E_0)} r. \quad (2.33)$$

The oscillator strengths are relative to one another and hence should satisfy

$$f_1 + f_2 = 1. \quad (2.34)$$

The next constraint comes from [26] and states that all the energy levels should be weighted and added logarithmically to the total ionization energy:

$$f_1 \ln E_1 + f_2 \ln E_2 = \ln I. \quad (2.35)$$

Moreover, f_1 and f_2 can be thought of as representing the relative number of loosely and tightly bound electrons. Using the first constraint, it is easy to see that the absolute number of loosely bound electrons is $Z \cdot f_1$ and the absolute number of tightly bound electrons is $Z \cdot f_2$ (since $Z \cdot f_1 + Z \cdot f_2 = Z$). For modeling purposes, GEANT4 has placed empirical initial conditions on these parameters:

$$f_2 = 0 \quad \text{for } Z = 1, \quad (2.36)$$

$$f_2 = 2/Z \quad \text{for } Z \geq 2, \quad (2.37)$$

$$E_2 = 10 \text{ eV} \cdot Z^2, \quad (2.38)$$

$$E_0 = 10 \text{ eV}. \quad (2.39)$$

From these, f_1 and E_1 can be found from Eqns. 2.34 and 2.35 given a particular muon through a particular material (from which Z , I , β , and the like are taken).

Finally, an energy loss for a thin absorber can be sampled. For the contribution due to excitation, two numbers n_1 and n_2 are sampled randomly from a Poisson

distribution. These numbers represent the relative contributions of the energy levels of E_1 and E_2 , respectively:

$$\epsilon_{exc} = n_1 E_1 + n_2 E_2.$$

The contribution due to ionization can be found by inverting the cumulative distribution function of $g(E)$ (see Eq. (2.31)):

$$G(E) = \int_{E_0}^E g(E)dE \rightarrow E = \frac{E_0}{1 - u \frac{T_{up} - E_0}{T_{up}}},$$

where u is uniformly randomly selected from $[0, 1]$. However, this treatment so far has only been executed for a single ionization. For an absorber of length L , the number of ionizations n_3 is again sampled from a Poisson distribution. Then the total energy loss for thin absorbers is

$$\epsilon = n_1 E_1 + n_2 E_2 + \sum_{j=1}^{n_3} \frac{E_0}{1 - u_j \frac{T_{up} - E_0}{T_{up}}}. \quad (2.40)$$

It should be noted that [19] does make a brief mention of a width correction algorithm. This algorithm allegedly decreases the dependence of the results on kinetic energy cuts and step sizes and works for any thickness of material. However, the section in the manual is less than a page long and purely conceptual without any mathematics or data on which to elaborate. The width correction algorithm is relevant to this work in order to make a fair comparison and understand why this work and G4Beamline disagree in some places.

Finally, the GEANT4 straggling routine can be summarized as such:

1. Determine if the absorber is “thick” via Eq. (2.30).
2. If the absorber is thick, use Gaussian distribution with mean $\mu = \langle dE/dx \rangle$ (from Eq. (2.5)) and standard deviation from Eq. (2.1).
3. If the absorber is “thin”, use Eq. (2.40).

- Select n_1 , n_2 , and n_3 from a Poisson distribution.
 - Select u_j from a uniform distribution on $[0, 1]$ (where $j = 1 \dots n_3$).
 - Find E_2 , f_2 , and E_0 from Eq. (2.36).
 - Find E_1 from Eqns. 2.34 and 2.35.
4. Apply width correction algorithm.

2.4 Multiple Scattering in G4Beamline

The G4Beamline scattering model in [18] uses the GEANT4 Urbán model [19] and parameterizes according to experimental data and Lewis theory [27]. For this section, the scattering distribution is $g(u)$, where $u = \cos \theta$ and θ is the scattering angle.

Based on the models available, it can be inferred that the function responsible for the sampling of the angular distribution, $g(u)$, is based off both the Goudsmit-Saunderson treatment of scattering [28] and Rutherford scattering. One fundamental result from Goudsmit and Saunderson is that for small angles, the scattering distribution is Gaussian. Recall that Rutherford scattering was derived in Section 2.2 and resulted in Eq. (2.29). It should be noted that the shape of $g(u)$ was chosen empirically, and is

$$g(u) = q_g [p_g g_1(u) + (1 - p_g) g_2(u)] + (1 - q_g) g_3(u), \quad (2.41)$$

where $0 \leq p_g, q_g \leq 1$ and

$$\begin{aligned} g_1(u) &= C_1 e^{-a(1-u)} & -1 \leq u_0 \leq u \leq 1 \\ g_2(u) &= C_2 \frac{1}{(b_r - u)^{d_r}} & -1 \leq u \leq u_0 \leq 1 \\ g_3(u) &= C_3 & -1 \leq u \leq 1 \end{aligned}$$

are normalized over $[-1, 1]$, where C_i are normalization constants and a , b_r , d_r , and u_0 are empirical parameters. All of these parameters are discussed in this section, and can be found in Table 2.1.

Observe that for small angles, $g(u)$ is nearly Gaussian since $\exp(1-u) = \exp(1-\cos\theta) \approx \exp(\theta^2/2)$. For large angles, $g(u)$ resembles the Rutherford dependence of Eq. (2.29) for $b_r \approx 1$ and d_r close to 2. Moreover, at small q_g the shape of $g(u)$ is nearly constant since the constant function $g_3(u)$ dominates.

While Eq. (2.41) is the main point of this section, it would be incomplete without detailing the nine parameters mentioned. The C_i (with $i = 1, 2, 3$) are normalization constants. a , u_0 , and d_r are chosen based off theoretical and experimental data and are a bit more interesting. Finally, p_g , q_g , and b_r can be found using constraints.

Finding a

Observe from Eq. (2.41) that a only appears in $g_1(u)$. Further observe from Eq. (2.41) that $g_1(u)$ is only valid for u close to 1. Since $u = \cos\theta$ (where θ is the scattering angle), $g_1(u)$ must be the part of $g(u)$ that determines small angle scattering.

It has already been noted that $g_1(u)$ is approximately Gaussian for u close to 1. Highland [29] provided an estimate for the width of the (approximate) Gaussian scattering distribution. Let the width of this Gaussian distribution be θ_0 . Lynch and Dahl [30] gave corrections to Highland's form of θ_0 in 1991. If θ_0 truly is the width of the Gaussian scattering distribution, then it follows that

$$g_1(u) \underset{\approx}{\sim} \exp\left(-\frac{\theta^2}{2\theta_0^2}\right) \approx \exp\left(\frac{1}{2} \cdot \frac{1 - \cos\theta}{1 - \cos\theta_0}\right),$$

G4Beamline Scattering Distribution Parameters

Parameter	Physical Meaning	Found Via	Eqn.
C_1, C_2 , and C_3	Normalization constants	Normalization	N/A
a	Related to Gaussian-like σ	Relating the Gaussian-like behavior of $g_1(u)$ to Highland-like theory [29]	2.42
u_0	The boundary between the Gaussian-like $g_1(u)$ and the Rutherford-like $g_2(u)$	empirical parameterization	2.44
d_r	The Rutherford-like exponent in $g_2(u)$	empirical parameterization	2.45
p_g	Relative contribution of the Gaussian-like $g_1(u)$ to the Rutherford-like $g_2(u)$	Demanding continuity	2.48
b_r	Relative u offset of the Rutherford-like $g_2(u)$	Demanding smoothness	2.49
q_g	The relative contribution of the varying functions $g_1(u)$ and $g_2(u)$ to the constant function $g_3(u)$	Demanding that g gives the same mean value as Lewis theory	2.50

Table 2.1: The nine parameters of the scattering distribution used by G4Beamline (see Eq. (2.41)).

where \propto means “approximately proportional to”. Recall from Eq. (2.41) that

$$g_1(u) \propto \exp(-a(1-u)).$$

Then it is reasonable to choose a as

$$a = \frac{0.5}{1 - \cos \theta_0}, \quad (2.42)$$

so that

$$\exp(-a(1-u)) = \exp\left(\frac{1}{2} \cdot \frac{1 - \cos \theta}{1 - \cos \theta_0}\right).$$

For heavy charged particles (such as muons), the model for θ_0 has been modified even more from Lynch and Dahl by GEANT4 [19]. Its form is now chosen by GEANT4 [19] as

$$\theta_0 = \frac{13.6 \text{ MeV}}{\beta c p} z_{ch} \sqrt{\frac{t}{X_0} \left[1 + 0.105 \ln\left(\frac{t}{X_0}\right) + 0.0035 \left(\ln\left(\frac{t}{X_0}\right) \right)^2 \right]} \left(1 - \frac{0.24}{Z(Z+1)} \right). \quad (2.43)$$

Finding u_0

Observe from Eq. (2.41) that the parameter u_0 is the boundary between the Gaussian-like $g_1(u)$ and the Rutherford-like $g_2(u)$. GEANT4 [19] has chosen u_0 as

$$u_0 = 1 - \frac{3}{a}. \quad (2.44)$$

It is assumed that this parameter has been chosen as such based on empirical results, but no formal explanation is given. While GEANT4 [19] does not elaborate on this parameterization, validation in Section 5.2 shows that this choice is reasonable.

Finding d_r

Observe from Eq. (2.41) that the parameter d_r is the Rutherford-like exponent. Note that a classical Rutherford distribution would have $d_r = 2$. For heavy particles

such as muons, the parameter d_r has been chosen by GEANT4 [19] as

$$d_r = 2.40 - 0.027 Z^{\frac{2}{3}}. \quad (2.45)$$

It is assumed that this parameter has been chosen as such based on empirical results, but no formal explanation is given. While GEANT4 [19] does not elaborate on this parameterization, validation in Section 5.2 shows that this choice is reasonable.

Finding p_g

Now p_g is found using constraints on the scattering distribution $g(u)$. Observe from Eq. (2.41) that the parameter p_g is the relative contribution of the Gaussian-like $g_1(u)$ to the Rutherford-like $g_2(u)$. It is reasonable to demand that $g(u)$ be continuous and smooth on $[-1, 1]$. Taking continuity and smoothness at $u = u_0$ yields the following constraints:

$$p_g g_1(u_0) = (1 - p_g) g_2(u_0), \quad (2.46)$$

$$a \cdot p_g g_1(u_0) = (1 - p_g) g_2(u_0) \cdot \frac{d_r}{b_r - u_0}. \quad (2.47)$$

From Eq. (2.46), it is easy to see that

$$p_g = \frac{g_2(u_0)}{g_1(u_0) + g_2(u_0)}. \quad (2.48)$$

Finding b_r

Observe from Eq. (2.41) that the parameter b_r is the relative u offset of the Rutherford-like distribution. For a classical Rutherford distribution, $b_r = 1$. From Eq. (2.47),

$$a = \frac{d_r}{b_r - u_0}.$$

Rearranging this yields

$$b_r = \frac{a}{d_r} + u_0. \quad (2.49)$$

Finding q_g

Lastly, q_g is found by knowing that $g(u)$ must give the same mean value as Lewis theory. Observe from Eq. (2.41) that the parameter q_g is the relative con-

tribution of the varying functions $g_1(u)$ and $g_2(u)$ to the constant function $g_3(u)$. GEANT4 [19] shows that

$$q_g = \frac{(1 - \frac{\lambda_{10} - \lambda_{11}}{\lambda_{10}})^{\frac{t}{\lambda_{10} - \lambda_{11}}}}{p_g \langle u \rangle_1 + (1 - p_g) \langle u \rangle_2}, \quad (2.50)$$

where λ_{10} is the value of the first transport free mean path at the beginning of the step, λ_{11} is this value at the end of the step, t is the true path length, and $\langle u \rangle_i$ is the mean value of u computed from the distribution $g_i(u)$.

Summary

In summary, the scattering model used by G4Beamline is based on the Geant4 model, which includes Lewis theory. The full form of the scattering equation is given by Eq. (2.41). This model has 9 parameters which are summarized in Table 2.1. As can be seen in the G4Beamline validation documents [18], this model works quite well. G4Beamline sets a precedent to use theory in conjunction with empirical parameters—a philosophy that this work also uses. Moreover, as is seen in the next chapter, this work employs the piecewise Gaussian-like and Rutherford-like distribution in its scattering algorithm.

CHAPTER 3

STOCHASTIC PROCESSES IN COSY INFINITY

In this chapter, the new algorithms implemented into COSY Infinity by this work is elaborated upon. First, energy straggling via Landau theory is detailed, including novel corrections. Next, the multiple scattering algorithm (which resembles the G4Beamline algorithm discussed in Section 2.4) and its implementation is discussed. Finally, the transverse displacement and temporal displacement algorithms are shown.

3.1 Energy Straggling in COSY

For energy loss, COSY uses the Bethe-Bloch equation (Eq. (2.5)) to find the mean energy loss. This can be done in the transfer map paradigm since average energy loss is a deterministic effect. However, this work is concerned with simulating realistic stochastic fluctuations about the average energy loss. For this reason, this work has implemented Landau theory [21] to describe the straggling distribution. Landau theory is discussed in detail in Section 2.1.2.

Due to its long tail, the average of the Landau distribution is undefined. This is clearly nonphysical. Recall from Eq. (2.16) that the universal Landau parameter is

$$\lambda = \frac{\epsilon - \langle \epsilon \rangle}{\xi} - (1 - C_{Euler}) - \beta^2 - \ln(\xi/T_{max}),$$

where ϵ is the energy loss, C_{Euler} is the Euler constant (≈ 0.577), $\beta = v/c$ is the relativistic velocity, and T_{max} is the maximum maximum transferrable energy from an incident muon to an electron at rest. However, this means that fluctuations about the mean energy loss ($\epsilon - \langle \epsilon \rangle$) are also divergent given enough samples. The possibility

Why?

of divergence results in a sensitivity to step size since smaller steps effectively produce a large sample size. In order to combat this, an artificial cutoff is given to λ such that the average Landau ϵ is equal to the average Bethe-Bloch energy loss (ϵ). That is, it is required that

$$\begin{aligned}\langle \lambda \rangle &= \left\langle \frac{\epsilon - \langle \epsilon \rangle}{\xi} \right\rangle - (1 - C_{Euler}) - \beta^2 - \ln(\xi/T_{max}) \\ &= -(1 - C_{Euler}) - \beta^2 - \ln(\xi/T_{max}).\end{aligned}$$

If this cutoff is λ_{max} , then $\langle \lambda \rangle$ can be calculated by the definition of an average over the range $[0, \lambda_{max}]$:

$$\langle \lambda \rangle = \frac{\int_0^{\lambda_{max}} \lambda * f(\lambda) d\lambda}{\int_0^{\lambda_{max}} f(\lambda) d\lambda}.$$

The task then is to numerically find λ_{max} such that it satisfies

$$\frac{\int_0^{\lambda_{max}} \lambda * f(\lambda) d\lambda}{\int_0^{\lambda_{max}} f(\lambda) d\lambda} = -(1 - C_{Euler}) - \beta^2 - \ln(\xi/T_{max}).$$

GEANT version 3.21 [31] suggests the following form for λ_{max} :

$$\lambda_{max} = 0.60715 + 1.1934 \langle \lambda \rangle + (0.67794 + 0.052382 \langle \lambda \rangle) \exp[0.94753 + 0.74442 \langle \lambda \rangle] \quad (3.1)$$

*Confusing.
You said
Urbán is
model fn
Multi. Scat.,
not MC
Tx*

note that GEANT4 does not have a section on the Landau cutoff since the Urbán model is used instead). However, a plot of required cutoffs (λ_{max}) vs. desired means ($\langle \lambda \rangle$) was produced independently in this work with muon ionization cooling parameters in mind. The form suggested by GEANT3 (see, e.g., Eq. (3.1)) was used to fit the plot in Figure 3.1. The determined form of the function is

$$\lambda_{max} = 0.517891 + 1.17765 \langle \lambda \rangle + (0.476074 + 0.00880733 \langle \lambda \rangle) \exp[1.15467 + 0.984008 \langle \lambda \rangle]. \quad (3.2)$$

Based on Eq. (2.16), it is possible to find ϵ_{max} :

$$\epsilon_{max} = \xi[\lambda_{max} + (1 - C_{Euler}) + \beta^2 + \ln(\xi/T_{max})] + \langle \epsilon \rangle.$$

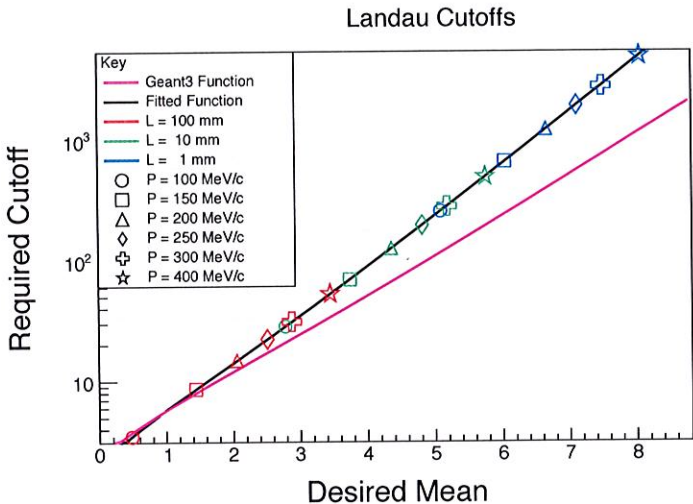


Figure 3.1: λ_{max} vs. $\langle \lambda \rangle$ over a variety of liquid hydrogen absorber lengths and initial beam momenta. The pink line is the form given by GEANT3 (see Eq. (3.1)) and the black line is the fitted curve (see Eq. (3.2)). The data points are combinations of shapes and colors, as seen in the key. For example, since green means 10 mm and the square means 150 MeV/c, the green square data point represents the required cutoff for 150 MeV/c muons passing through 10 mm of liquid hydrogen. Liquid hydrogen was chosen in order to match the results in Section 5.1. However, other materials (such as lithium hydride) still fall within the desired $\langle \lambda \rangle$ range of [0, 9].

Therefore, during the energy loss sampling, if any energy loss ϵ is selected which is greater than ϵ_{max} it is discarded and the sampling is performed again. However, if the result has been discarded 100 times, the particle is assumed to have lost too much energy and is considered lost.

3.2 Multiple Scattering in COSY Infinity

Similar to ICOOL's fifth method of scattering, the Rutherford model (see Section 2.2), COSY utilizes a piecewise distribution function which is Gaussian at small angles (as Goudsmit and Saunderson suggested [28]) and Rutherford-like at large angles. This Rutherford-like tail is derived at length in Appendix B, with a review of the relevant particle physics symbols and methods in Appendix C. The result is the (differential) Mott scattering cross section:

$$\frac{d\sigma}{d\Omega} \propto \frac{1 + \frac{(\beta\gamma)^2}{2}(1 + \cos\theta)}{(1 - \cos\theta)^2}, \quad (3.3)$$

where $d\sigma/d\Omega$ is the differential scattering cross section, β is the relativistic velocity, $\gamma = 1/\sqrt{1 - \beta^2}$, and θ is the scattering angle. Observe that for the non-relativistic limit $\beta \rightarrow 0$ the cross section does indeed approach a Rutherford distribution (Eq. (2.29)). The practical implementation of this cross section into the probability distribution function is discussed in Section 3.2.1.

3.2.1 Implementation. Now that the forms of the Gaussian and Rutherford-like scattering cross sections have been obtained, implementation of these cross sections is discussed. In this work, when a particle passes through matter, the change in angle of this particle is selected from a probability distribution. For $u = \cos\theta$, this distribution should be Gaussian-like at small angles [28] and follow the Mott cross section at large angles. Based on a Gaussian-like cross section for small angles and

the cross section in Eq. (3.3), the distribution has been chosen as

$$g(u) = \begin{cases} e^{-a(1-u)} & u_0 \leq u \\ \zeta \frac{1 + \frac{1}{2}(\beta\gamma)^2(1+u-b_c)}{(1-u+b_c)^2} & u \leq u_0 \end{cases}, \quad (3.4)$$

where u_0 is the cutoff between the Gaussian-like distribution and the Mott distribution, ζ is the amplitude of the Mott distribution, and b_c is the relative u shift of the Mott distribution. The parameter a is an empirical parameter, based off Highland theory [29], and can be found in Eq. (2.42). Eq. (2.42) is reproduced here for convenience:

$$a = \frac{0.5}{1 - \cos \theta_0}.$$

where θ_0 has the form [29]

$$\theta_0 = \frac{E_s}{p\beta} \sqrt{\frac{L}{X_0}}.$$

However, this definition has been extended in this work to include empirical corrections based on GEANT4's [19] treatment of θ_0 (see Eq. (2.43)):

$$\theta_0 = \frac{13.6 \text{ eV}}{\beta p} \sqrt{\frac{L}{X_0} \left[1 + h_1 \ln \frac{L}{X_0} + h_2 \left(\ln \frac{L}{X_0} \right)^2 \right]}. \quad (3.5)$$

The Highland correction terms have been chosen novelly in this work as $h_1 = 0.12$ and $h_2 = 0.006$. This was done by fitting the curve given by Eq. (3.4) to match the MuScat results [32], the results of which can be found in Section 5.2. It is important to note that these correction terms are tunable for future data of muons through higher Z material.

u_0 is the point at which the Gaussian term meets the Mott tail. This has been chosen empirically as

$$u_0 = 1 - \frac{4.5}{a}. \quad (3.6)$$

This parameter was fitted alongside the Highland correction terms to match the experimental results in [32].

ζ and b_c are the angular scattering distribution's amplitude and offset for the tail. These are found by demanding continuity and smoothness at u_0 :

$$e^{-a(1-u_0)} = \zeta \frac{1 + \frac{1}{2}(\beta\gamma)^2(1+u_0-b_c)}{(1-u_0+b_c)^2},$$

$$ae^{-a(1-u_0)} = \zeta \frac{1 + \frac{1}{2}(\beta\gamma)^2(1+u_0-b_c)}{(1-u_0+b_c)^2} \left(\frac{2}{1-u_0+b_c} + \frac{(\beta\gamma)^2}{2 + (\beta\gamma)^2(1+u_0-b_c)} \right).$$

Then

$$a = \frac{2}{1-u_0+b_c} + \frac{(\beta\gamma)^2}{2 + (\beta\gamma)^2(1+u_0-b_c)}.$$

Solving this for $(u_0 - b_c)$ yields a quadratic with the solution

$$b_c = u_0 + \frac{A_2 + \sqrt{A_2^2 - 4A_1A_3}}{2A_1}, \quad (3.7)$$

with

$$A_1 = -a(\beta\gamma)^2,$$

$$A_2 = -(\beta\gamma)^2 - 2a,$$

$$A_3 = (\beta\gamma)^2(a - 3) + 2a - 4.$$

The continuity condition for $g(u_0)$ yields the expression for ζ :

$$\zeta = \frac{e^{-a(1-u_0)}(1-u_0+b_c)^2}{1 + \frac{1}{2}(\beta\gamma)^2(1+u_0-b_c)}. \quad (3.8)$$

Now that the distribution function has a concrete form, it is implemented by inverting the cumulative distribution function (CDF). Let $G(u)$ be the integral of $g(u)$. Then the variable G is uniformly sampled over the region $[0, G_{max}]$. If $G \geq G(u_0) \equiv G_0$ then the Gaussian part of the distribution is used to generate u (i.e., $G(u \geq u_0)$). Otherwise, the tail of the distribution is used. Figure 3.2 shows $G(u)$ for $L = 100 \text{ mm}$, $p = 200 \text{ MeV}/c$, and a radiation length or $X_0 = 8.66 \text{ m}$ (to simulate a liquid hydrogen target).

which?
traversing?

citation?
(disagrees w/ PDG?)

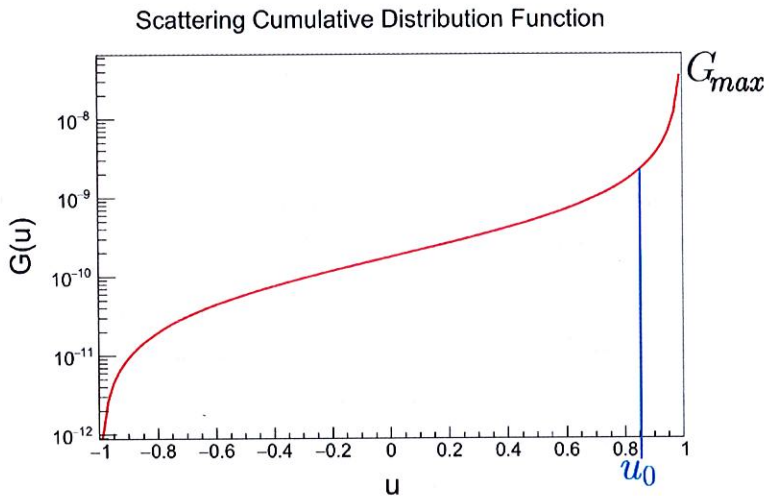


Figure 3.2: Example of the cumulative angular distribution function for muons with momenta of 200 MeV/c passing through 100 mm of liquid hydrogen. Note that the y axis is log scaled due to the very sharp peak. Furthermore, note that u_0 is greatly exaggerated, since its actual value for these parameters is 0.99987.

However, since this is a piecewise function, the CDF is inverted in pieces. The tail of the CDF is found first:

$$G(u \leq u_0) = \int_{-1}^u \zeta \frac{1 + \frac{1}{2}(\beta\gamma)^2(1 + u' - b_c)}{(1 - u' + b_c)^2} du'.$$

This integral may be solved by substituting $v = 1 - u' + b_c$ and simply splitting the numerator into separate parts:

$$\begin{aligned} G(u \leq u_0) &= -\zeta \left(1 + \frac{1}{2}(\beta\gamma)^2(1 - b_c)\right) \int_{2+b_c}^{1-u+b_c} v^{-2} dv - \\ &\quad \zeta \frac{(\beta\gamma)^2}{2} \int_{2+b_c}^{1-u+b_c} (v^{-2} - v^{-1} + b_c v^{-2}) dv, \\ G(u \leq u_0) &= \zeta \left(1 + (\beta\gamma)^2\right) \left(\frac{1}{1 - u + b_c} - \frac{1}{2 + b_c}\right) + \zeta \frac{(\beta\gamma)^2}{2} \ln \left(\frac{1 - u + b_c}{2 + b_c}\right). \end{aligned} \quad (3.9)$$

The goal is to solve Eq. (3.9) for $u(G)$. However, using direct inversion is extremely difficult and involves special functions. Therefore, it is more prudent to generate u via bisection method (see Figure 3.3). In this method, the true G is sampled uniformly on the range $[0, G_{max}]$, where $G_{max} \equiv G(1)$. Explicitly, G_{max} is

$$\begin{aligned} G_{max} \equiv G(1) &= \int_{-1}^{u_0} \zeta \frac{1 + \frac{1}{2}(\beta\gamma)^2(1 + u - b_c)}{(1 - u + b_c)^2} du + \int_{u_0}^1 e^{-a(1-u)} du, \\ &= G_0 + \frac{1}{a} - \frac{e^{-a(1-u_0)}}{a}. \end{aligned}$$

If $G < G_0$, then the tail is sampled. A trial u called \bar{u} (as in ‘average’) is selected from some range which is known to contain the actual u . The range is described as $[u_{min}, u_{max}]$, and $\bar{u} = (u_{min} + u_{max})/2$.

Initially, the range is chosen as $u_{min} = -1$ and $u_{max} = u_0$ (since that is the largest range on which $G(u \leq u_0)$ is valid and hence u is guaranteed to be in this range). $\tilde{G} \equiv G(\bar{u})$ is found using Eq. (3.9), and then the routine is subject to the

Explaining why algorithm works?

Scattering Cumulative Distribution Function

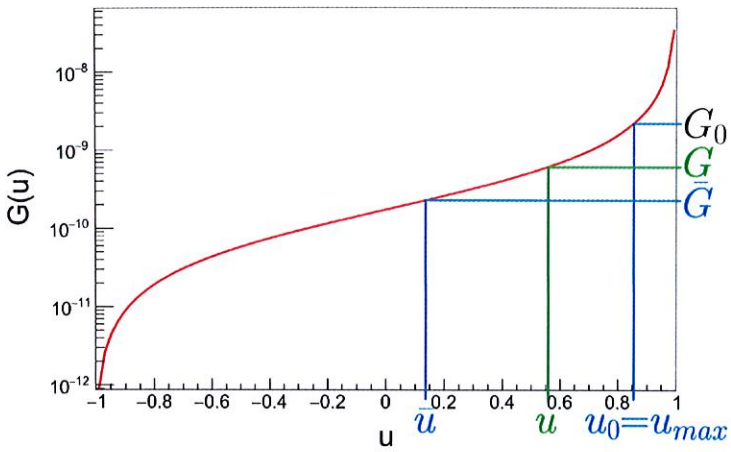


Figure 3.3: Example of the first iteration of the algorithm to obtain the true u (in green). The true G is chosen uniformly from $G \in [0, G_{max}]$. If $G < G_0$, then the tail is sampled via bisection method. In this case, since $\bar{G} < G$, \bar{u} is the new u_{min} and \bar{u} is calculated again.

following conditions:

- If $\bar{G} \in [G - \delta G, G + \delta G]$ then $u = \bar{u}$, return value.
- If $\bar{G} < G - \delta G$ then $u_{min} = \bar{u}$, rerun with new u_{min} .
- If $\bar{G} > G + \delta G$ then $u_{max} = \bar{u}$, rerun with new u_{max} .

δG is a precision, and has been chosen for this work as $\delta G = 10^{-8}$. However, it is conceded that in the future δG should be a percentage of G_{max} rather than an absolute number.

For the peak, $u_0 \leq u$ and so the CDF becomes

$$G(u_0 \leq u) = \int_{-1}^{u_0} g(u) du + \int_{u_0}^u e^{-a(1-u)} du.$$

The first term is simply G_0 , the cumulative distribution function at u_0 . The second term is easily integrable and yields

$$G(u_0 \leq u) = G_0 + \frac{e^{-a(1-u)} - e^{-a(1-u_0)}}{a}. \quad (3.10)$$

The inversion of this function is quite straightforward, and is

$$u(G_0 \leq G) = 1 + \frac{1}{a} \ln [a(G - G_0) + e^{-a(1-u_0)}]. \quad (3.11)$$

Therefore, if $G \in [0, G_{max}]$ is greater than or equal to G_0 , then it is simply inserted into Eq. (3.11) and the true u is obtained.

It is a subtle yet important point to note that the Mott cross section (Eq. (3.3)), upon which the probability distribution function $g(u)$ in Eq. (3.4) is based, assumes an on-axis straight line trajectory. An on-axis trajectory is equivalent to saying that $p_z = p$ and $x = y = p_x = p_y = 0$. For particles that are not on-axis, the reference frame both before and after scattering is rotated such that $p = p_z$. A particle that is not on-axis is exemplified in Figure 3.4. Here, the muon has some angle θ_o before entering the medium. The lab frame has transverse and longitudinal position axes T and z and the rotated frame has corresponding transverse and longitudinal position axes T_R and z_R .

To reiterate, prior to scattering, in the rotated frame the rotated longitudinal momentum is the total momentum ($p_{z,R} = p$) and the rotated transverse momentum is zero ($p_{T,R} = 0$). After scattering, $g(u)$ yields the scattered angle θ_s . The rotated longitudinal momentum is no longer necessarily equal to the total momentum, but rather $p_{z,R} = p \cos \theta_s$. Similarly, the rotated transverse momentum is not necessarily zero but instead $p_{T,R} = \sqrt{p^2 - p_{z,R}^2}$. Note that since energy straggling has already

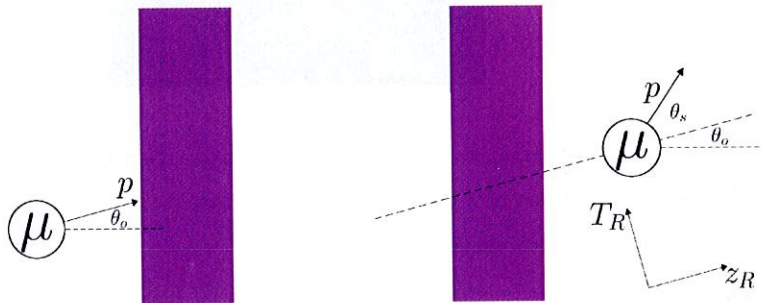


Figure 3.4: Example of a muon entering an absorber (purple) with some nonzero initial angle θ_o . The muon then scatters an angle θ_s with respect to its initial momentum \vec{p} . The scattering distribution $g(u)$ assumes a straight, on-axis particle ($x = y = p_x = p_y = 0$) before scattering, and so is in the rotated frame represented by T_R, z_R .

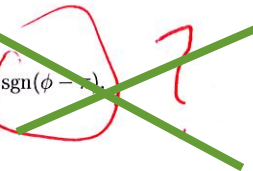
been accounted for, the total momentum p stays constant throughout the scattering process and regardless of reference frame.

Due to cylindrical symmetry, the transverse momentum in the rotated frame $p_{T,R}$ must be distributed uniformly into the transverse x and y momenta. The constraint upon the transverse momentum in any frame is

$$p_T^2 = p_x^2 + p_y^2.$$

Therefore, the variable ϕ is selected uniformly from $[0, 2\pi]$. The x and y momenta in the rotated frame are

$$\begin{aligned} p_{x,R} &= P_{T,R} \cos \phi \cdot \text{sgn}(\phi - \pi), \\ p_{y,R} &= P_{T,R} \sin \phi, \end{aligned}$$



where sgn is the sign function defined by

$$\text{sgn}(x) = \begin{cases} -1 & \text{for } x < 0 \\ 0 & \text{for } x = 0 \\ 1 & \text{for } x > 0 \end{cases}.$$

The rotated x and y momenta ($p_{x,R}$ and $p_{y,R}$) are subsequently transformed into the lab frame.

To summarize, the angular distribution used by COSY Infinity is based on a piecewise function which is Gaussian for small angles [28] and has a Mott tail for large angles. This distribution is represented by $g(u)$ in Eq. (3.4), where $u \equiv \cos \theta$. $g(u)$ has four parameters: a , an empirical parameter that is based on Highland theory [29] and is dependent on some critical angle θ_0 , defined in Eq. (3.5); u_0 , the empirical cutoff angle that distinguishes which angles are Gaussian and which are not, found by Eq. (3.6); b_c , a parameter derivable from smoothness of g at u_0 , which represents the offset of the Mott tail, found in Eq. (3.7); and ζ , a parameter derivable from

continuity of g at u_0 which represents the amplitude of the Mott tail, found in Eq. (3.8). From $g(u)$, its antiderivative $G(u)$ may be found and a particular G may be picked from the range $[0, G_{max}]$. If $G < G_0 \equiv G(u_0)$, then u comes from the Mott tail and a bisection method is used to find u . If $G_0 \leq G$ then u comes from the Gaussian peak and $G(u)$ may be inverted to find $u(G)$. This scattered angle must then be rotated into the lab frame and the additional transverse momentum must be uniformly distributed into p_x and p_y .

3.3 Transverse Displacement in COSY Infinity

Due to multiple scattering events, when a particle traverses matter, a direct correlation between the particle transverse position and scattered angle is not always clear. Two identical particles with identical initial conditions may end up with identical scattered angles but different transverse positions (see Figure 3.5). This is because these two particles may take different paths through the absorber. While both of these paths may lead to a similar final angle with respect to the z axis, the positions are likely different due to their trajectories.

For this reason, transverse corrections have been implemented in COSY. Due to a lack of experimental data at the time, COSY was compared to G4Beamline across several initial momenta and absorber lengths. The result was

$$x = x_o + x_D + \text{Gaus}(\theta_{diff} * L/2, \theta_c/(2\sqrt{3})), \quad (3.12)$$

where x_o is the original x position, $x_D = L * P_{x,o}/P_{z,o}$ is the deterministic gain in x , and $\text{Gaus}(\mu, \sigma)$ is a randomly selected number from a Gaussian distribution with mean μ and standard deviation σ . The forms of μ and σ were selected based on a combination of the Particle Data Group [15] and Fernow and Gallardo [33]. Note that the average $\mu = \theta_{diff} * L/2$ represents the transverse displacement that would have occurred if all of the angular scattering had happened at the point $L/2$. $\theta_{diff} = \theta_{final} - \theta_o$ is the

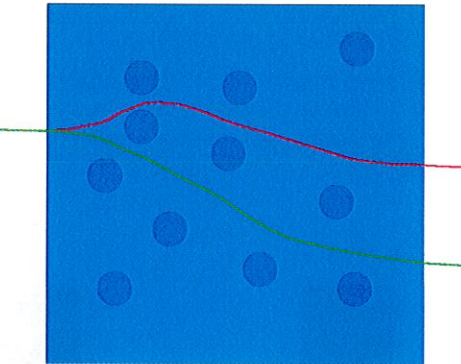


Figure 3.5: Two examples of true paths which a particle might take when traversing a medium. Note that both the red and green paths have the same final scattered angle but different transverse positions.

amount of deflection which occurred due to scattering and $\theta_c = 13.6 \text{ eV}/\beta p \cdot \sqrt{1/X_0}$ is the coefficient from England theory [29].

The fitting of these parameters is discussed next. As previously mentioned, the data for the fits were generated by G4Beamline [18]. Here, a particular example of a simulation of 10^6 particles passing through 1 cm of liquid hydrogen is shown. The initial beam distribution was a pencil beam of momentum 200 MeV/c. A plot of the histogram of (x, p_x) phase space can be seen in Figure 3.6. It can be seen in Figure 3.7 that the cross section of a given transverse momentum results in a nearly-Gaussian x histogram. It can also be inferred from the figure that the mean and standard deviation of the Gaussian fit varies depending on which p_x is chosen. For example, higher values of p_x appear to have both a larger mean and standard deviation. While this trend is conceptual, it aids in the understanding of the form of Eq. (3.12).

The phase space portrait in Figure 3.8 shows that the distribution is only locally Gaussian. However, fitting in the range of $p = 100\text{--}400 \text{ MeV}/c$, $L = 1\text{--}100 \text{ mm}$ has shown that this is a good approximation for the majority of particles (see Section 5.1).

An example of the success of this implementation can be seen in Figure 3.9, where 10^6 muons of momentum $250 \text{ MeV}/c$ were simulated through 100 mm of liquid hydrogen. The simulation was carried out in both COSY and ICOOL [17] with good agreement.

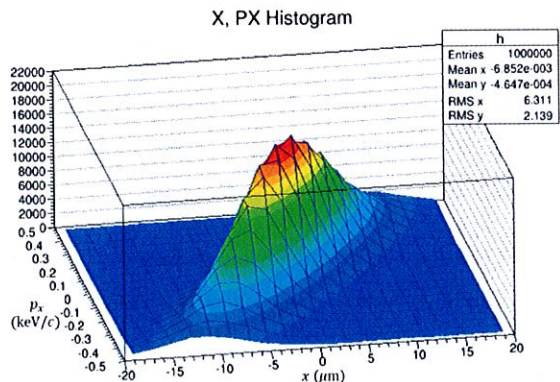


Figure 3.6: 2D histogram of (x, p_x) phase space for 10^6 muons of momentum $200 \text{ MeV}/c$ passing through 1 cm of liquid hydrogen.

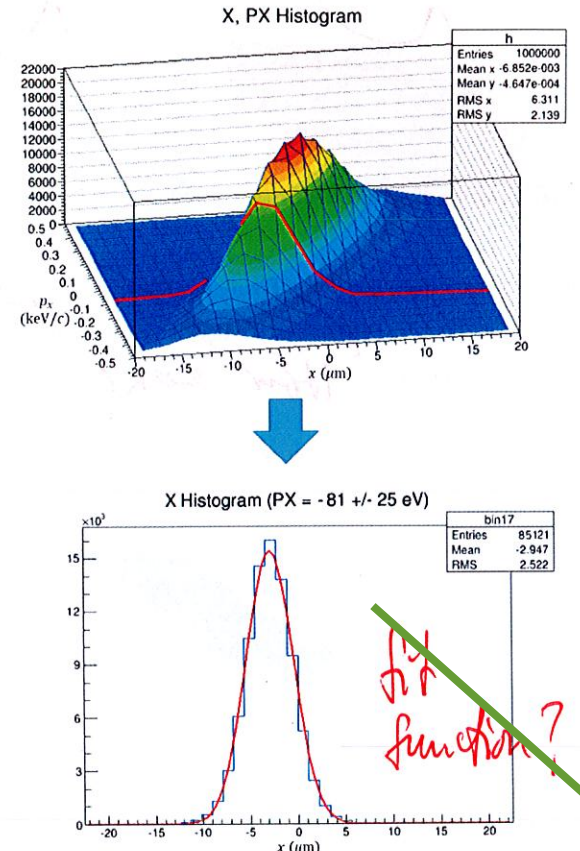


Figure 3.7: Cross section of Figure 3.6 at $p_x = (-0.081 \pm 0.025) \text{ keV}/c$. The resulting x histogram fit (in red) is nearly Gaussian.

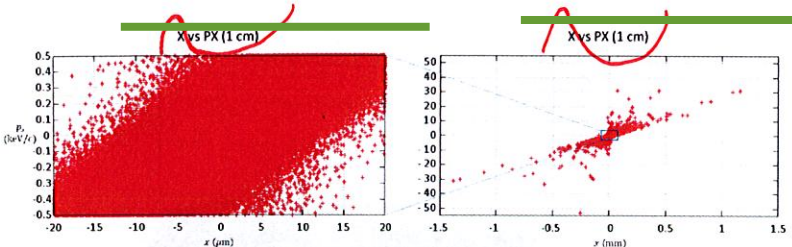


Figure 3.8: Phase space portrait of Figure 3.6. Observe that the bulk in Figure 3.6 is represented on the left. Further observe that the extrema of this distribution do not follow a Gaussian curve.

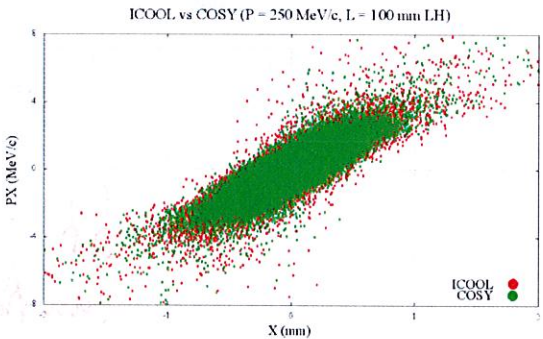


Figure 3.9: Sample simulation results for the implementation of the transverse coordinate correction algorithm.

3.4 Temporal Displacement in COSY Infinity

define For the time of flight offset, both the deterministic and stochastic processes are handled in the same routine. To first order, the particle decelerates at some average rate through an absorber of length L . If a is the constant acceleration then

$$v_f = v_o + a\Delta t,$$

or

$$a = \frac{v_f - v_o}{\Delta t}.$$

At the same time, $v_f^2 = v_o^2 + 2aL$, and so

$$a = \frac{v_f^2 - v_o^2}{2L}.$$

Then

$$\Delta t = \frac{(v_f - v_o)2L}{v_f^2 - v_o^2}.$$

Given $\beta = p/E$ and $v = \beta c$, then

$$\Delta t = \frac{\left(\frac{p_f}{E_f} - \frac{p_o}{E_o}\right)2L}{\left(\frac{p_f^2}{E_f^2} - \frac{p_o^2}{E_o^2}\right)c}. \quad (3.13)$$

However, COSY does not have a time variable, but rather a variable ℓ that is described as the time-of-flight in units of length. In COSY [4], this is defined as

$$\ell = \frac{-(t - t_0)v_0\gamma}{1 + \gamma},$$

where the subscript 0 signifies the reference particle. Let the time before a step be denoted t_1 and the time after a step denoted t_2 . Then to find ℓ_2 given ℓ_1 and Δt from Eq. (3.13), observe that

$$\begin{aligned} \ell_1 &= \frac{(t_{01} - t_1)v_{01}\gamma_1}{1 + \gamma_1} = (t_{01} - t_1)A_1 \\ \ell_2 &= \frac{(t_{02} - t_2)v_{02}\gamma_2}{1 + \gamma_2} = (t_{02} - t_2)A_2, \end{aligned} \quad (3.14)$$

where

$$A_n \equiv v_{0n}\gamma_n/(1 + \gamma_n) \quad \text{for } n = 1, 2. \quad (3.15)$$

Then

$$\begin{aligned} \ell_2 - \ell_1 &= (t_{02} - t_2)A_2 - (t_{01} - t_1)A_1 \\ &= [(t_{02} - t_{01}) + t_{01}] - [(t_2 - t_1) + t_{01}]A_2 - (t_{01} - t_1)A_1 \\ &= (\Delta t_0 - \Delta t)A_2 + (t_{01} - t_1)A_2 - (t_{01} - t_1)A_2 \\ &= (\Delta t_0 - \Delta t)A_2 + (t_{01} - t_1)(A_2 - A_1). \end{aligned}$$

Eq. (3.14) says that $t_{01} - t_1 = \ell_1/A_1$. Moving ℓ_1 to the right hand side,

$$\begin{aligned}\ell_2 &= (\Delta t_0 - \Delta t)A_2 + \frac{\ell_1}{A_1}(A_2 - A_1) + \ell_1 \\ &= (\Delta t_0 - \Delta t)A_2 + \ell_1\left(\frac{A_2 - A_1}{A_1} + \frac{A_1}{A_1}\right) \\ &= (\Delta t_0 - \Delta t)A_2 + \ell_1\frac{A_2}{A_1}.\end{aligned}$$

Substituting for A_n via Eq. (3.15) yields the final result

$$\ell_2 = \frac{(\Delta t_0 - \Delta t)v_{02}\gamma_2}{1 + \gamma_2} + \ell_1 \frac{v_{02}\gamma_2(1 + \gamma_1)}{v_{01}\gamma_1(1 + \gamma_2)}. \quad (3.16)$$

Using Eq. (3.16), Δt from Eq. (3.13) can be directly input into the new COSY variable for time-of-flight in units of length. Figure 3.10 shows the simulation results for a beam of 10^6 muons of momentum 172 MeV/c passing through 109 mm of liquid hydrogen, which were the parameters of the MuScat experiment [32]. The COSY results are shown alongside ICOOL [17]. Note that the agreement is quite good. ICOOL displays a thicker bulk at around 0.430 ns, but it is approximately 1 ps in width—about 0.2% of the average time-of-flight.

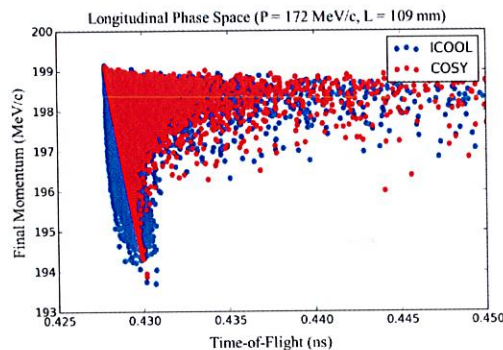


Figure 3.10: Sample simulation results for the implementation of the temporal displacement algorithm discussed in this section.

CHAPTER 4

SOFTWARE IMPLEMENTATION

This chapter discusses in detail the organization and internal structure of the code ~~which~~^{that} is the implementation of the novel algorithms discussed in Chapter 3. For reference, a reproduction of the code itself may be found in Appendix F. First, the user input is discussed. Next, the *cosy.fox* level of the code is examined. Finally, the structure of the FORTRAN code is briefly considered. Figure 4.1 is referenced during these discussions.

In addition to the user's input file, COSY also uses a *cosy.fox* file. This file contains a plethora of global variables, functions, and routines which the user can access. However, *cosy.fox* can also be used to hide most of the complicated machinery from the user. For example, for this study the routines in *cosy.fox* transform the COSY coordinates (x, a, y, b, ℓ, d) into absolute coordinates (x, p_x, y, p_y, t, E) , and then relay the information to the FORTRAN code. Both the user file and the *cosy.fox* file are written in COSYScript, the programming language of COSY.

4.1 User Input

As with the deterministic absorber routine previously present in COSY, WA, the user must first call the procedure

BBC $<Z> <A> <\rho> <I> <\delta> <C>$;

This stores the material parameters in a global array. The arguments are the nuclear charge Z , the atomic mass A , the density of the material ρ , the ionization energy

⁴Recall from Eq. (1.1) that x and y are the transverse coordinates; $a = p_x/p_0$; $b = p_y/p_0$; $\ell = -(t - t_0)v_0\gamma/(1 + \gamma)$; $\delta = (K - K_0)/K_0$; E is the total energy; K is the kinetic energy; and the subscript 0 denotes the coordinate of the reference particle.

"—" is not a virg

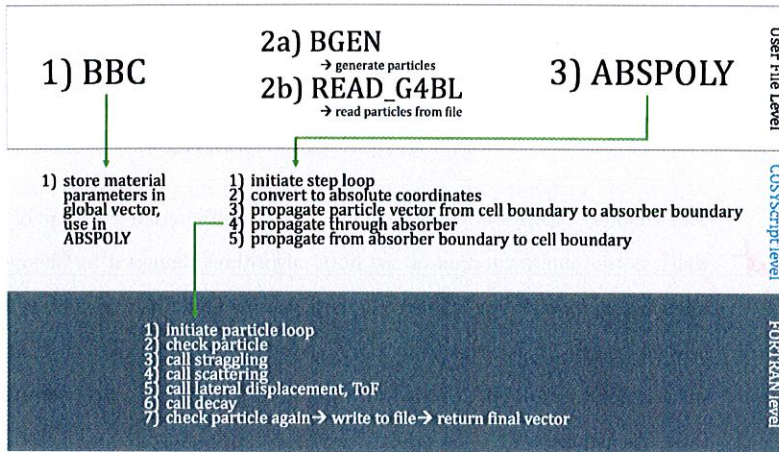


Figure 4.1: A flowchart for the structure of the new COSY routines implemented in this work.

I , the density correction δ , and the shell correction C . Next, the user must either generate a distribution of particles or read a distribution of particles from a file. Using $BGEN <n> <V> <\mu_x> <\sigma_x> <\mu_{px}> <\sigma_{px}> <\mu_y> <\sigma_y> <\mu_{py}> <\sigma_{py}> <\mu_t> <\sigma_t> <\mu_{pt}> <\sigma_{pt}>$;

the user can generate a Gaussian beam of n particles into a 2D vector V . Note that in COSY, a 2D vector is a vector of vectors and is not the same data class as an array.

Alternatively, the user may use

$READ_G4BL <file> <n> <V>$; ASCII only?

to read a G4Beamline-formatted file of n particles and store it into a 2D vector V . Finally, the user can call

$ABSPOLY <S_1> <S_2> <n> <L> <A> <V> <X_0> <S_n> <L_c> <O>$;

where S_1 ⁵ is an n^{th} order polynomial describing the entrance surface, S_2 is an n^{th}

⁵For a full description of the entrance and exit polynomials S_1 and S_2 , please see the COSY beam physics manual [4], page 33.

order polynomial describing the exit surface, L is the on-axis length of the absorber, A is the aperture, V is the 2D input and output particle vector, X_0 is the radiation length of the material, S_n is the number of steps inside the absorber, L_c is the length of the absorber cell, and O is the output unit number (e.g. "12" to save the results in fort.12). A depiction of the parameters can be found in Figure 4.2.

just 1 number? derive
too complicated? Are there
better?
some?

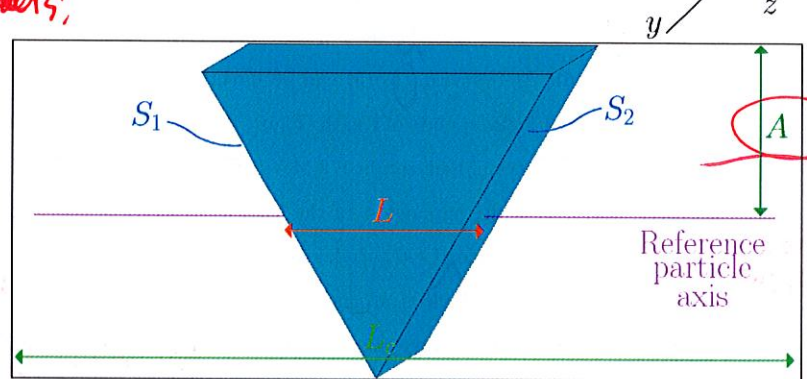


Figure 4.2: Cartoon example of some of the ABSPOLY parameters.

4.2 COSYScript Level

As previously mentioned, the **ABSPOLY** routine is defined in the external file **cosy.fox**. Here, the step loop over S_n is initialized. Next, input 2D vector V is converted from coordinates relative to the reference particle to absolute coordinates. The particle vector is then propagated from the cell boundary (whose width is defined by L_c) to the absorber (whose on-axis width is defined by L). If $L_c < L$ then no propagation occurs. When the particles are at the absorber boundary, the 2D particle vector V is passed on to the FORTRAN level of the code, where propagation through the absorber takes place. The routine linking the COSYScript and FORTRAN levels

coupling

is STOABS and is discussed in Section 4.3. After the 2D particle vector V is returned, V is propagated to the end of the cell and returned to the user.

4.3 FORTRAN Level

Except for the propagation of particles through the absorber, the processes found in Section 4.2 are much faster in COSYScript than in FORTRAN. This is because processes like coordinate conversion, propagation through a vacuum, etc., are deterministic and can therefore be handled by transfer maps.

The routine

STOABS < V > < m > < L > < MP > < X_0 > < O > < A > < n > ;

takes input parameters from the COSYScript level and returns the input 2D particle vector V . Here, m is the particle mass (taken from the reference particle), L is an n -dimensional array containing the path lengths for each particle, MP is an array containing the material parameters (taken from the global array BETHEBLOCHC set up by the routine BBC), X_0 is the radiation length of the material, O is the output unit number, A is the aperture, and n is the number of particles.

Once the FORTRAN level has this information, a loop over n particles is started. Each particle is checked at the beginning of each loop for the following flags: particle stopped, particle hit aperture, particle missed absorber, drift. If either the particle was stopped ($E \leq m$) or the particle hit the aperture ($x^2 + y^2 \geq A^2$) then the particle is terminated. If the particle missed the absorber completely then the drift flag is turned on. If the drift flag is on then the particle is simply propagated without the stochastic processes called.

Provided that the particle has not been flagged, the particle is subject to energy straggling and then multiple scattering. After these two routines, the lateral displacement and time-of-flight corrections are called. It should be noted that the

order matters for energy straggling and multiple scattering. The order does not matter for lateral displacement and time-of-flight provided that both straggling and scattering have already occurred. Finally, decay can be called. Note that for this work, decay has been turned off completely, and so this step is skipped.

Finally, the particle is checked again. If the output unit number O is not equal to zero then the particles are written to a file. Lastly, the 2D particle vector V is returned to the COSYScript level.

4.4 Summary

Figure 4.1 displays the conceptual process of operating the implemented routines. First, the user defines the material parameters in BBC, which stores these parameters as global variables in the COSYScript level. Next, the user creates a 2D vector of particles, either by generating a Gaussian beam via BGEN or reading particles from a G4Beamline file via READ_G4BL. Finally, the user calls the ABSPOLY routine. ABSPOLY converts the COSY coordinates to and from absolute coordinates and calls the FORTRAN routine to step through the absorber. On the FORTRAN level, each particle is subjected to the energy straggling, multiple scattering, transverse displacement, and time-of-flight algorithms described in Chapter 3. These particles are returned to the user at the end of the propagation.

⇒ can't propagate in through
absorber housing to
evaluate fails

CHAPTER 5

RESULTS

In this chapter, the new COSY routines are benchmarked against both ICOOL and G4Beamline for pencil beams. Recall that a pencil beam is a beam with an RMS of zero for all transverse coordinates. Pencil beams are used in order to simulate a plethora of possible paths and energy losses for a particular initial condition. Both validation against past experiments and predictions of current muon ionization cooling channel efforts are also shown. Since both ICOOL and G4Beamline have automatic variable stepping, their step sizes are left as default unless explicitly stated otherwise.

5.1 Benchmark Against Other Codes

This section briefly discusses the comparison of the new COSY routines with those of two other codes, ICOOL [17] and G4Beamline [18]. Refer to Figures 5.1–5.12 (12 figures, each with three subplots) mentioned here. The benchmarking was done over both the typical momentum range of cooling channels (100, 200, 300, and 400 MeV/c) and various absorber lengths (1, 10, and 100 mm). These simulations were performed using a pencil beam of 5×10^4 muons with the aforementioned momenta through liquid hydrogen. Note that for the transverse position and transverse momentum histograms, the absolute value of the coordinate is plotted. Therefore, the mean is not zero. For COSY, the step size was the entire absorber length. For G4Beamline in the case of a 1 mm absorber, the maximum step size was limited to 0.1 mm. This was done because of the heavy dependence of the transverse position on step size for short absorbers in G4Beamline.

good!

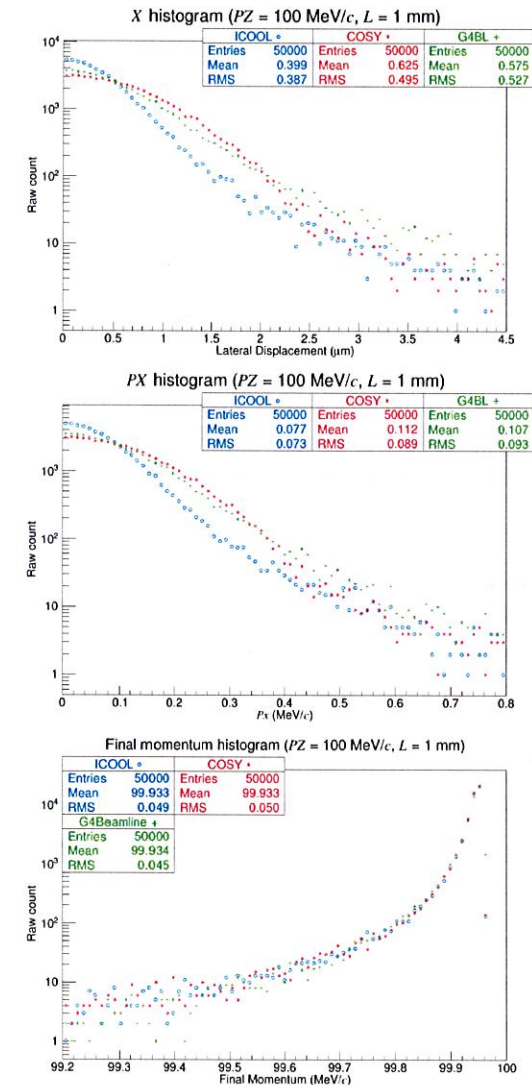


Figure 5.1: Muons of momentum 100 MeV/c through 1 mm liquid hydrogen. Observe that for the x and p_x histograms, COSY and G4Beamline follow a Gaussian-like peak whereas ICOOL follows a Fano peak.

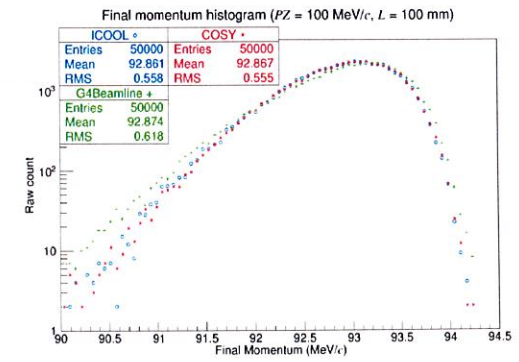
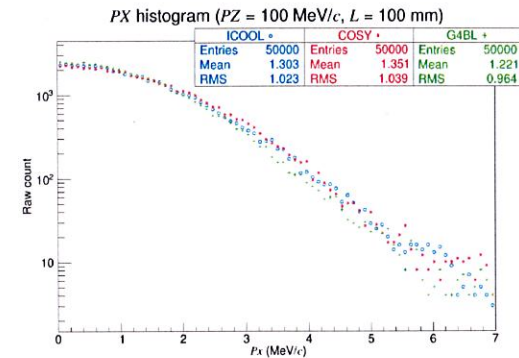
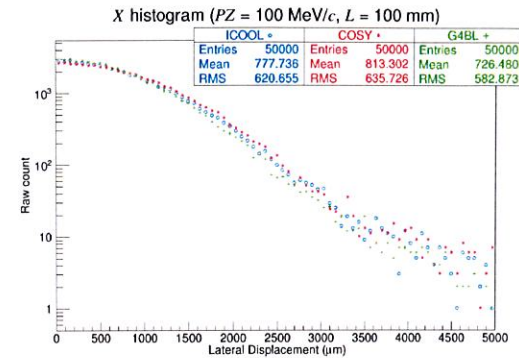
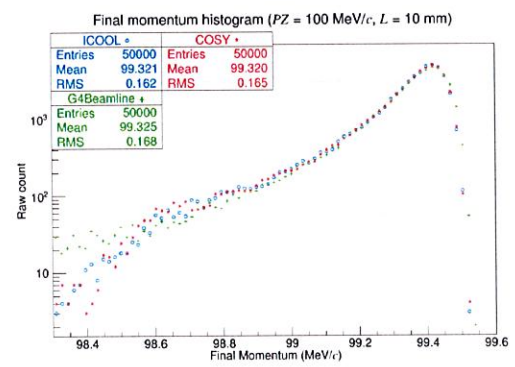
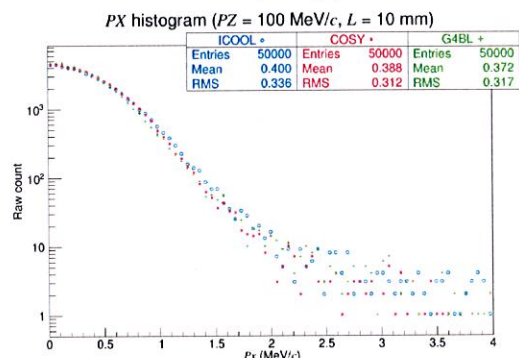
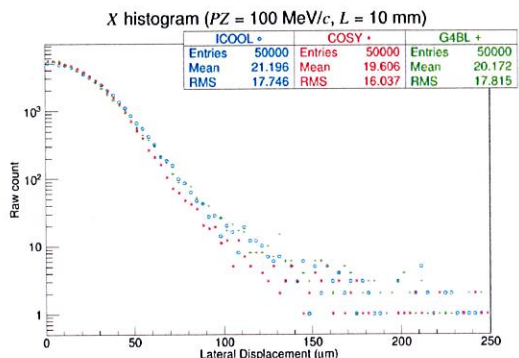


Figure 5.2: Muons of momentum 100 MeV/c through 10 mm liquid hydrogen.

Figure 5.3: Muons of momentum 100 MeV/c through 100 mm liquid hydrogen.

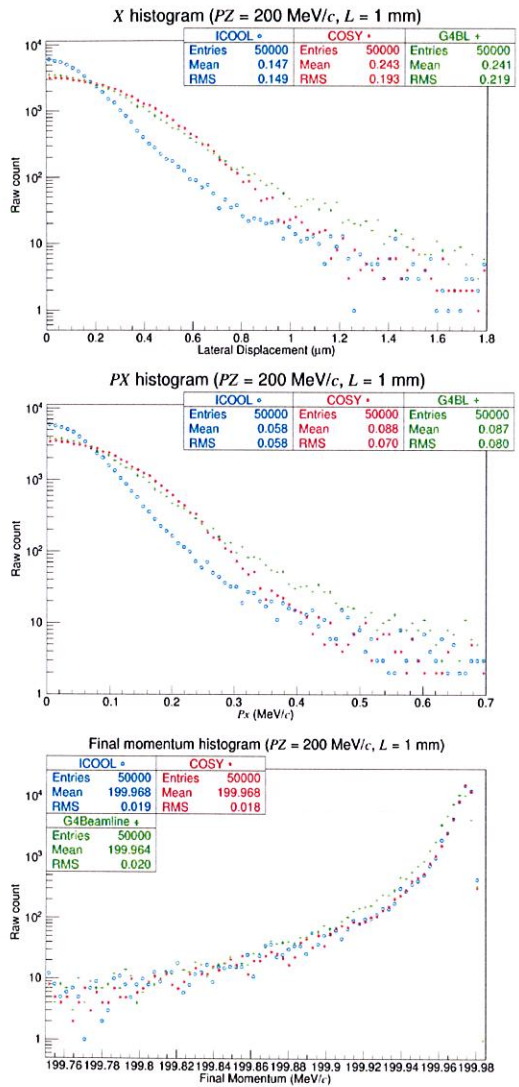


Figure 5.4: Muons of momentum 100 MeV/c through 1 mm liquid hydrogen. Observe that for the x and p_x histograms, COSY and G4Beamline follow a Gaussian-like peak whereas ICOOL follows a Fano peak.

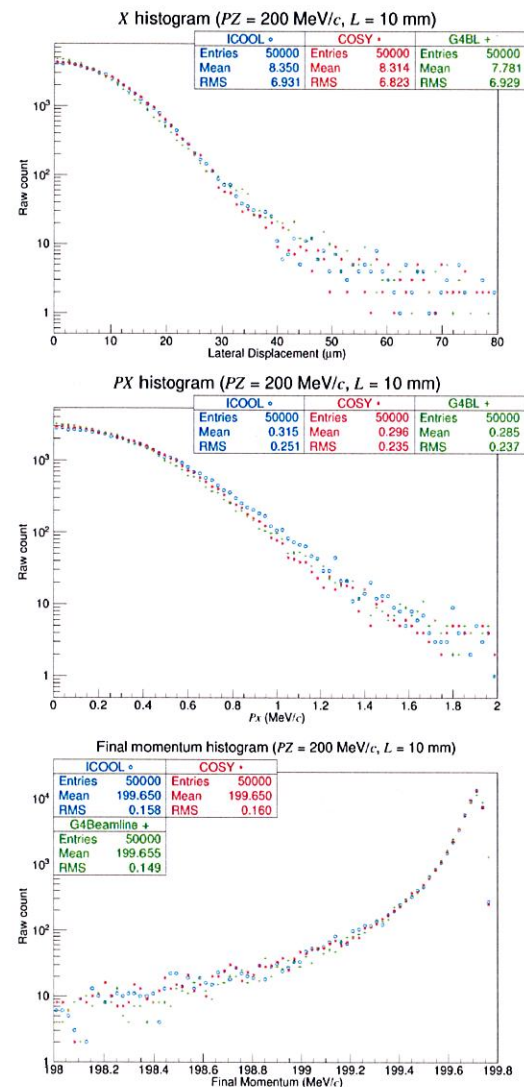


Figure 5.5: Muons of momentum 200 MeV/c through 10 mm liquid hydrogen.

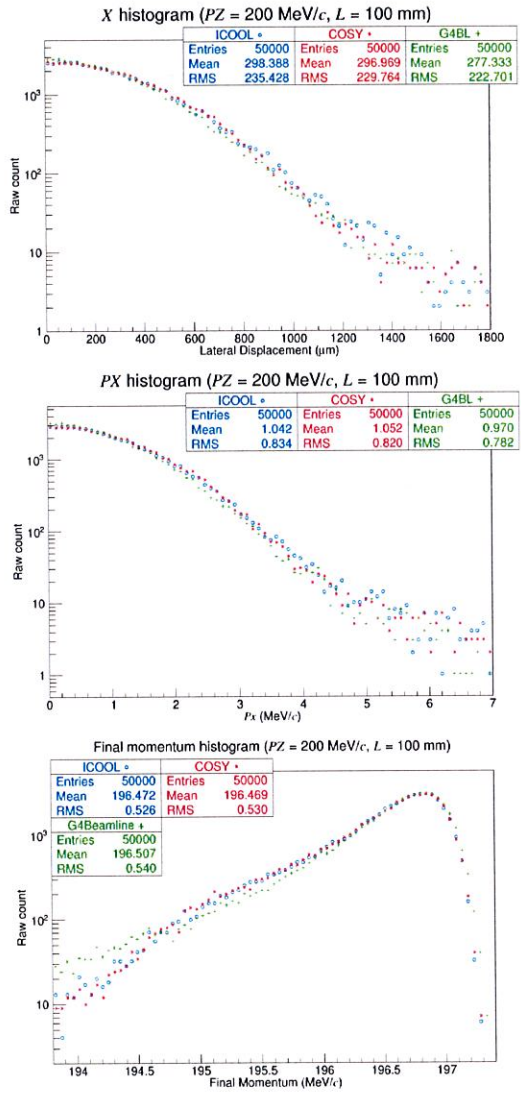


Figure 5.6: Muons of momentum 200 MeV/ c through 100 mm liquid hydrogen.

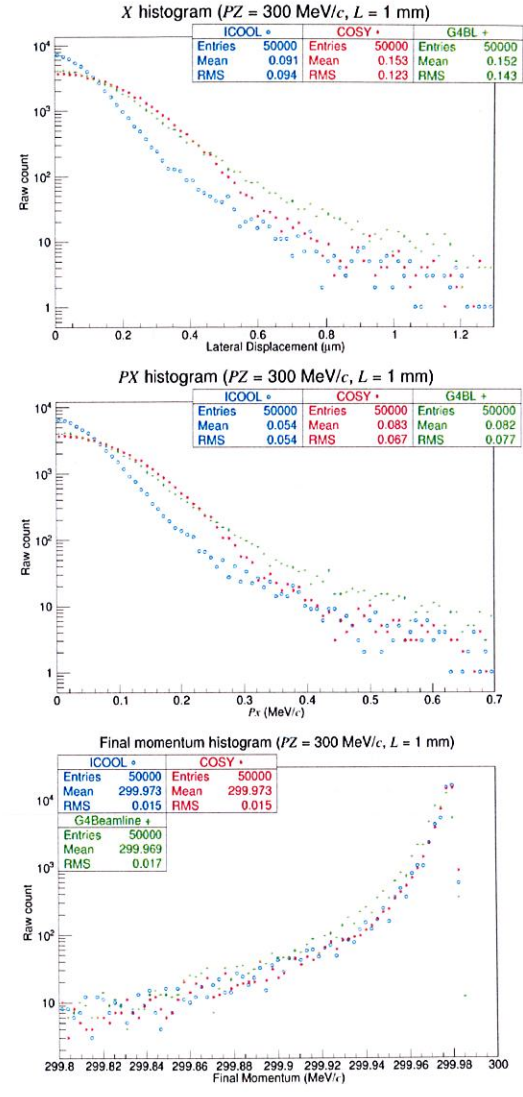


Figure 5.7: Muons of momentum 100 MeV/ c through 1 mm liquid hydrogen. Observe that for the x and p_x histograms, COSY and G4Beamline follow a Gaussian-like peak whereas ICOOL follows a Fano peak.

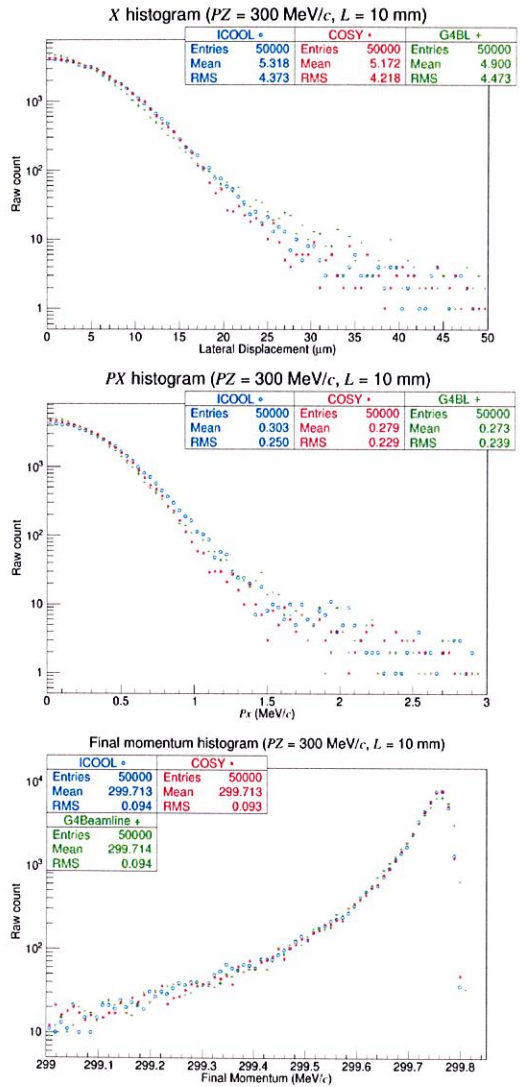


Figure 5.8: Muons of momentum $300 \text{ MeV}/c$ through 10 mm liquid hydrogen.

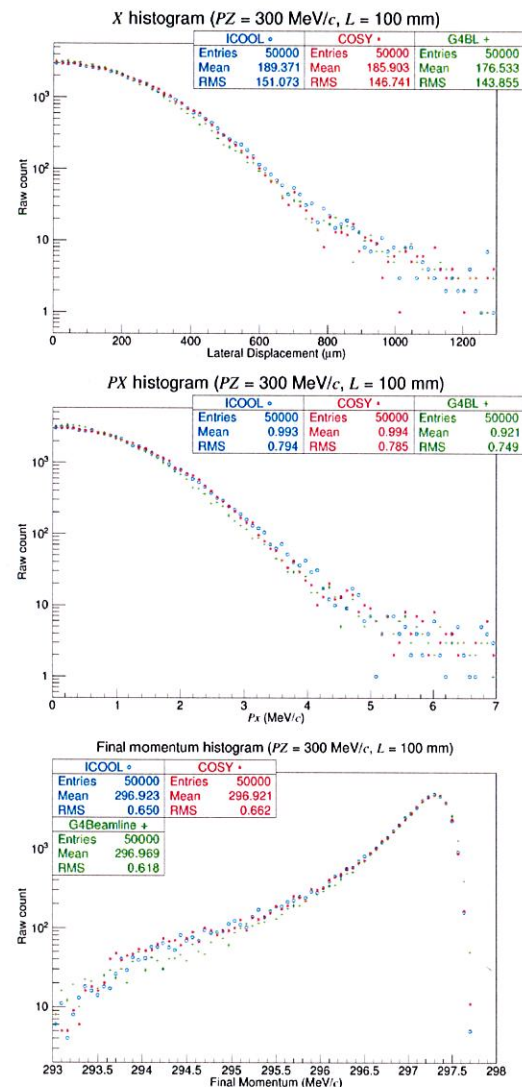


Figure 5.9: Muons of momentum $300 \text{ MeV}/c$ through 100 mm liquid hydrogen.

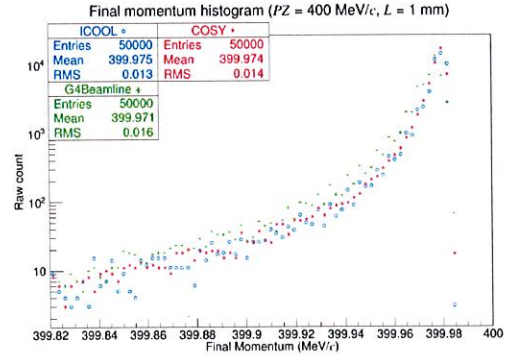
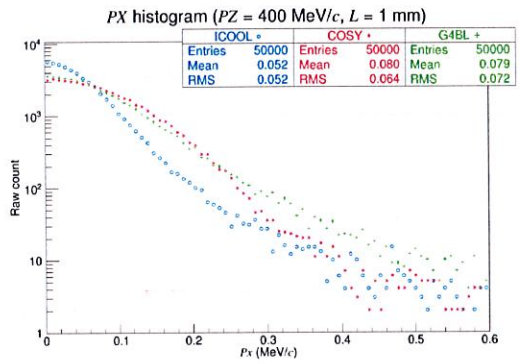
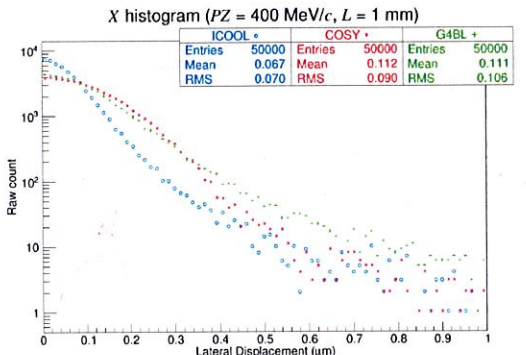


Figure 5.10: Muons of momentum $100 \text{ MeV}/c$ through 1 mm liquid hydrogen. Observe that for the x and p_x histograms, COSY and G4Beamline follow a Gaussian-like peak whereas ICOOL follows a Fano peak.

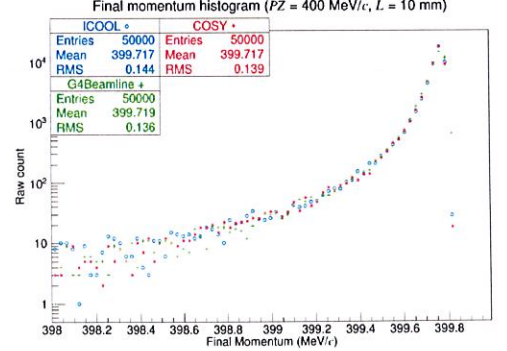
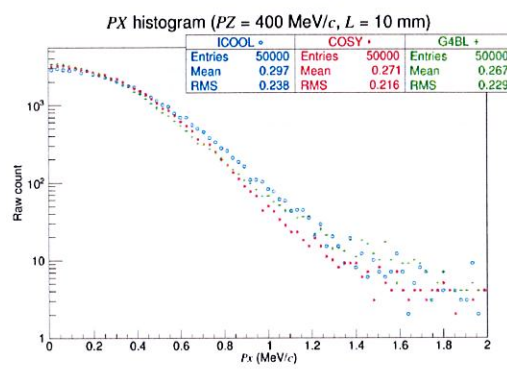
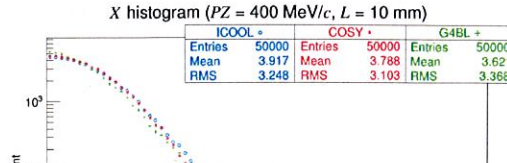


Figure 5.11: Muons of momentum $400 \text{ MeV}/c$ through 10 mm liquid hydrogen.

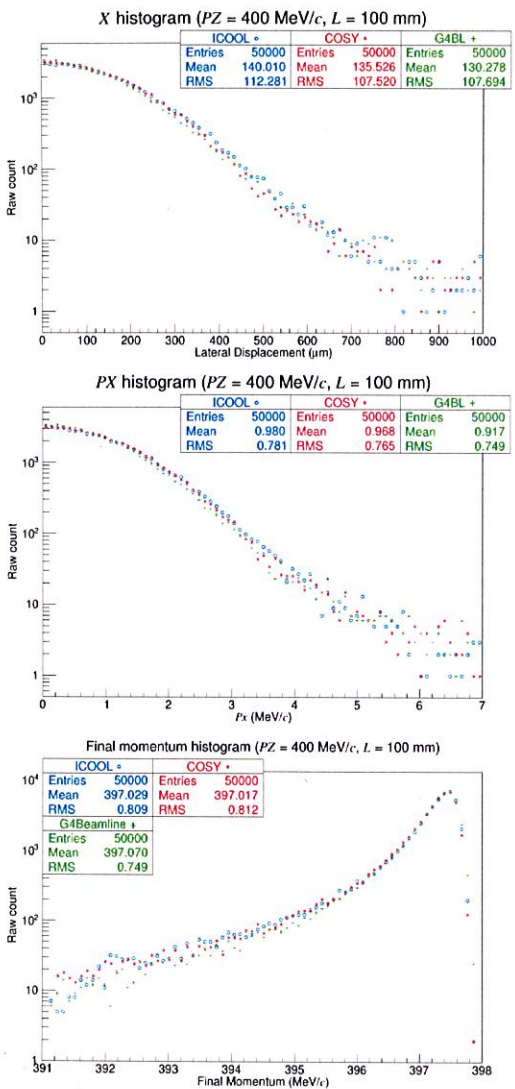


Figure 5.12: Muons of momentum $400 \text{ MeV}/c$ through 100 mm liquid hydrogen.

For the 1 mm figures (Figures 5.1, 5.4, 5.7, and 5.10) there is much disagreement between the codes' transverse momentum distributions. Since the transverse momentum and transverse position coordinates are related, there is also disagreement among the transverse position distributions. This is likely because the default ICOOL scattering model uses a Fano peak with a Rutherford tail whereas both COSY and G4Beamline use a Gaussian peak. It can be seen by, e.g., Figure 5.1 that COSY, like G4Beamline, uses the Gaussian model for the peak but, like ICOOL, then switches to a Rutherford tail.

For the 10 mm figures (Figures 5.2, 5.5, 5.8, and 5.11), both x and p_x distributions agree well. For COSY, the tail of the distribution falls off slightly faster after approximately $1 \text{ MeV}/c$.

For the final momentum plots, ICOOL and COSY agree quite well. This is not surprising since both codes use Landau theory to describe the energy loss distribution. G4Beamline occasionally disagrees. An example of this can be seen in Figure 5.4. However, given the scale of the horizontal axis this disagreement is much smaller than it initially appears.

5.2 Validation

The new COSY routines were also compared to the Muon Scattering Experiment [32], often referred to as MuScat. This experiment measured the scattering of a beam of collimated muons through seven materials. To emulate this, pencil beams with momentum $P = 172 \text{ MeV}/c$ were created in COSY, G4Beamline, and ICOOL. The pencil beam consisted of 5×10^6 particles and was propagated through 109 mm of liquid hydrogen, 159 mm of liquid hydrogen, and 3.73 mm of beryllium. Liquid hydrogen was chosen to represent muons through long absorbers of low- Z materials. Beryllium, on the other hand, was chosen to represent muons through much thinner

among

overinterpreting statistical fluctuations

and denser media. COSY took a single step through the absorbers while G4BL took a step size of 1 mm. The data points were normalized to the total probability, was calculated via Simpson's rule. The probability per radian was then found by dividing the probability of the data point by the scattered angle at that point. The results are shown below.

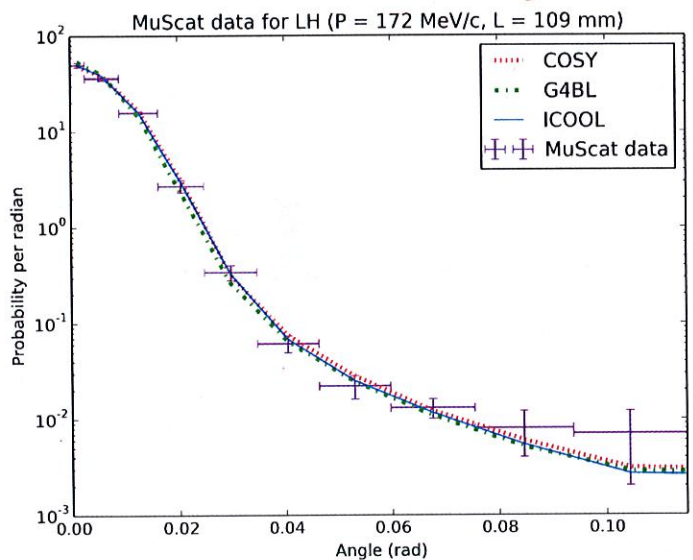


Figure 5.13: MuScat angular scattering results for 109 mm of liquid hydrogen compared against COSY (red), G4BL (green), and ICOOL (blue).

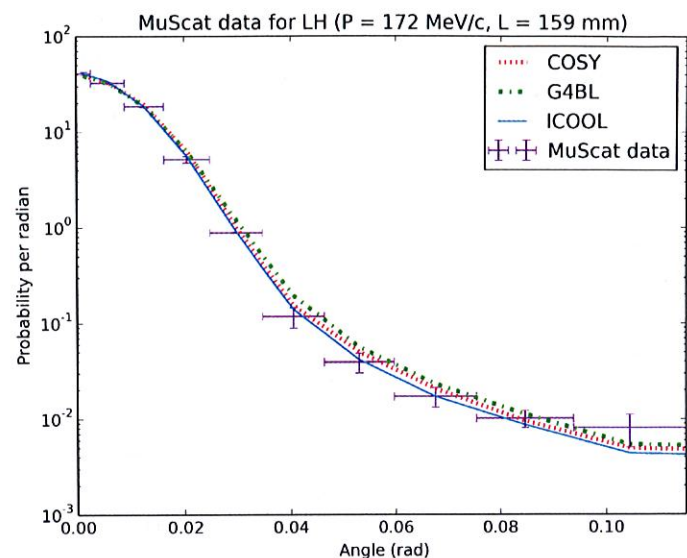


Figure 5.14: MuScat angular scattering results for 159 mm of liquid hydrogen compared against COSY (red), G4BL (green), and ICOOL (blue).

? what
was

don't make sense

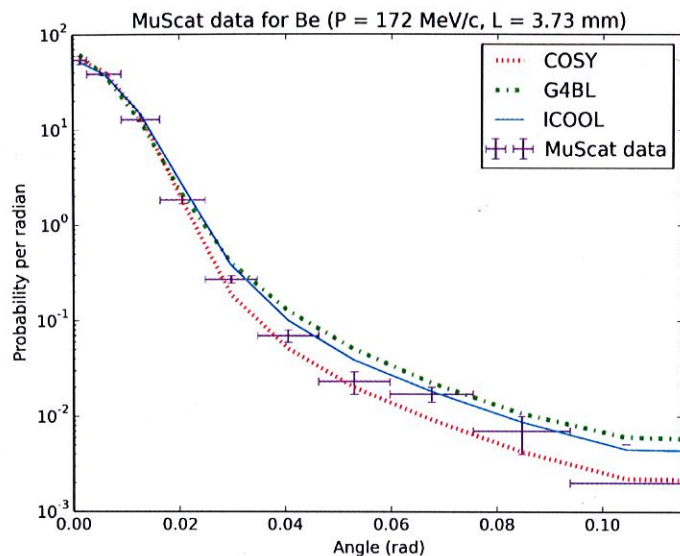


Figure 5.15: MuScat angular scattering results for 3.73 mm of beryllium compared against COSY (red), G4BL (green), and ICOOL (blue).

In the liquid hydrogen cases, COSY appears to match both G4Beamline and ICOOL very well, as well as the MuScat data points. ICOOL appears to have a sharper peak than either COSY or G4Beamline, which can be more easily seen in the 159 mm liquid hydrogen case than in the 109 mm case. In the case of beryllium, COSY matches the MuScat points slightly better than G4Beamline and ICOOL, particularly for the two data points between 0.04 and 0.06 radians.

5.3 The Muon Ionization Cooling Experiment

This section introduces the Muon Ionization Cooling Experiment (MICE [34]), a practical application for the new absorber routines in COSY. The results of MICE

simulations in ICOOL, G4Beamline, and COSY are examined, showing good agreement.

in progress

5.3.1 **Introduction to MICE.** The Muon Ionization Cooling Experiment (MICE [34]) is an experiment currently being developed at the Rutherford Appleton Laboratory in Oxfordshire, U.K. Its goal is to show a proof-of-principle demonstration of muon ionization cooling. MICE Step IV configuration is explored in this work. The Step IV cell includes 12 magnetic coils positioned symmetrically around a flat absorber. Figure 5.16 shows a schematic of this lattice with 350 mm of liquid hydrogen as the absorber.

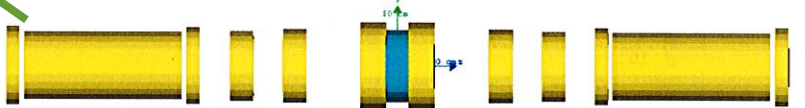


Figure 5.16: MICE Step IV cell. Magnetic coils are shown in yellow and the absorber is shown in blue. The green and blue axes are the y and z axes, here drawn to scale as 500 mm each. The aperture (invisible for display purposes) is 300 mm. Image rendered via G4Beamline [18].

*why neglect window shape
cite published papers, please*

5.3.2 **Results of MICE Simulation.** 10^6 muons were simulated through the cell in Figure 5.16. The coil parameters may be found in Table 5.1. The absorber was a 350 mm cylindrical block of liquid hydrogen centered at $z = 0$. The aperture was set to 300 mm. Note that other materials such as safety windows were not accounted for in this simulation. The decay process was disabled in all simulation codes. The beam started at -2.45105 m and ended at 2.450 m. The initial distribution was Gaussian with parameters summarized in Table 5.2.

While the selection of order and step size is detailed in the next section, it was found that a 5th order simulation was sufficient for COSY. Through the coil-

MICE Step IV Coil Parameters

Name	z position mm	Length mm	Inner radius mm	Outer radius mm	Current density A/mm ²
End2	±3200.28	110.642	258	325.783	±126
Center	±2450.275	1314.3	258	280.125	±148
End1	±1700.29	110.642	258	318.905	±133
Match2	±1300.29	199.492	258	288.925	±132
Match1	±860.645	201.268	258	304.165	±133
Focus	±202.2	213.3	267.6	361.9	±104

Table 5.1: MICE Step IV coil parameters corresponding to Figure 5.16.

~~flip a solenoid mode?
presumably ↗ but should specify explicitly
seem oversimplified
@ 25th order many conditions missing?~~

MICE Step IV Initial Distribution Parameters

Parameter	Mean	Standard deviation
x (mm)	0	32
y (mm)	0	32
z (mm)	0	0
p_x (MeV/c)	0	20
p_y (MeV/c)	0	20
p_z (MeV/c)	200	30

Table 5.2: MICE Step IV initial distribution Gaussian parameters.

only portion of the simulation, 50 steps were taken on each side of the absorber (or roughly a step size of 46 mm both upstream and downstream). The particles were tracked through the momentary transfer map after each step and then the transfer map was set to unity. It was noted that for the coil-only section, a single transfer map was not sufficient even at the 9th order. This is due to the relatively large phase space volume of the beam and the complexity of the magnetic field. Through the absorber-coil region (-350/2 mm to 350/2 mm), it was found that a 1st order map with 5 steps was sufficient. This is due to the transverse phase space of the beam reaching a minimum and the magnetic field passing through the point of symmetry. Compounding the map without propagating the beam also gave poor results.

When one takes the composition of two n^{th} order transfer maps, a transfer map of order $n \times n$ is the result. For example, the first step in MICE simulation would yield a 5th order transfer map. Taking the second step would give a new transfer map of order $5 \times 5 = 25$. However, since COSY is operating in the 5th order mode, the new transfer map would not be 25th order, but rather it would be truncated to a 5th order map. For this reason, the particles were propagated through the momentary transfer map after each step in the simulation.

The magnetic field in G4Beamline was created using the **coil** and **solenoid** commands. The field was then exported to a file using the **printfield** command to a file. The field map file was read by both G4Beamline (which used the **fieldmap** command) and ICOOL (which used the **GRID** command operating in G43D mode).

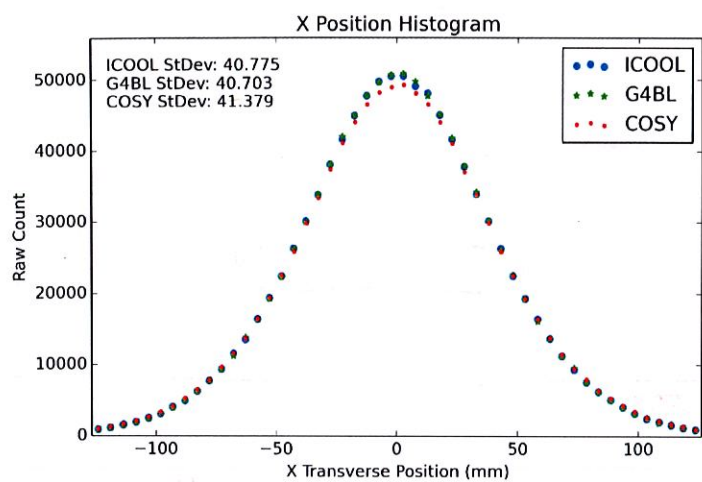


Figure 5.17: MICE Step IV x position results for 350 mm of liquid hydrogen.

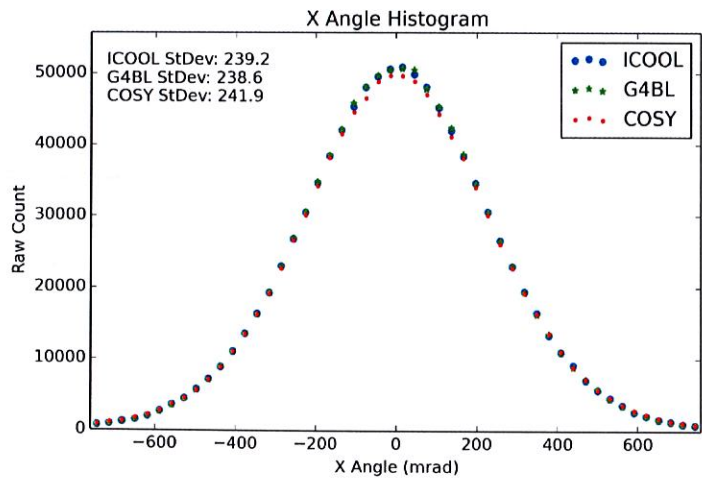


Figure 5.18: MICE Step IV x angle results for 350 mm of liquid hydrogen.

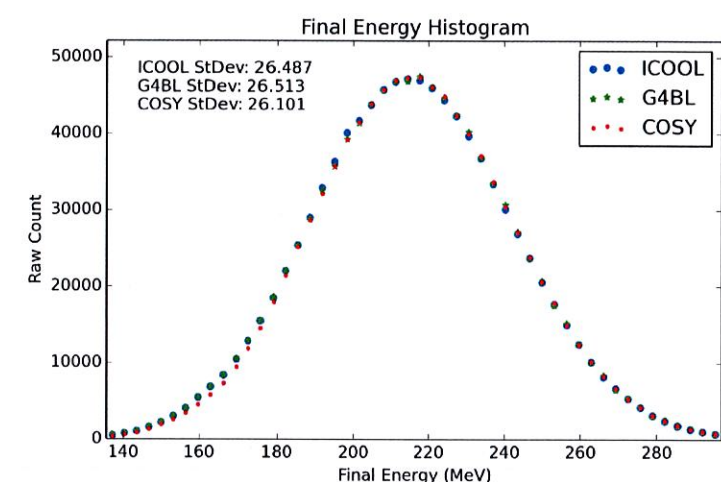


Figure 5.19: MICE Step IV final energy results for 350 mm of liquid hydrogen.

The runtimes of ICOOL, G4Beamline, and COSY are listed in Table 5.3. To reiterate, COSY was run at 5th order with 50 steps before the absorber, 5 steps at 1st order inside the absorber, and 50 steps at 5th order after the absorber. Note that the initialization time for G4Beamline to create the field maps was 33 seconds. The time it took to create a text file for ICOOL input was 11 seconds. Since G4Beamline only has to create the field map once, the initialization time is added to neither ICOOL nor G4Beamline the run times in Table 5.3. COSY did not have any initialization time.

As a second test, MICE configuration in Figure 5.16 was simulated using 65 mm of lithium hydride. Lithium hydride is an attractive material because, unlike liquid hydrogen, it does not require cryogenic conditions, but still maintains a low Z value. It can be seen from Figures 5.20, 5.21, and 5.22 that 65 mm of lithium hydride has a similar effect on the beam as 350 mm of liquid hydrogen.

Figures cited?
not done?

Run Times (in seconds) for MICE Step IV Simulation

Number of particles:	10^6	10^5	10^4	10^3
COSY:	367	31	6	4
G4BL (coils):	3973	392	40	6
G4BL (field map):	662	75	15	9
ICOOL (field map):	1091	117	19	9

Table 5.3: Run times for MICE Step IV simulation for liquid hydrogen. Note that the G4Beamline initialization time was not added to the run time values. G4BL (coils) represents the simulation in G4Beamline when the `coil` parameter was used. G4BL (field map) represents the simulation when G4Beamline (like ICOOL) read the field map from a file.

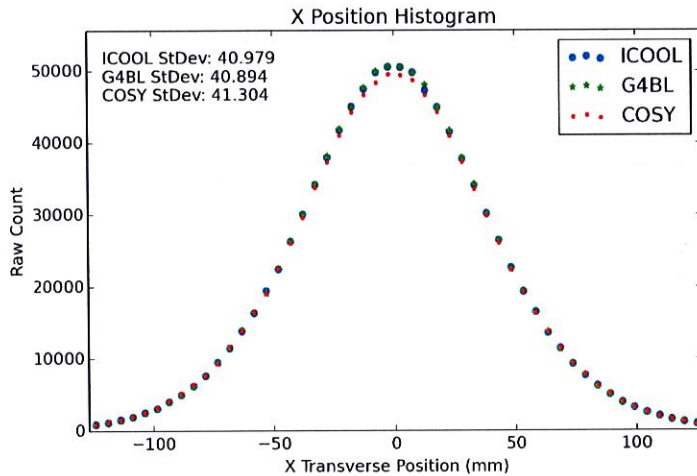


Figure 5.20: MICE Step IV x position results for 65 mm of lithium hydride.

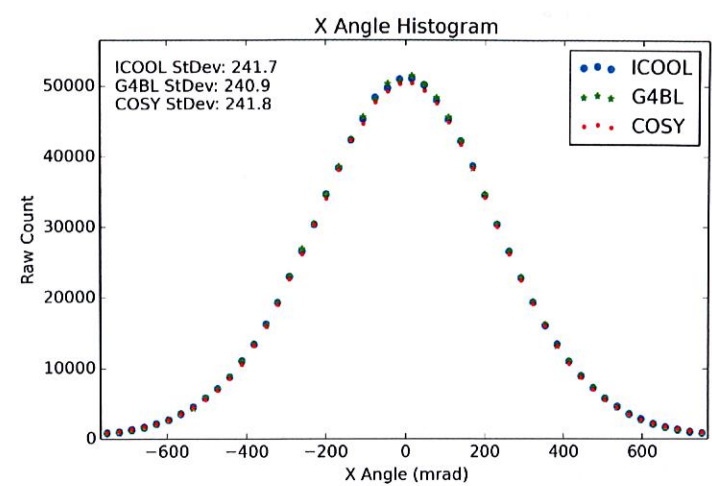


Figure 5.21: MICE Step IV x angle results for 65 mm of lithium hydride.

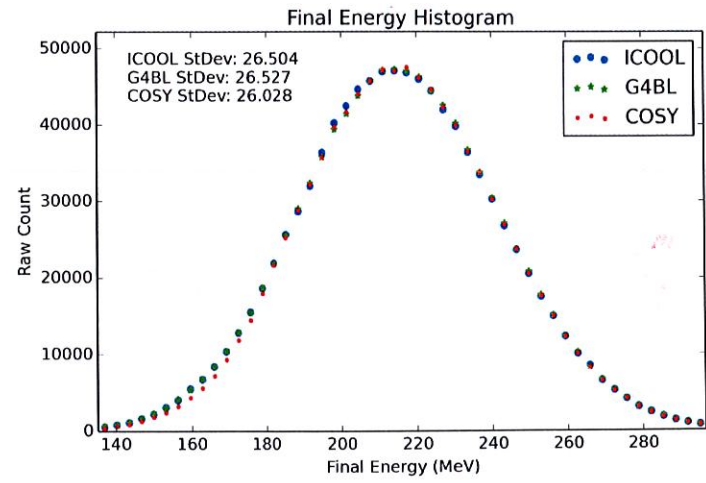


Figure 5.22: MICE Step IV final energy results for 65 mm of lithium hydride.

Step Size Dependence for Absorber-Coil Section (Liquid Hydrogen)

	ICOOL (field map)	G4BL (field map)	COSY		
			1 step	5 steps	10 steps
σ_x (mm):	50.5	50.4	50.3	50.6	50.7
σ_{θ_x} (mrad):	201.9	201.4	205.7	200.5	199.9
σ_E (MeV):	26.7	26.7	26.6	26.6	26.6
Computational time (s):	19	25	4	5	8

Table 5.4: First order step size dependence for the absorber-coil section of MICE Step IV lattice for 10^5 muons passing through 350 mm of liquid hydrogen. The transmission was very nearly 100% for all three codes regardless of circumstances. The energy for COSY does not change much with respect to order since the energy loss algorithm does not use a transfer map approach.

5.3.3 Step Size Effects. Several step sizes were tested in COSY to ensure optimal efficiency. The results are discussed here.

For the absorber-coil section of MICE liquid hydrogen lattice ($-0.35/2$ to $0.35/2$), it was found that 5 steps were sufficient to approximate the superposition of the absorber and coils. To study this step size dependence, 10^5 particles from the initial distribution found in Table 5.2 were propagated through the 350 mm liquid hydrogen flat absorber. This simulation took the surrounding magnetic fields into account. Table 5.4 shows the effect of changing the step size for the absorber-coil section only.



The discrepancy of COSY w.r.t. G4Beamline is <1% for all components. Results of the absorber-coil simulation can be seen in Figures 5.23-5.25. There is good agreement between ICOOL, G4Beamline, and COSY.

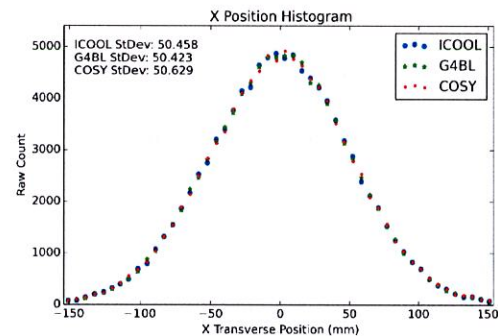


Figure 5.23: Absorber-coil simulation results for x with 10^5 muons and a 5 step propagation.

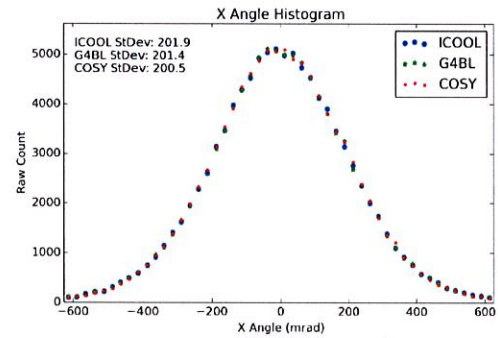


Figure 5.24: Absorber-coil simulation results for θ_x with 10^5 muons and a 5 step propagation.

(why switch
between?
mm?)

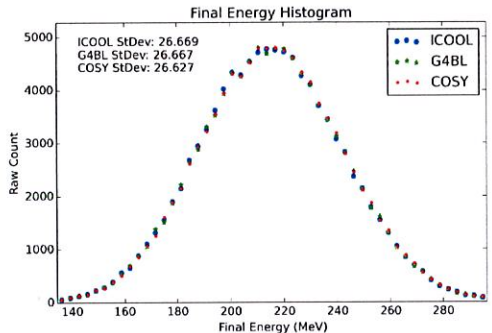


Figure 5.25: Absorber-coil simulation results for the final energy with 10^5 muons and a 5 step propagation.

For both the upstream and downstream sections, the entire MICE cell was simulated (-2.45105 m to 2.450 m). It was found that COSY operated sufficiently well at order 5 and with 50 steps in the simulation.

To study this step size dependence, 10^5 particles from the initial distribution found in Table 5.2 were propagated through MICE cell. Table 5.5 shows the effect of changing the step size.

For most COSY cases, the discrepancy w.r.t. G4Beamline is on the order of 1%. 5th order at 50 steps was selected as “best” because of the increased agreement with both ICOOL and G4Beamline when compared to both 3@50 and 5@30 (particularly for the transmission). Moreover, 5@50 gives similar results as 7@100 but with drastically decreased computational time.

Results of the step size study for 5@50 can be seen in Figures 5.26 and 5.27. There is good agreement between ICOOL, G4Beamline, and COSY.

Step Size Dependence for MICE Step IV

	ICOOL (field map)	G4BL (field map)	COSY [order]@[number of steps]	3@50	5@30	5@50	5@100	7@100
σ_x (mm):	40.7	40.7	42.5	41.2	41.4	41.4	41.0	41.0
σ_{θ_x} (mrad):	240.2	240.2	248.3	239.8	242.1	243.8	241.8	
% transmission:	98.5	98.5	99.6	96.8	97.7	98.6	97.9	
Comp. time (s):	114	82	12	21	25	43	132	

Table 5.5: Step size dependence for MICE Step IV lattice for 10^5 muons. The notation for COSY is [order]@[number of steps].

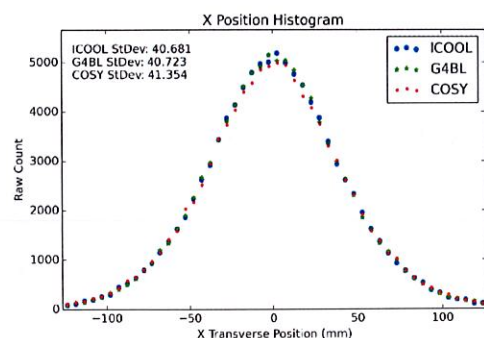


Figure 5.26: MICE simulation results for x with 10^5 muons at 5th order and 50 steps.

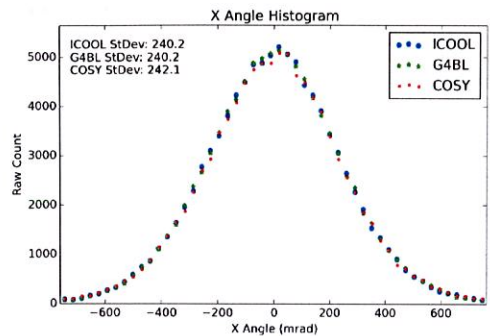


Figure 5.27: MICE simulation results for θ_x with 10^5 muons at 5th order and 50 steps.

5.4 Summary

In summary, new simulation tools for muon ionization cooling have been added to COSY Infinity for particle-by-particle propagation. The energy straggling, multiple scattering, transverse position, and time-of-flight models were developed from first principles. The algorithms implemented have been modified via empirical fit to MuScat [32] while keeping reasonable agreement with G4Beamline. Fitted with this new software, COSY has simulated one of the current muon ionization cooling efforts, MICE Step IV [34], yielding agreement within 1% of both ICOOL and G4Beamline. The code developed in this work is accurate, fast, and user-friendly.

APPENDIX A DERIVATION OF TRANSVERSE EMITTANCE

```

IMPLICIT DOUBLE PRECISION(A-H,O-Z)

DOUBLE PRECISION MASS

DOUBLE PRECISION, DIMENSION(:, :, ), ALLOCATABLE :: V ! V(NPART,6)

INTEGER IALLOCATESTATUS,I,J

!-----MEMORY MANAGEMENT -----
PARAMETER(LMEM=1000000000,LVAR=100000000,LDIM=10000)
INTEGER NTYP(LVAR),NBEG(LVAR),NEND(LVAR),NMAX(LVAR),
* NC(LMEM),NDIM(LDIM)

DOUBLE PRECISION CC(LMEM)

COMMON NTYP,NBEG,NEND,NMAX, CC,NC, NDIM, IDIM, IVAR,IMEM
COMMON /TYID/ NRE,NST,NLO,NCM,NVE,NIN,NIV,NDA,NCD,NTM,NGR

! CONSISTENCY CHECKS AND PREPARATION
! *****
IF(NTYP(IZ).NE.NRE) CALL FOXNTY(IAV)
IF(NTYP(IREG).NE.NRE) CALL FOXNTY(ISI)
IF(NTYP(INPART).NE.NRE) CALL FOXNTY(IN)
IF(NTYP(IUI).NE.NRE) CALL FOXNTY(IUI)
IF(NTYP(IAPE).NE.NRE) CALL FOXNTY(IAPE)

! GET VARS
! *****
Z = CC(NBEG(IZ))
REG = NINT(CC(NBEG(ISI)))
NPART = NINT(CC(NBEG(INPART)))
UI = NINT(CC(NBEG(IUI)))
APE = CC(NBEG(IAPE))

MASS = 105.6583715

ALLOCATE(V(NPART+10,7),Stat=IALLOCATESTATUS)
IF (IALLOCATESTATUS /= 0) STOP "*** Not enough memory ***"

DO 7 I=1,NPART
    X =CC(NBEG(IV+1)+I-1)
    PX=CC(NBEG(IV+2)+I-1)
    Y =CC(NBEG(IV+3)+I-1)
    PY=CC(NBEG(IV+4)+I-1)
    T =CC(NBEG(IV+5)+I-1)
    E =CC(NBEG(IV+6)+I-1)
    P =SQRT(E**2-MASS**2)
    PZ=SQRT(P**2-PX**2-PY**2)

    ! MAKE SURE PARTICLE ISN'T LOST
    TOL=1E10
    IF (APE.LE.0) APE=TOL
    IF ((X.GE.TOL).OR.(Y.GE.TOL).OR.(T.GE.TOL).OR.(PZ.GE.TOL).OR.
& (SQRT(X**2+Y**2).GE.APE).OR.(X.NE.X).OR.(PX.NE.PX).OR.
& (Y.NE.Y).OR.(PY.NE.PY).OR.(T.NE.T).OR.(E.NE.E)) THEN
        WRITE(6,*) "PARTICLE ",I," LOST!"
    ELSE
        WRITE(6,20) I,1,2,0,1,T,X,Y,Z,PX,PY,PZ,0,0,0,1,0,0,0,0,0,0,0,0
    ENDIF
CONTINUE
FORMAT(I,4I2,7E22.14,11I2)
END

```

BIBLIOGRAPHY

- ~~Not to give complete info so reader can't find reference~~
- Publisher?
- ~~available where?~~
- ~~Be more specific!~~
- ~~ICOLL? relevant?~~
- ~~page n volume missing~~
- [1] D. Griffiths. *Introduction to Elementary Particles*. 2nd edition, 2008.
 - [2] Pauline Gagnon. The standard model: A beautiful but flawed theory. <http://www.quantumdiaries.org>, 2014.
 - [3] D. Griffiths. *Introduction to Electrodynamics*. 3rd edition, 1999. Publisher?
 - [4] M. Berz and K. Makino. *CERN Y Infinity Beam Physics Manual*, 2013. Version 9.1.
 - [5] M. Berz. *Modern Map of Tools in Particle Beam Physics*. 1999. Available where?
 - [6] M. Berz. *Introductory Beam Physics*.
 - [7] J. Nielsen and D. McMorrow. *Elements of Modern X-ray Physics*. 2nd edition, 2011.
 - [8] D. Griffiths. *Introduction to Quantum Mechanics*. 2nd edition, 2005.
 - [9] J. V. José and E. J. Saletan. *Classical Dynamics: A Contemporary Approach*. 1998.
 - [10] Fermi National Accelerator Laboratory. Muon Accelerator Program.
 - [11] G. K. O'Neill. Storage-ring synchrotron: Device for high-energy physics research. *Phys. Rev.*, 102, 1956.
 - [12] D.B. Lichtenberg, P. Stehle, and K. R. Symon. Modifications of Liouville's theorem required by the presence of dissipative forces. *MURA*, 126, 1956.
 - [13] Yu.M. Ado and V.I. Balbekov. Use of ionization friction in the storage of heavy particles. *Sov. Atomic Energy*, 31, 1971.
 - [14] R. P. Johnson. Ionization cooling. *Proceedings of COOL 2007*, 2007.
 - [15] J. Beringer *et al.* (PDG) PR D⁸⁵, 010001 chpt. 31, 2013.
 - [16] Particle Data Group Atomic Nuclear Properties. <http://pdg.lbl.gov/2014/AtomicNuclearProperties/>, 2014.
 - [17] R.C. Fernow. ICOLL. <http://www.cap.bnl.gov/ICOLL/fernnow/readme.html>, 2012. version 3.30.
 - [18] Tom Roberts. G4beamline. <http://www.muonsinternal.com/muons3/G4beamline>. Version 2.15w.
 - [19] CERN. *GEANT4 Physics Reference Manual*, 2011. Version 9.5.0.
 - [20] H. A. Bethe. Scattering of electrons. *Z. für Physik*, 76, 1932.
 - [21] L. Landau. On the energy loss of fast particles by ionisation. *J. Phys. U.S.S.R.*, 8, 1944.
 - [22] Robert L. Borrelli and Courtney S. Coleman. *Differential Equations: A Modeling Perspective*. 2nd edition, 2004.

- ~~Not to give complete info so reader can't find reference~~
- Publisher?
- ~~available where?~~
- ~~Be more specific!~~
- ~~ICOLL? relevant?~~
- ~~page n volume missing~~
- ~~These are much better references!~~
- [23] M. S. Livingston and H. A. Bethe. Chapter XVI: Auxiliary data for the evaluation of experiments. *Reviews of Modern Physics*, 9, 1937. Section C: Nuclear Dynamics, Experimental.
 - [24] P. V. Vavilov. Ionization losses of high energy heavy particles. *Soviet Physics JETP*, 5, 1957.
 - [25] N.W. Ashcroft and N.D. Mermin. *Solid State Physics*, HRW International Editions. 1976.
 - [26] H. Bichsel. Straggling in thin silicon detectors. *Rev. Mod. Phys.*, 60, 1988.
 - [27] H.W. Lewis. Multiple scattering in an infinite medium. *Phys. Rev.*, 78, 1950.
 - [28] S. Goudsmit and J.L. Saunderson. Multiple scattering of electrons. *Phys. Rev.*, 57, 1939.
 - [29] V. Highland. Some practical remarks on multiple scattering. *NIM*, 129, 1975.
 - [30] G. R. Lynch and O. I. Dahl. Approximations to multiple Coulomb scattering. *NIM*, 1991.
 - [31] CERN. *GEANT - Detector Description and Simulation Tool*, 1993. Version 3.21.
 - [32] D. Atwood *et al.* The scattering of muons in low z materials. *NIM*, 251, 2006.
 - [33] R. Fernow and J. C. Gallardo. Muon transverse ionization cooling: Stochastic approach. *Phys. Rev. E*, 52, 1995.
 - [34] U. Bravar *et al.* Mice: The muon ionization cooling experiment. In *Proceedings of the DPF-2011 Conference*, 2011. ~~These are much better references!~~
 - [35] Chuong B. Do. The multivariate gaussian distribution. <http://cs229.stanford.edu/section/gaussians.pdf>, 2008. Stanford University CS 229 Lecture Notes.
 - [36] P. C. Mahalanobis. On the generalized distance in statistics. *Proceedings of the National Institute of Sciences of India*, 2, 1936.